UNIVERSITA' DI PISA

Corso di Laurea Magistrale in Fisica

Anno Accademico 2014/2015

Tesi di Laurea Magistrale

A multiwavelength study of the extended radio lobes of the giant elliptical radio galaxy M87

Candidato
Federica Savini

Relatore
Prof. Steven Neil Shore

Agli spiriti liberi

Contents

Physical constants and acronyms

Milliarcsecond	1 mas	$4.8 \cdot 10^{-9}$ rad
Astronomical unit	1 AU	$1.5 \cdot 10^{13}$ cm
Light year	1 ly	$9.5 \cdot 10^{17}$ cm
Parsec	1 pc	$3 \cdot 10^{18}$ cm
		3.26 ly
Solar mass	1 $M_\odot$	$2 \cdot 10^{33}$ g
Solar luminosity	1 $L_\odot$	$4 \cdot 10^{33}$ erg s^{-1}
Jansky	1 Jy	10^{-23} erg s^{-1} cm^{-2} Hz^{-1}
Electron volt	1 eV	$1.6 \cdot 10^{-12}$ erg
Speed of light	c	$3 \cdot 10^{10}$ cm s^{-1}
Boltzmann constant	σ	$5.67 \cdot 10^{-5}$ erg cm^{-2} s^{-1} K^{-4}
Stefan-Boltzmann constant	k	$1.38 \cdot 10^{-16}$ erg K^{-1}
Thomson cross section	σ_T	$6.65 \cdot 10^{-25}$ cm^2
Gravitational constant	G	$6.67 \cdot 10^{-8}$ cm^3 s^{-2} g^{-1}
Electron mass	m	$9.1 \cdot 10^{-28}$ g
Proton mass	m_p	$1.67 \cdot 10^{-24}$ g
Elementary charge	e	$4.8 \cdot 10^{-10}$ e.s.u

Table 1. Here, there is a list of the some astronomical and physical constants.

EGRET	Energetic Gamma-Ray Experiment Telescope (CGRO)
HESS	High Energy Stereoscopic System
HST	Hubble Space Telescope
LOFAR	low-frequency Array (radio)
NED	NASA/IPAC Extragalactic Database
NRAO	National Radio Astronomy Observatory (USA-VA)
SDSS	Sloan Digitized Sky Survey
VLA	Very Large Array (radio)
VLBA	Very Long Baseline Array (radio)
VLBI	Very Long Baseline Interferometry (radio)
VSOP	VLBI Space Observatory Programme

Table 2. Here, there is a list of the most common abbreviations and acronyms of projects and catalogues used in this thesis and in astrophysics in general.

AGN	Active galactic nucleus/nuclei
BAL	Broad absorption line quasar
BLR	Broad line region
BLRG	Broad line radio galaxy
CMRB	Cosmic Microwave Background radiation
FR	Fanaroff and Riley radio galaxy (Fanaroff & Riley, 1974)
ICM	Intracluster medium
LINER	Low-ionization nuclear emission-line region
MHD	Magnetohydrodynamics
NLR	Narrow line region
OVV	Optical violent variable blazar
PSF	Point spread function
SMBH	Supermassive black hole
VHE	Very high energy

Table 3. Here, there is a list of the most common abbreviations and acronysms of some physical phenomena used in this thesis and in astrophysics in general. However, they could present variations throughout the literature.

Introduction

Among the galaxies, those with strong nuclear activity are the most energetic persistent objects in the Universe. Active galactic nuclei (AGN) are characterized by high luminosities coming from a tiny volume, creating an energy source that cannot be attributed to stars or gas. Instead, the energy is thought to come from accretion onto a supermassive black hole in the nucleus by material raining in from the host galaxy. This explains their small size and high power output, but there is more to understand.
AGN are sites of high energy processes. The same mechanisms that accelerate cosmic rays and the energetic particles in solar flares and supernova remnants are likely to be operating at the center of these galaxies to accelerate relativistic charged particles. However, they are fairly complex objects own to the extraordinary variety of diverse physical domains as general relativity, accreting disks, jets, plasma physics and synchrotron emission.
Some of them are able to generate powerful jets creating a direct physical link between the nucleus and the host galaxy or even the cluster. The first jet observed in an AGN was the M87 bright jet (Curtis, 1918). M87, which is the subject of this thesis, is a large elliptical galaxy harboring an active nucleus and was one of the first identified radio sources. It is one of the nearest radio galaxies and of the brightest radio source in the northern sky. Furthermore, M87 was the first for which the cluster was identified with this as a central galaxy: it lives at the center of Virgo cluster that is the nearest cluster of galaxies, providing the possibility to study the interaction of its jet and the intracluster medium (ICM) that forms a radio halo with a projected end-to-end length of about 80 kpc, called Virgo A.
Radio halos are the clearest evidence of the presence of magnetic fields and cosmic ray mixed with the thermal ICM in the central regions of clusters of galaxies. Relativistic electrons injected in the ICM by the AGN lose energy mainly by synchrotron emission.
This thesis presents a study of the extended radio emitting structures of M87, which is observable at low radio frequency through interferometric data from 25 MHz (LOFAR; de Gasperin et al., 2012), 74 MHz (VLA; Kassim et al., 1993), 140 MHz (LOFAR; de Gasperin et al., 2012), 327 MHz (VLA; Owen et al., 2000) to 10.6 GHz (Effelsberg; Rottmann et al., 1996).
The analysis is performed using new low-frequency radio maps at 74 MHz and 330 MHz. These data were obtained by Dr. N. Kassim and Dr. T. Clarke (Naval Research Laboratory Washington) with the low-frequency upgrade of the Very Large Array (VLA) radio telescope. The VLA, sited near Socorro (New Mexico, USA), is an element aperture synthesis interferometer composed of 27 radio antennas.

As an introduction, I present an overview of the AGN phenomenon and classification, principally from an observational point of view. Then, I discuss radio galaxies as AGN with strong radio emission. Finally, I describe M87 and its observations across the electromagnetic spec-

trum, mainly in the radio band.
The Data analysis chapter, after a digression about the non-thermal processes relevant to AGN, presents the result of this work: a low-frequency spectral index map with characterization of its relative errors. This map provides information about the aging and acceleration mechanisms for trapped synchrotron-emitting electrons and on their energy distribution.
The Conclusion chapter provides a physical explanation for the many fine structure features that appear in the maps, especially one enigmatic feature that emerged from this study. This is a localized flattening of the power law spectrum that has no counterparts in the literature.
The appendices collect information about the radio interferometry technique and CASA, which is the software used to analyze radio astronomical data.

Chapter 1

Active Galactic Nuclei

Galaxies are gravitationally bound systems of stars, gas and dust. Although the majority of their centers is bright due to increased star density, a small fraction $(1 - 10\%)$ of galaxies are distinguished by their brilliant point-like nuclei which often outshine their host galaxies. These nuclei are characterized by so high luminosities from a compact region that are called active.
An active galactic nucleus has an energy source beyond what can be attributed to stars or gas heated by them: a non-stellar or non-thermal emission. They emit strongly over the whole electromagnetic spectrum, even gamma-rays where most galaxies hardly radiate at all.
Common properties include the variability, the presence of strong broad emission lines and a broad-band non-thermal continuum. Many active nuclei are variable, changing their luminosity and their emission lines strength substantially within a few months, days, or even hours at X-ray wavelengths. To allow such fast variability knowing that no signal can travel faster than light, both broad lines and continuum radiation must come from a region no more than a few light-weeks across.

1.1 Observational features

Phenomena hardly ever observed in normal galaxies occur to be signatures of the presence of activity. The most important observable features used as tracers of these sources can be summarized here [1], bearing in mind that not every AGN shows every property:

- small angular size
  in optical and X-ray images the nucleus appears to be a bright point source, and a high dynamic range is needed to observe both the nucleus and the host galaxy. The size is strongly dependent on the wavelength;

- high luminosity
  AGN luminosity is in the range $(10^{42} - 10^{48})\, erg \cdot s^{-1}$ and, compared to a typical normal galaxy, can be 10^4 times as great. However, it is necessary here to consider the presence of the host galaxy, dust and relativistic beaming [2] ;

[1] For a complete analysis, see Krolik (1999)

[2] This cause a selection effect in favor of material moving towards the observer. Relativistic beaming will be discussed in the section "Relativistic beaming and superluminal motion"

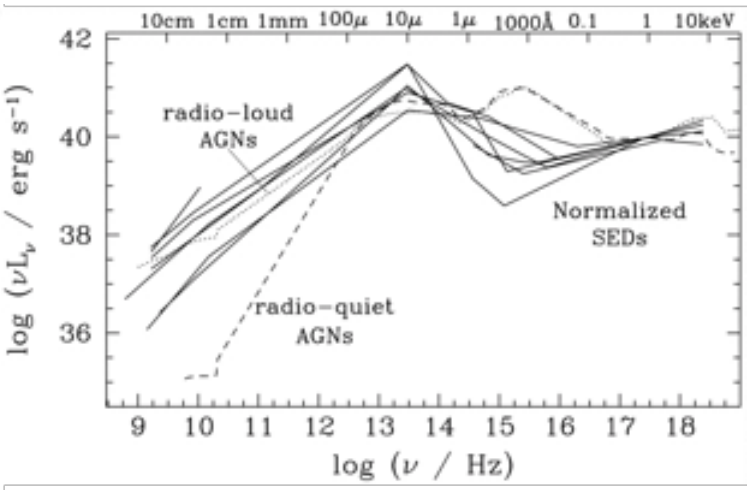

Figure 1.1. *Interpolated SED of seven low-luminosity AGN (solid lines) normalized to the 1 keV luminosity of M81. The sample is made by NGC 4261, NGC 4579, NGC 6251, M84, M81, M87, and NGC 4594. The median radio-loud (dotted line) and radio-quiet (dashed line) SED of luminous AGN from Elvis et al. (1994), normalized similarly, are overplotted for comparison. The broadband spectra of the low-luminosity AGN share a number of common traits, and they differ markedly from the SED of luminous AGN. (Ho, 1999).*

- broad continuum
  the continuum spectra is completely different from normal galaxy spectra, in fact the range over which the spectral energy distribution (SED is roughly flat is far broader than any normal galaxy's, more than a factor of 10^5 in frequency (fig. 1.1). For this reason, the spectra of AGN are usually characterized as a power law of the form $F \propto \nu^{\alpha}$ where α is the spectral index.
  Note that $F_\nu \nu$ is the typical variable used for the SED: it is specific flux multiplied by the frequency. Note that $F_\nu \nu = dF/dlog\nu = dF/dlog\lambda = F_\lambda \lambda$ is the best quantity to describe the bands in terms of energetics and eventual maxima, because it emphasizes the frequencies at which most of the power is emitted.
  Two features are almost ubiquitous in AGN spectra: an UV and an IR bump, interpreted as thermal emission respectively from an accretion disk surrounding a central engine and from warm dust at greater distances.
  In addition, the fraction of luminosity in the radio and X-rays band is generally larger;

- emission lines
  these are often very prominent, unlike a normal galaxy's where they are weak and predominantly in absorption. The UV spectrum of M87 is shown in figure 1.2. The nucleus of M87 displays a low ionization emission-line spectrum, which is well reproduced by a multicomponent photoionization scenario (Sabra et al., 2003). In addition, to emission lines, UV absorption features are seen in the spectrum, also characterized by low ionization.
  Lyα, the Balmer lines, the CIV 1549 doublet, [OIII] 5007 are almost always seen in AGN spectra. X-ray lines emission are often detected, the best-known of which is the iron Kα line around 6.4 keV (Reynolds & Nowak, 2003).
  What is extremely interesting is the line width distribution showing that some sources

have also broad lines ($FWHM > 10^3 km\,s^{-1}$), whereas others only narrow lines ($FWHM < 10^3 km\,s^{-1}$). The line width is interpreted as Doppler shift, giving an indication of gas motions in the emitting regions. In fact, forbidden lines which are collisionally suppressed are only seen with narrow profiles;

- variability
  the variability of AGN, especially in the optical band, is considered a defining characteristic that distinguishes these sources from normal galaxies. In general, there are not special timescales, unlike stars whose variability is dominated by some particular frequencies.
  The variability usually increases toward shorter wavelengths and for a small number of AGN is much stronger with a correlation with strong polarization, compact radio structure and strong high-energy emission in the gamma-ray band.
  The intensity variations in the optical and radio bands on timescales of months to years provided evidence for compact source in the nucleus. X-ray observations set tighter constraints on the upper limit to the size of the central engine by establishing that the X-ray luminosity can change by factors 2 with timescales of days, hours, and even minutes.

- polarization
  most AGN are weakly linearly polarized ($\simeq 0.5 - 2\%$) but just enough to distinguish the polarization from that of stars (due to dust transmission properties). A minority, including the minority with strong optical variability, are much more polarized $\simeq 10\%$;

- radio emission
  historically, radio emission was the first observed mark of AGN and unresolved cores with radio halos discovered in many radio sources were an indication of non-stellar activity in external galaxies. Then, in 1963 Maarten Schimdt realized that the bright optical point source associated with the radio source 3C273 had the, at the time incredibly, high redshift of 0.158, discovery that opened the field of active galaxies. Nowadays, many radio sources are associated with AGN, e.g. Virgo A with M87 and Perseus A with NGC 1275.
  In general, only about 10% of the radiation from quasars and AGN is emitted at radio wavelengths, with most of the power being radiated at submillimeter wavelengths. In contrast to the continuum at higher energies (far-IR up to far-UV), which is dominated by thermal emission, the radio emission must have a non-thermal origin. It shows indeed a spectrum characteristic of synchrotron radiation.

What can be inferred from their common properties is (Ferrarese & Ford, 2005):

- the spectral energy distribution is absolutely non-stellar, but is dominated by a non-thermal emission mechanism;

- AGN must be very massive, knowing the extremely large bolometric luminosities and the period of activity (up to 10^7 years) in which they consume an enormous amount of material;

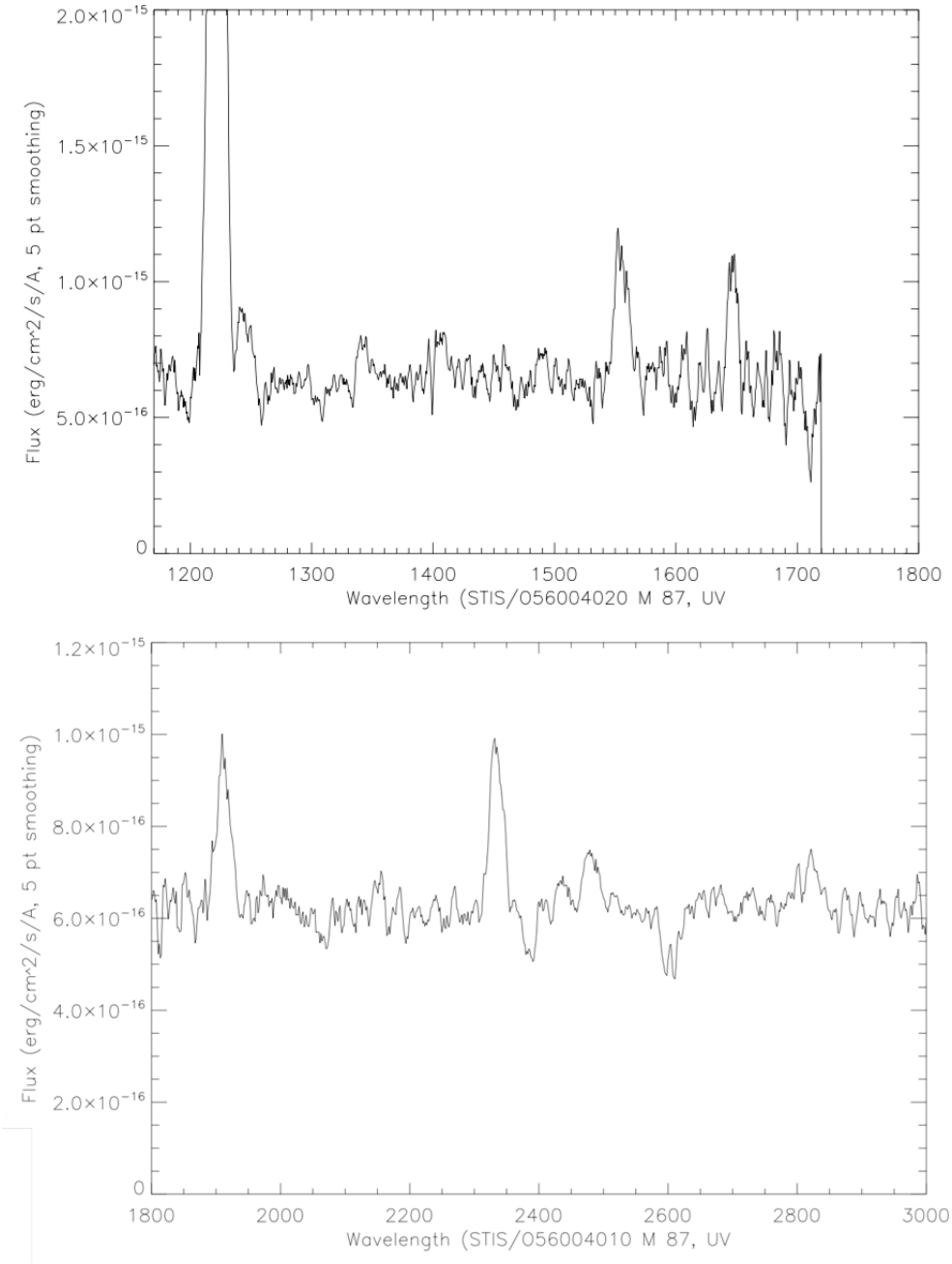

Figure 1.2. *UV spectrum of the nucleus of M87 from Space Telescope Imaging Spectrograph (STIS) on the Hubble Space Telescope (G140L grating, 52″ x 0.5″ aperture).*
Lines are 1216 Lyα, 1240 NV, 1400 SiIV, 1640 HeII, 1910 [CIII], 1335 CII, 2324 CII, 2800 MgII and the absorption lines are from both the Galaxy (foreground) and intrinsic to M 87.

- AGN are extremely compact, the flux variability confines AGN to within the distance that light can travel on time scale of less than a day, knowing that no signal can travel faster than light. This has significant implication for sources of energy that vary their output over time because, the maximum size L of an object varying with some characteristic time Δt is the distance that light could have traveled during that time, therefore $L \leqslant c\,\Delta t$.

Moreover, what can be inferred from their broadband continuum spectral energy distribution is (Koratkar & Blaes, 1999):

- the presence of dust in a range of temperatures and at a range of distances that is responsible for reprocessing the UV emission causing the IR bump;
- the presence of cold material that affects the X-ray region (fluorescence of the $FeK\alpha$ line and reflection) with a power law interpreted as inverse Compton scattering on photons by hot electrons in a region around the central engine.

Finally what can be inferred from their emission lines:

- the especially large widths of the broad lines interpreted dynamically indicate that they arise in a deep gravitational potential, which makes the broad lines especially valuable as probes of the central source. The region where these lines form is called broad line region (BLR); the absence of the broader component in the forbidden or semiforbidden lines, which are transitions collisionally suppressed, tells that the gas has a high density;
- the region where narrow lines form (NLR) is partially resolved in some of the nearest AGN, therefore it is possible to describe it as a region spatially extended and low-density.

1.2 The central engine as a black hole

The main issue about AGN has been finding what physical mechanism can provide extremely high luminosities from an extremely compact region. In fact, the effective way to derive energy is what all these sources have in common.
A very efficient mechanism that converts gravitational potential energy into radiation is the accretion onto a compact object. The black hole model was firstly introduced by Lynden-Bell (1969) and then supported by Rees (1984) to explain AGN activities.
The central object imprints unique dynamical signature on the motion of surrounding matter: within the sphere of influence, an orbital motion or velocity dispersion of stars or gas is unambiguous proof of the existence of a central mass concentration [3]. The case of a supermassive black hole (SMBH) is the most performant (Ferrarese & Ford, 2005). However, although nowadays the black hole model has achieved a widespread acceptance, its not yet fully confirmed because direct signatures of accretion onto SMBH are much harder to detect, as compared to their indirect signals.

[3] It has been observed relativistic velocities within a few Schwarzschild radii in the Fe Kα emission line in Type 1 AGN.

A SMBH is a black hole that does not originate from collapse of a star having a mass range of $(10^6 - 10^9)\, M_\odot$, far from the values of stellar black hole $(10 - 10^2)\, M_\odot$. SMBH are now believed to exist in the centres of most, or all, massive galaxies, but only 1% of them is active and only 0.1% has radio jets.
The mass and characteristic length scale for a black hole are interchangeable:

$$R_{SCH} = \frac{2GM_\bullet}{c^2} \simeq 3 \cdot 10^5 \, \frac{M_\bullet}{M_\odot} \; cm \simeq 2 \cdot 10^{-8} \, \frac{M_\bullet}{M_\odot} \; AU \tag{1.1}$$

where $M_\bullet$ is the black hole mass and R_{SCH} is the Schwarzschild radius, called also the event horizon. It is the gravitational radius of a spherical surface that defines a boundary [4].
To measure the mass of a black hole at the center of galaxies, there are direct methods as determination of circumnuclear ionized gas or star dynamics, stellar proper motion (for the Milky Way; Ghez et al., 2008) and study of H_2O maser emission (for the Sy 2 NGC 4258 case; Miyoshi et al., 1995).
However, the resolution that is necessary for the application of those methods is not possible for AGN. The reason is that most of them are distant. Moreover, the brightness of the active nucleus often overwhelms the stellar features in the host galaxy spectra and the gas can easily be perturbed by radiation pressure or shocks.
So, to provide the mass for AGN, indirect methods such as as gas-dynamical models are used (Kormendy & Ho, 2013).
Although the studies of supermassive black holes originated and evolved within the AGN context, modern SMBH searches have targeted almost exclusively quiescent or weakly active nearby galaxies. The reasons for this are the more simplicity in observations of the motion of the gas and stars surrounding the central object (Ferrarese & Ford, 2005). In summary, except for a handful of cases (the Milky Way and NGC 4258) statistical and systematic biases amount to a factor of a few in uncertainty in SMBH mass estimates.
Aside from mass, another parameter that features a black hole is the angular momentum J: it tells whether the black hole is rotating or not [5] . Defining an adimensional angular momentum per unit mass, it leads to the spin: $a = \frac{Jc}{GM_\bullet^2}$. If a = 0, the black hole is static, while if a = 1, the black hole is rotating with maximum angular momentum.
Due to spacetime curvature, it is not possible to have a stable circular orbit near the horizon and, moreover, rotating black holes have a more complicated horizon with a closer-in last stable orbit. In fact, the radius of the innermost stable circular orbit (ISCO), inside which material plunges into the black hole, depends sensitively on the black hole spin: for a static black hole $R_{ISCO} = 3R_{SCH}$, whereas for a maximally rotating black hole $R_{ISCO} = 9/2R_{SCH}$ or $R_{ISCO} = 1/2R_{SCH}$ for retrograde and prograde orbits respectively.
Providing a measure of the ISCO radius and an estimate of the black hole mass, the spin can

[4]This is valid for a non-rotating BH; for a rotating black hole there are two relevant surfaces, the event horizon, and the static surface, which completely encloses it. At the static surface, a particle would need to move at the speed of light in a direction opposite to the rotation of the hole in order to be stationary. In the region of space within the static surface and the event horizon, called the ergosphere, the rotating black hole drags space around with it in such a way that all objects must corotate with the black hole.

[5]The space-time around a static black hole is described by Schwarzschild metric, whereas the space-time around a rotating black hole is described by Kerr metric.

be inferred.

The energy from AGN is given by gravitational energy released by the accretion of matter falling onto the SMBH and converted to heat. Therefore, high quantity of emission in the form of radiation is provided from the central region.

1.2.1 Accretion disk

Stars and gas are observed to orbit about the centers of galaxies. When gas accretes toward the black hole located there, the gravitational force acting upon the gas increases as well as the centrifugal force. The key to the extraction of energy by material falling into a black hole is the presence of a significant angular momentum, typical of real astrophysical situation. The gas has almost certainly enough angular momentum to flatten into a rotating disk, known as an accretion disk, just like the gas in a binary system with mass transfer (Lynden-Bell, 1969). It is indeed expected that the matter orbiting around the central black hole, penetrate another inclined orbit plane and collide with other matter mixing the angular momentum and eventually concentrating on a single common plane.
Adjacent rings of gas scratch each other and the resulting friction allows the gas to move toward the black hole. This decelerating frictional force can originate from turbulence, magnetic field lines stretched between rings or the development of gas clouds, bars, and spiral arms in the outer parts of accretion disk.
Whatever its origin, this frictional force is responsible for heating the gas in the disk which can then radiate as a blackbody [6]. This process is several hundred times more efficient than the nuclear processes occurring in stars.
Matter pulled toward the black hole loses angular momentum that need be compensated by an angular momentum gain of the mass far from the centre in order to conserve the total angular momentum. The slow process transports angular momentum outwards providing heat generation through turbulent viscosity (Lynden-Bell, 1969; Shakura & Sunyaev, 1973).

In the most well-studied model, the disk is assumed to be physically thin and optically thick. This allows the maximum amount of heat to radiate away from the surface of the disk before matter crosses over the event horizon. Most of this energy will be released fairly close to the black hole, within a radius of typically 10^2 AU for massive black hole in a quasar. In order to fuel a bright quasar, gas must accrete at a rate of up to $10\,M_{\odot}/yr$.
In addition, a corona of hot material analogous to the solar corona forms above the disk and can up-scatter photons by inverse Compton up to X-ray energies. Finally, a large fraction of the primary emission may be obscured by interstellar gas and dust grains in the outer parts of the disk, but in a steady-state situation this will be re-radiated at some other waveband, typically IR.

[6] The emitted spectrum is a superposition of blackbody spectra of different local temperatures. For AGN the disk spectrum peaks in the optical-UV band, whereas for stellar black holes it peaks in the soft X-ray. The radiation from the accretion disk excites cold atomic material close to the black hole and this radiates via emission lines. If there is enough gas around the black hole, then the photons will be absorbed and reemitted several times before they escape.

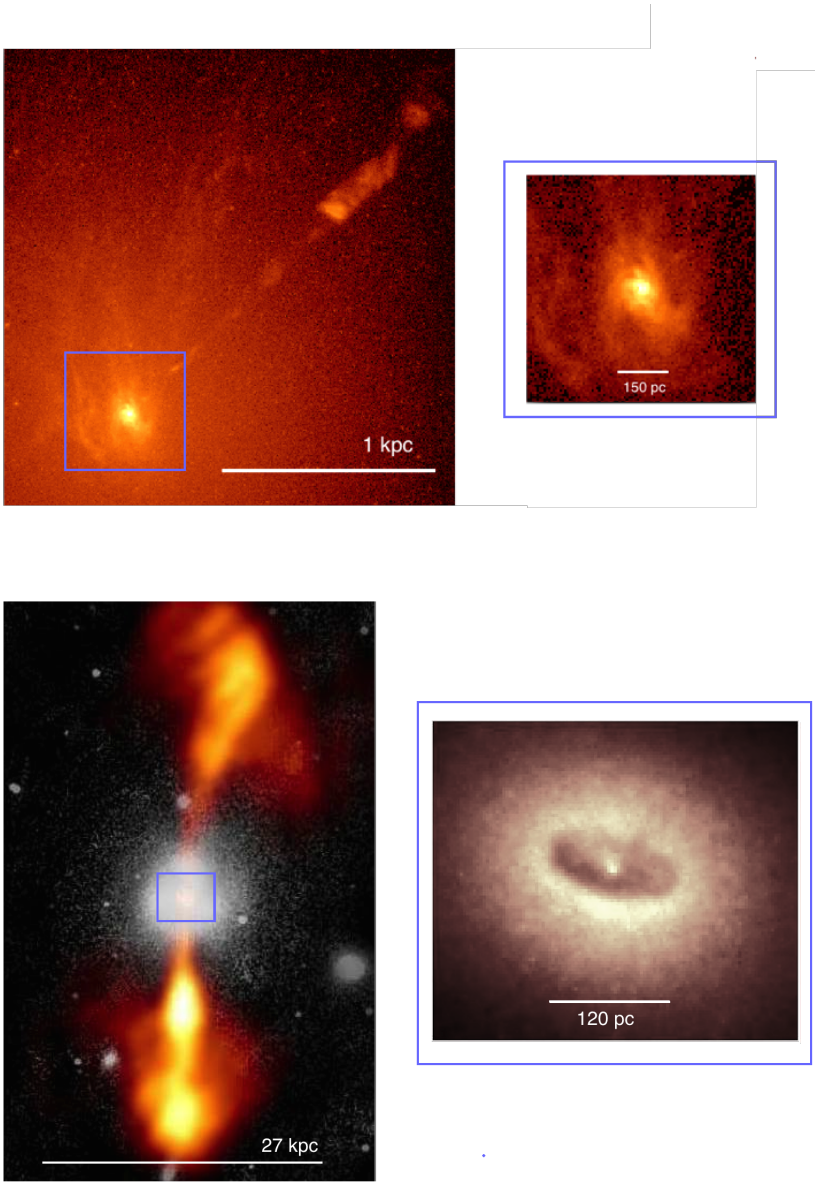

Figure 1.3. At the top, gas disk in nucleus of active galaxy M87, which will be discussed in the present work. On the left, it is possible to see also the jet. On the right, a zoom-in of the disk (Optical band 658 nm; instrument: Hubble Space Telescope Wide Field Planetary Camera 2, STScI).
At the bottom, the giant elliptical galaxy NCG 4261. On the left, a ground-based composite optical (white, 405 nm, instrument: LCO) and radio (orange, 20 cm, instrument: VLA) image where it is possible to see also the jets spanning a distance on the kiloparsec scale. On the right, a zoom-in of the core where the giant disk of cold gas and dust and what is inside it are clearly visible (V optical 547 nm, R optical 675 nm, IR 791 nm; instrument: Hubble Space TelescopeWide Field Planetary Camera 2, STScI).

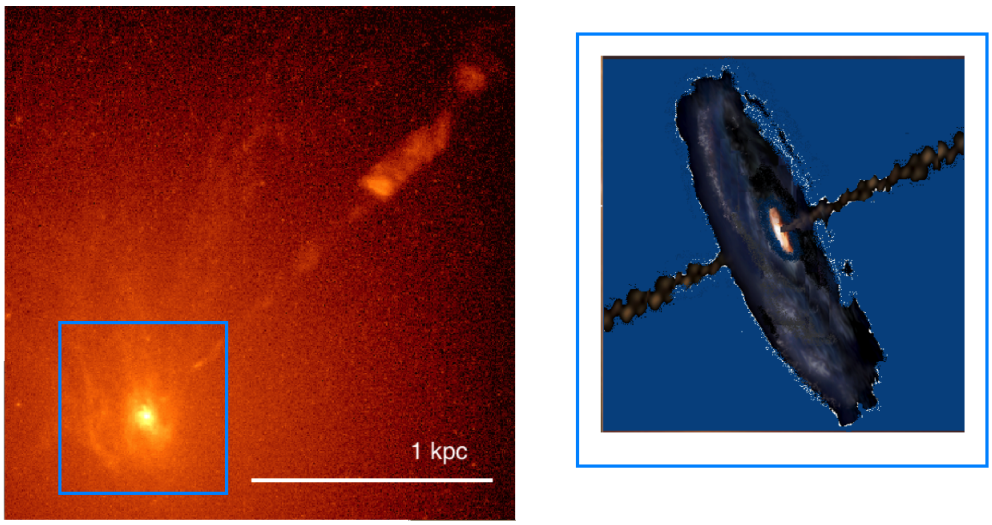

Figure 1.4. *Gas disk in nucleus of active galaxy M87 and its jet with the related approximate structure.*

1.3 The inferred structure

Let explain the approximate structure of an AGN schematized in fig. 1.4, inferred from observational features and proposed models:

- a supermassive black hole whose gravitational energy leads to the formation of an accretion disk, or more generally optically thick plasma, which glows brightly at UV and soft X-ray wavelengths; a corona of optically thin plasma might surround the disk producing medium and hard X-ray emission throughout inverse Compton scattering;
- clouds of gas moving rapidly in the potential of the black hole, whose gravity dominates the BLR; the emission lines formed here are broadened by Doppler shifts;
- a thick dusty torus or warped disk of gas and dust well outside the accretion disk and the broad-line region (fig. **??**), with a sea of electrons permeating the volume within and above the torus;
- narrow-line clouds farther from the dynamical center forming the NLR; the emission lines formed here present narrow profile and even forbidden transitions;
- collimated radio jets, if present, formed by outflows of energetic particles emanating from the central region, carrying gas from there to the outer parts of the galaxy and beyond; it is widely believed that these jets are launched perpendicular to axis of the accretion disk.

The narrow components have Doppler widths usually less than around $10^3 kms^{-1}$; these emission lines arise in relatively low-density ($n_e \simeq 10^3 cm^3$) gas that is spatially extended. In contrast, the broad components have Doppler widths in the range $(10^3 - 2.5 \cdot 10^4 km)\, s^{-1}$ and arise in gas of fairly high density by nebular standards ($n_e > 10^9 cm^3$), as determined from the weakness of certain metastable and forbidden lines that are relatively more prominent in lower-density gases (Peterson, 2006).

	Mass	**Schwarzschild radius R_{SCH}**
BH	$10^6 - 10^9 M_\odot$	$0.01 - 10$ AU

	Distance from the BH	**Distance from the BH (cm)**
Accretion disk (inner radius)	$0.01 - 60$ AU	$10^{11} - 10^{15}$
Accretion disk (outer radius)	$1 - 10^3$ AU	$10^{13} - 10^{16}$
BLR	few light weeks $-$ 1 ly	$10^{16} - 10^{17}$
Inner radius of the torus	$\simeq 1$ ly	10^{18}
NLR	$\simeq 10^2 - 10^4$ ly	$10^{18} - 10^{20}$
Radio jets	$1 - 10^7$ pc	$10^{17} - 10^{24}$

Table 1.1. Typical values for AGN components (Beckmann & Shrader, 2012).
$1pc \simeq 3.26\,ly \simeq 2 \cdot 10^5 AU$
$1AU \simeq 1.5 \cdot 10^{13} cm$
$1M_\odot = 2 \cdot 10^{33} g$
$R_{SCH} = \frac{2GM_\bullet}{c^2}$

Note that in both the NLR and the BLR, the gas moves supersonically.

In tab. 1.1, the typical, approximate values for these AGN components are shown. Note that for the black hole, knowing the mass implies knowing the size, while for the other components (the accretion disk, the broad- and narrow-line region, and the extension of the absorber), it is more difficult to estimate the size because these are model-dependent. Finally, the size of the jet is easier to determine as one is able to observe it directly in the radio domain.

This is the standard picture for active galactic nuclei and, according to the current "AGN paradigm", the properties of the nuclear activity can always be reproduced by slightly modifying, rather than completely revising, this basic picture. Changes in the angle at which the AGN is observed, in the spin and mass of the black hole, in the accretion rate, and in the kind of interactions between the source and the surrounding medium, account for the various types of AGN (Ferrarese & Ford, 2005), leading to the unified scheme.

1.4 Classification and the unified scheme

A basic and extreme distinction is between radio-loud and radio-quiet AGN.
The first ones are characterized by prominent radio jet and/or lobe emission and they are roughly $15 - 20\%$ of AGN (Urry et al., 1995). The twin jets have relativistic motion, at least near to the central source, that produces synchrotron emission. This configuration leads to radio galaxy and radio quasar classification.
However, if the jet opening angle is small, that is the jet is pointing towards the observer's line of sight, then a relativistic effect will change its features beaming the emission into a cone whose aperture depends on the jet speed. This effect is known as relativistic beaming and in this case, the observer will see a blazar.
The presence of a relativistic jet constitutes a fundamental distinction between various types

of AGN, simply because an anisotropic and strongly Doppler-boosted jet emission can dramatically affect the observed properties of a source.

Radio-quiet AGN are usually classified according to their luminosity and/or optical spectra features:

- Seyfert galaxies, with optical nuclear continuum emission; they can have strong nuclear X-ray emission and a weak radio jet without extended lobes. They are divided into two types: Seyfert 1, which present also broad emission lines, and Seyfert 2, which present only narrow lines. The host galaxies are usually spiral or irregular galaxies;

- Radio-quiet quasars (RQQ), called also quasi-stellar objects (QSO), are more luminous than Seyfert galaxies. RQQ always show strong optical continuum emission, X-ray continuum emission, and broad and narrow optical emission lines. Their host galaxies can be spirals, irregulars or ellipticals. Among them, it should be mentioned other two classes: broad absorption lines (BAL) quasars, which are approximately 10% of the QSO population (Gallagher, 2002) and exhibit deep, broad absorption lines from high ionization ultraviolet resonance transitions and infrared (IR) quasars, characterized by luminosities in the infrared band $> 10^{12} L_{\odot}$ (also known as ULIRG, that is Ultra Luminous IR Galaxies; Hao et al., 2005);

- Low-Ionization Nuclear Emission Regions (LINERs), characterized by low luminosity and strong emission lines especially from low-ionization stages, more than in Seyfert galaxies. In term of activity, LINERs are on the borderline and it is still a matter in hand whether these galaxies are truly active or not.

Radio-loud AGN are divided in:

- Radio-loud quasars (RLQ), similar to RQQ with the addition of emission from a jet, together with nuclear and often extended radio emission;

- BL Lac objects, quasars distinguished by lack of strong emission or absorption lines in their spectra are named after their prototype, BL Lacertae. They are characterized by a large and extremely rapid variability in optical and radio brightness within a few days. If, in addition, they present stronger emission lines, they become optically violently variable (OVV) quasars. These and the BL Lac objects are collectively known as blazars. Note that all known blazars are radio-loud and they appear as the most luminous objects in the Universe;

- Radio galaxies, with both nuclear and extended radio emission found essentially always in elliptical galaxies. On the base of optical spectra, two types of radio galaxies were classified: broad-line radio galaxies (BLRG) and narrow-line radio galaxies (NLRG). They were also distinguished into two luminosity classes with distinct morphology (FR 1 and FR 2; see the "Radio galaxies" section).

In addition, an empirical classification is based on the observed properties of their optical and ultraviolet spectra. It allows a separation of AGN into three types (tab. 1.2) that may be explained by simple geometrical effects involving anisotropic obscuration of the active center viewed at different inclination with respect to the accretion disk axis (Antonucci, 1993):

Galaxy Type	Active Nuclei	Emission Lines Narrow (10^3 km/s)	Emission Lines Broad (10^4 km/s)	X-rays	UV (excess)	Far-IR (excess)	Radio	Jets	Variable	Radio loud
Normal	no	weak	no	weak	no	no	no	no	no	no
Starburst	no	yes	no	some	no	yes	some	no	no	no
LINERs	yes	yes	no	weak	no	no	no	no	no	no
Seyfert I	yes	yes	yes	some	some	yes	few	no	yes	no
Seyfert II	yes	yes	no	some	some	yes	few	yes	yes	no
Quasar	yes	yes	yes	some	yes	yes	some	some	yes	10%
BL Lac	yes	no	no	yes	yes	no	yes	yes	yes	yes
OVV	yes	no	faint	yes	yes	no	yes	yes	yes	yes
Radio galaxy	yes	some	some	some	some	yes	yes	yes	yes	yes

Figure 1.5. *The AGN taxonomy first created by Krolik (1999) and then updated by De Gasperin (2012). The comparison is made also with normal and stardust galaxies.*
Note that BL Lac and OVV are called Blazars and radio-quiet quasar are sometimes called QSO.

- Type 2 have permitted and forbidden lines from low-ionized and low-density gas, with typical line widths $\leqslant 10^3\, km\, s^{-1}$;
- Type 1, in addition, have permitted lines from a higher density region, with typical line widths $\simeq 10^4 km\, s^{-1}$ and strong variable featureless continua;
- Type 0 have unusual characteristics due to relativistic beaming.

The point is that AGN look differently from different aspect angles, due to the presence of the obscuring torus or warped disk (type 2) and the eventual presence of jets, whose plasma is relativistically beamed (type 0). From type 2 to type 0 the angle respect to the line of sight is decreasing: from 90 to 0 degrees, in other words the observer look towards the torus for type 2 and looking towards the jet axis for type 0.
An other feature that does not depend on the object itself, but on the observation, is the possibility to see the host galaxy: when the host galaxy is visible, the AGN is called Seyfert galaxy, whereas when it is not, it is called quasar. Seyfert nuclei are on average two orders of magnitude less powerful than quasars, so the luminosity of the AGN does not overwhelm the starlight and it is possible to see the host galaxies.
For years, it has been looking for a single and basic model that would explain the diversity observed among active galaxies.
The current scheme is based on the orientation of the AGN, instead of its physical properties, because its appearance depends strongly on the angle respect to the observer. The orientation relative to the line of sight is crucial for the variety in AGN types, therefore the distinctions are based on an observational construction.

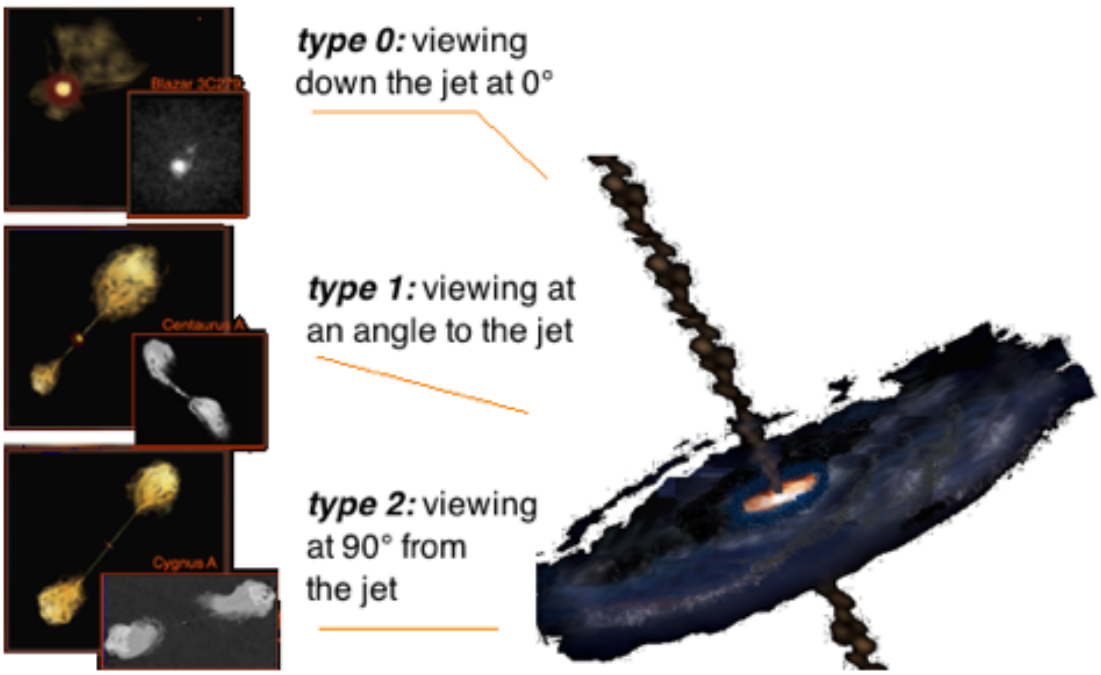

Figure 1.6. *Representation of an AGN with jets, adapted from Fermi GLAST image (http://www.nasa.gov/fermi).*
This shows how much our classification of AGN depends on the angle respect to the line of sight.
1) *At 0 degrees, looking down the jets, the emission is dominated by high-energy photons (X-rays, gamma rays) and the AGN is a Blazar. As an example, it is shown the gamma-ray image of 3C279, one of the brightest gamma-ray object in the sky; the faint source just above to the upper right is blazar 3C273 (Instrument: CGRO EGRET, credit: EGRET team, NASA/GSFC).*
2) *Viewing from a different angle, the linear jets are clear and the central source is detectable in X-rays down to radio. As an example, it is shown the radio image of Centaurus A, a nearby radio galaxy (Instrument: VLA, credit: NRAO/AUI).*
3) *When seen from the side, the relatively weak emission from the lobes becomes apparent and huge clouds of radio-emitting gas are seen over 100 kpc from the black hole. The central region can be seen as just a point-like source. As an example, it is shown the radio image of the radio galaxy Cygnus A, one of the strongest radio sources in the sky (Instrument: VLA, credit: NRAO/AUI).*

Type	Features	Radio-loud	Radio-quiet	L
2	narrow emission	NLRG FR1	Seyfert 2	Low
	lines and weak continua	NLRG FR2	IR quasars	High
1	broad emission	BLRG FR2	Seyfert 1	Low
	lines and bright continua	RLQ	RQQ	High
0	unusual spectral characteristics	Blazars	BAL quasars	

Table 1.2. AGN taxonomy based on optical emission line properties. Note that from type 2 to type 0 the angle respect to the line of sight is decreasing.
L = luminosity
NLRG = Narrow Lines Radio Galaxy
BLRG = Broad Lines Radio Galaxy
FR = Faranoff-Riley
IR = Infrared luminous
RLQ= Radio-loud quasars
RQQ= Radio-quiet quasars (or QSO="quasi stellar object" that is a term still occasionally used)
BAL = Broad absorption lines

1.5 Radio galaxies

Galaxies which are identified with strong radio sources in the range of $(10^{41} - 10^{46})\, erg \cdot s{-}1$ are generally referred to as radio galaxies.
Two types of radio galaxies have optical spectra of the sort that we identify with AGN activity: broad-line radio galaxies (BLRG) and narrow-line radio galaxies (NLRG). They show bright optical emission lines in their spectra: the first are characterized by very broad H and He features with line widths up to 25000km/s, whereas the latter show typical line widths of 1000 km/s, including both forbidden lines (O, N, S, Fe) as well as the Balmer lines.
BLRG and NLRG are considered the radio-loud counterpart of Seyfert galaxies (respectively type 1 and 2), in terms of basic phenomenology. As a class, they have a number of differences from Seyferts, one of this is that they appear to occur in elliptical galaxies rather than spirals. In fact, strong radio sources are typically identified with giant elliptical galaxies, although some of the brightest radio sources are associated with quasars.
In nearly every case, in the host galaxy there is evidence of a significant departure from the simple structure expected in an elliptical. One can see the presence of disk-like structures, spiral arms and on occasion multiple nuclei (Mahabal et al., 1999).
In radio galaxies it is possible to find different types of radio features:

- lobes, large-scale structures on either side of the host galaxy, fairly symmetrical and ellipsoidal where there is back-flow of the shocked jet material (perhaps mixed with the surrounding extragalactic gas); they are often several hundreds kiloparsecs in length and can be separated from the galaxy by a similar distance; the stronger the radio source, the bigger the lobes tend to be;

- plumes, much more elongated, present in low-luminosity sources;

- hotspot, typical of high-power radio sources, are small and high surface bright regions where a jet meets the ambient medium and decelerates through a shock transition; often spots of infrared or optical continuum emission can be detected in the same region of a radio hotspot;

- jets, long narrow collimated structures coming from close to the active nucleus and going to the lobes; they can be smooth or characterized by discrete blobs, called knots.

The radio emission structure can be classified as extended or compact: the extended structure is transparent, whereas the compact one has a so high electron density that the source becomes opaque to its own radiation (see self-absorption in the "synchrotron emission" section). The first have steep spectra and they are typical of long-wavelength radio surveys, whereas the latter have flat spectra and are most easily detected by radio surveys at short wavelengths.
The active nucleus is seen as a core radio source, only a few parsecs across. The cores, in contrast to the lobes, are brightest at higher radio frequencies. Therefore, if a source is lobe-dominated has a dominating extended structure, whereas a source is core-dominated has a dominating compact structure.

The conventional measure of radio loudness is the ratio between the specific flux in the radio band and the optical band:

$$R = \frac{F_\nu^r}{F_\nu^{opt}} \tag{1.2}$$

where the wavelength chosen for F_ν^{opt} is 4400 Å.

When the flux is characterized by extended lobes, the spectrum is well determined by this power law:

$$F_\nu \propto \nu^\alpha \tag{1.3}$$

where α is the spectral index. It is in the range from -1.3 to -0.5 for extended radio features (Verschuur & Kellermann, 1988). The spectrum usually becomes more steep at high frequency. The spectrum results flatter in core-dominated sources. However, the correlation between morphology and spectrum is not always valid.
It is important to note that the numbers of flat and steep sources depend on the selection effect: low-frequency detection finds more steep spectra, while high-frequency flatter spectra. Moreover, steeper sources tend to be at higher redshift.
In all resolved radio structure, the radiation is linearly polarized until few tens of percent. The polarization direction depends on the position within the source, so different angular resolution can measure different fractional polarization.

1.5.1 FR1 vs FR2

Radio galaxies have been distinguished into two luminosity classes with distinct morphology by Faranoff and Riley (1974). They noticed that the position of high and low surface brightnes regions in the lobes of extragalactic radio sources is correlated with their radio luminosity.

The luminosity distinction is based on the value at radio frequency of 178 MHz: $L_{178} \simeq 2 \cdot 10^{25} W\, Hz^{-1}$ (Urry et al., 1995). Actually, this is clear in the optical as well as in the radio range.
An other distinction is due to the morphology of the radio jets. FR1 and FR2 both have pairs of jets, but FR2 jets are more collimated with large and diffuse radio lobes characterized by strong hotspots and/or bright edges. The morphology of the FR1 is not so well defined, with atypical radio structures, like edge darkened plumes; anyway, this class shows a lack of hotspots but a compact emission arising from close to the core and then growing dimmer. In fact, the surface brightness of the lobes decays going away from the galaxy, contrary to that in high-power sources. Moreover, the jets are often bent. In fact, FR1 are usually found in clusters where the ambient medium with the low-velocity jets creates distortions, oscillations and curvatures, whereas FR2 are often isolated or in poor groups of galaxies.

To summarize:

- FR1 are low-luminosity with $L_r < L_{178}$, but, at a given radio luminosity, are more optically luminous; a jet can be seen on both sides of the nucleus but the sources become fainter approaching the outer edges of the lobes; FR1 sources are associated with bright, large elliptical galaxies (D or cD) that have a flatter light distribution than an average

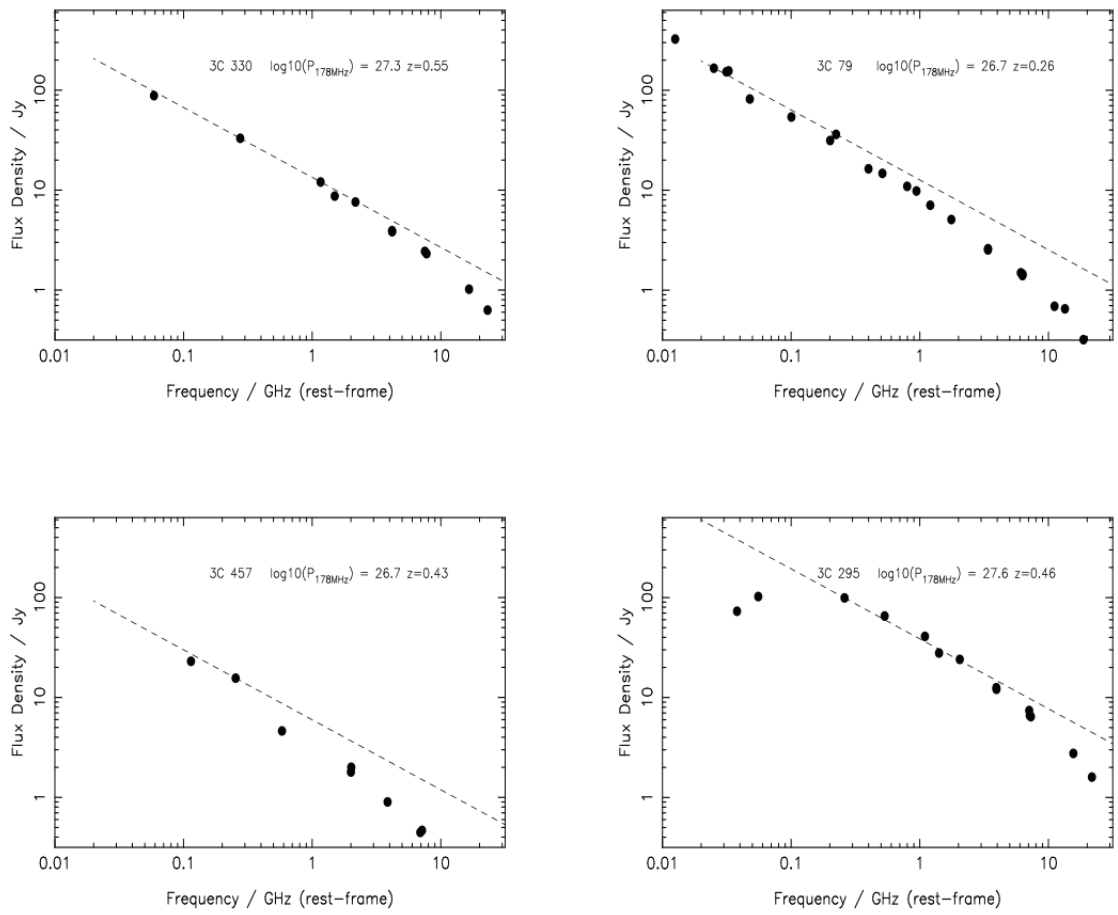

Figure 1.7. *Example of four FR 2 radio galaxies. Observed data are points and the dashed line indicates slope of spectral index equal to -0.7. (Jackson & Wall, 2001)*

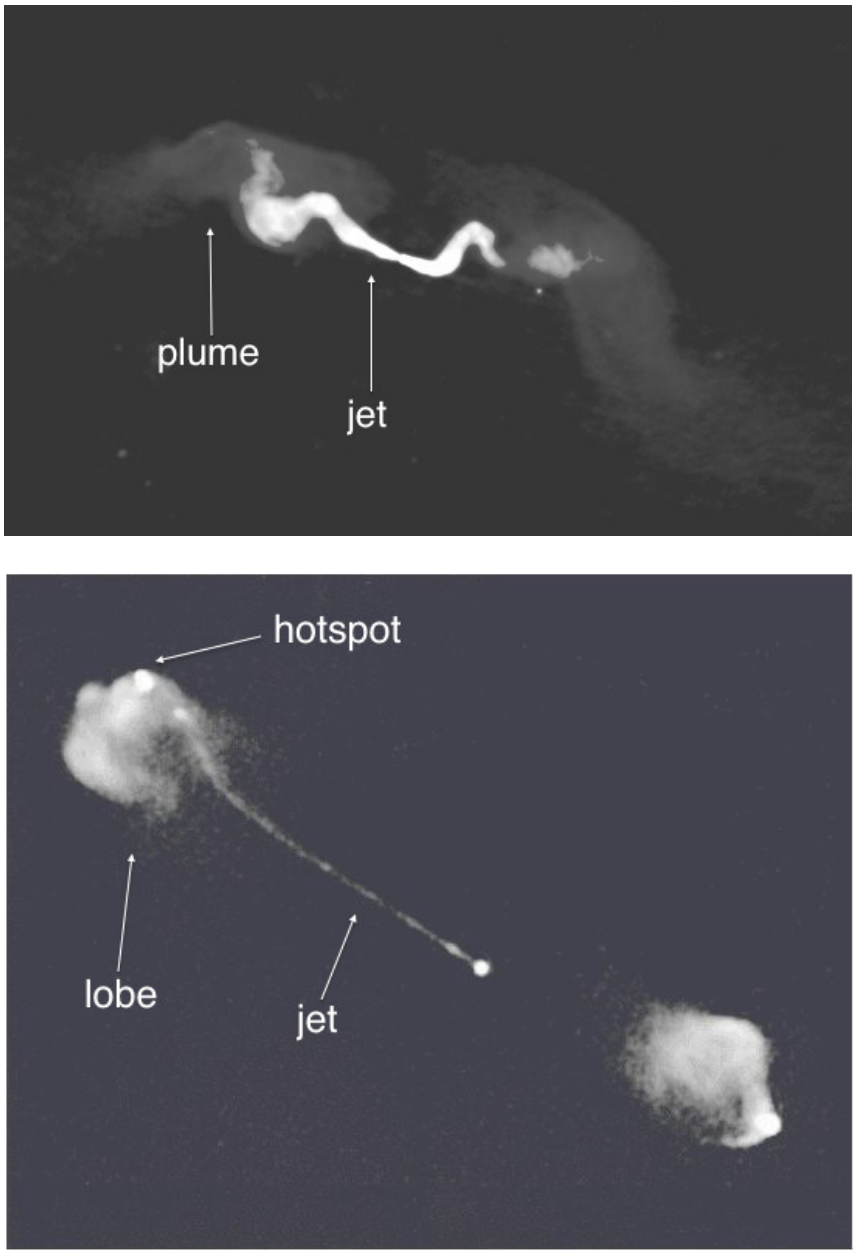

Figure 1.8. At the top, it is shown the radio galaxy 3C31 as an example of FR 1 type (Instrument: VLA, 20 cm). FR 1 class presents jet dominated emission, two-sided jets and they are typically found in clusters and weak-lined galaxies.
At the bottom, it is shown the radio galaxy 3C175 as an example of FR 2 type (Instrument: VLA, 6 cm). FR2 class presents lobe dominated emission, one-sided jets with relativistic velocity on all scales and they are found isolated or in poor groups in strong emission lines galaxies.
What suddenly strikes is the different morphology of the jets: 3C31 presents bending jets and irregularly shaped plumes, which stretch to a distance of 300 kpc from the center of the galaxy; 3C175 has collimated jets terminating in brighter lobes with hotspots. Actually, only one of the jet is visible in 3C175, the jet that is pointing toward the observer line of sight, with an extension of the order of Mpc (the entire radio source is approximately 200 Mpc end-to-end and the bright central source is the optical quasar (z = 0.77).).

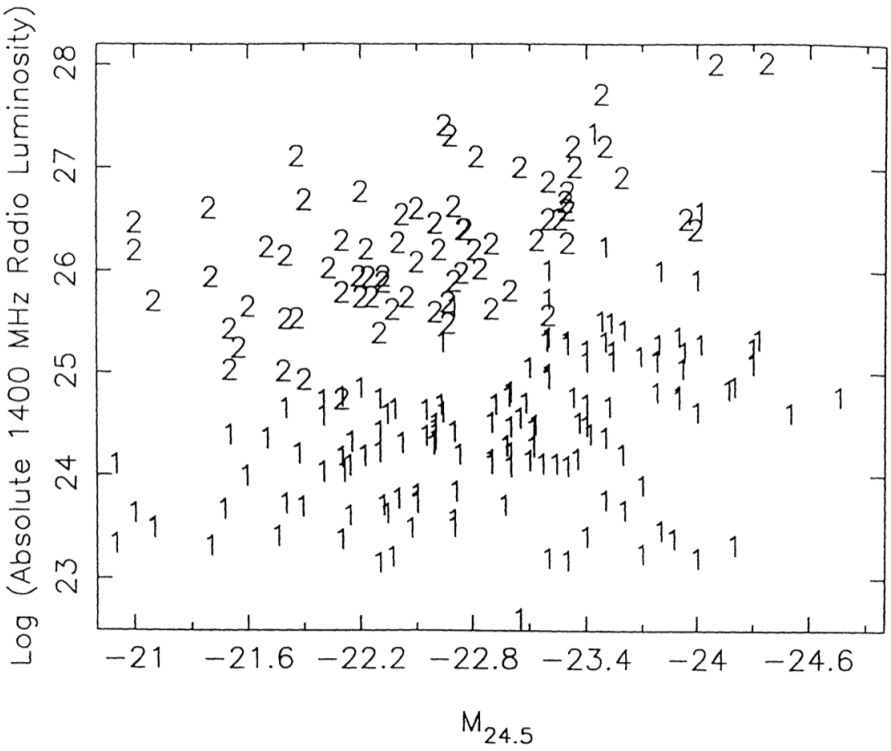

Figure 1.9. *FR1 and FR2 classes, 1 and 2 respectively, as a function of radio luminosity at 1400 MHz ($W \cdot Hz^{-1}$ radio units) and optical absolute magnitude in R band (Owen & Ledlow, 1994). For a given radio luminosity, there is an optical luminosity limit that separates the two types of source.*

elliptical one and are often located in rich clusters with extreme X-ray emitting gas (Owen & Laing, 1989; Prestage & Peacock, 1988). As the galaxy moves through the cluster, the gas can distort the radio structure through ram pressure, which explains why narrow-angle-tail or wide-angle-tail sources appear to be derived from the FR1 class of objects;

- FR2 are high-luminosity with $L_r > L_{178}$, but, at a given radio luminosity, are less optically luminous; the jets are brighter than those in FR1 but weak compared to the lobes and they are often one-sided. FR2 sources are generally associated with galaxies that appear normal, except that they have nuclear and extended emission line regions. The galaxies are giant ellipticals, but not first-ranked cluster galaxies.

The distribution of FR1 and FR2 radio galaxies as a function of their optical and radio luminosity is shown in figure 1.9. As found out by Owen and Ledlow, there is a clear diagonal division of the types that means the radio luminosity at the division between the classes increases with optical luminosity. The diagonal boundary is given approximately by $L_r \propto L_{opt}^2$. When the two-dimensional distribution of points is projected onto the radio luminosity axis, the two types remain separated but with some mixing at the boundary. Sources fainter than this limit are FR2, while those brighter than it are FR1.
Focusing on the emission of the nucleus, Chiaberge (2000) found a correlation between radio and optical nuclear luminosity for FR1. This means that they have not a torus, whereas FR2 do have. These radio galaxies could be inherently different sources, caused by a different efficiency in the accretion process.

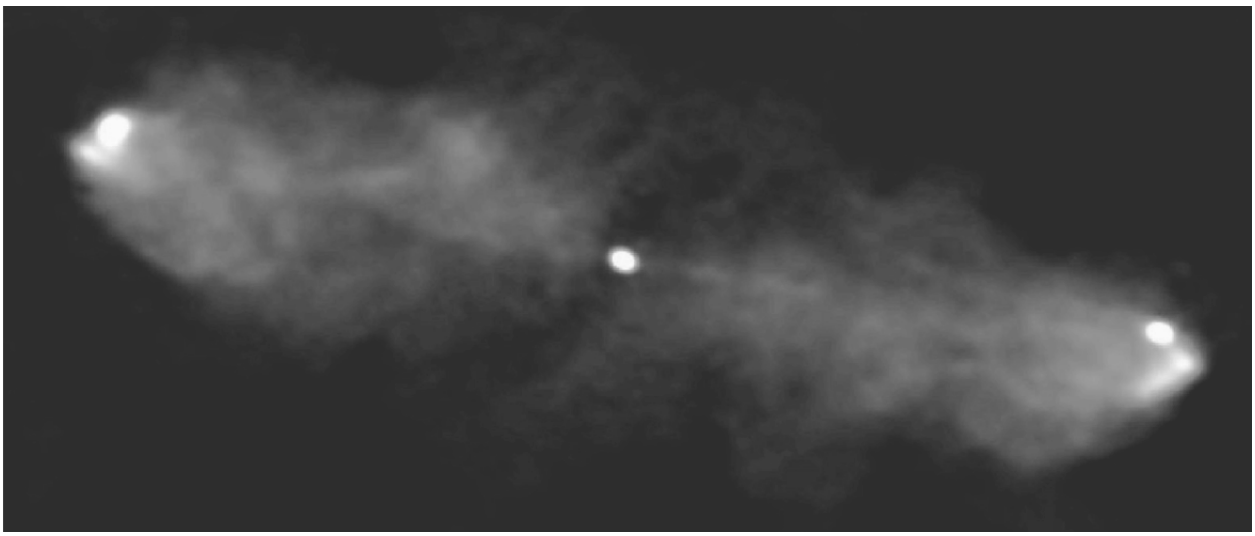

Figure 1.10. *Classical double radio galaxy 3C452 (Instrument: GMRT, 1314 MHz)*

1.5.2 Radio structure and emission

Names are given to several particular types of radio source based on their radio structure:

- Classical double
  refers to a FR2 source with regions of synchrotron-emitting plasma that can extend to thousands of kiloparsecs terminating in clear hotspots, as shown in fig. 1.10. These radio galaxies are thought to be powered by narrow collimated jets. Regions of low surface brightness emission lying between the galaxy center and the hot spots, called radio bridges, are believed to be a result of the accumulation of relativistic particles accelerated at the hot spots over the lifetime of an FR 2 source that form a low-density cocoon around the jet (Kharb et al., 2008)

- Fat doubles
  are sources with diffuse lobes but neither jets nor hotspots. Such sources may be relics whose energy supply has been permanently or temporarily turned off. Fat double lobes in this giant radio source are a result of the ejection and deposition of synchrotron plasma over a wide range of angles over time rather than the expansion of relic lobes. (Subrahmanyan et al., 2006)

- Tailed radio galaxies

  have the same morphology of that in double radio galaxies but distorted by motion through an intracluster medium; in fact, these sources occur in clusters of galaxies, preferentially in high-density regions of the intracluster medium, where the X-ray intensity is high. Even cluster mergers were made responsible for the formation of tails, which always occurs in their radio emission [7], usually far beyond the optical extent of their host galaxies. Tailed radio galaxies, whose examples are shown in figure 1.11, can be subdivided into wide-angle (WAT) and narrow-angle tailed (NAT) types, referring to the opening angle between the two opposite jets emanating from the nucleus of the

[7] It is important to remember that these object are totally different from optical tails due to tidal interactions shown in normal galaxies

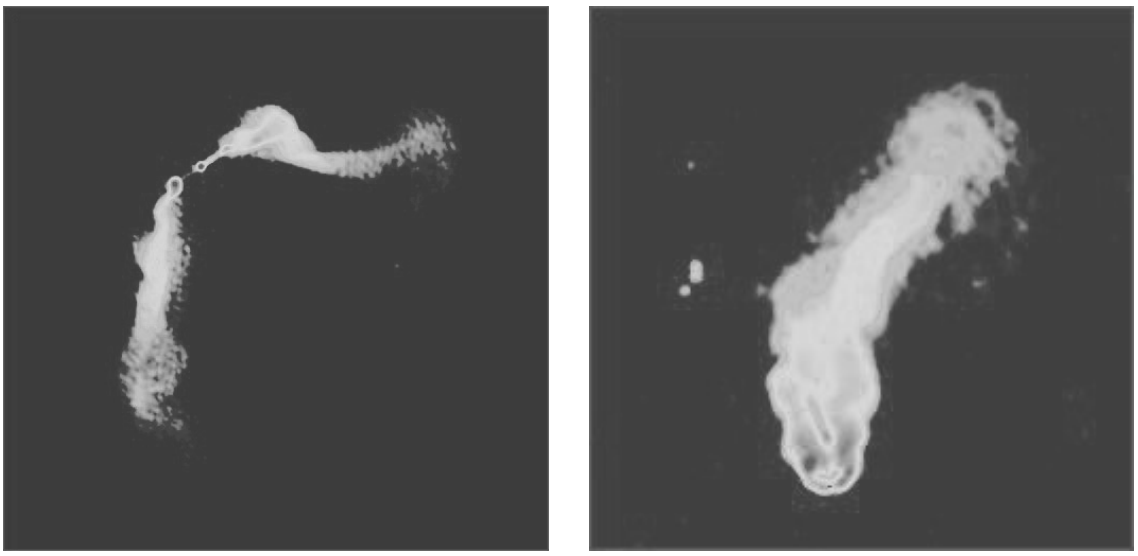

Figure 1.11. On the left side, prototypical WAT source 3C465 at the center of the rich Abell cluster of galaxies A2634 (Instrument: VLA, 20cm)
On the right side, NAT source NGC1265 (Instrument: VLA, 20cm).

optical galaxy.

Wide-angle tail (WAT) normally refers to a source intermediate between standard FR1 and FR2 structure, with efficient jets, in case hotspots and with plumes rather than lobes. It is usually found in clusters, whose radio jets have been bent into a "large C shape", and there is a significant interaction the intracluster environment. In fact, the jet bending can be interpreted as the action, on the jets, of ram pressure from the high velocity motion of the associated active elliptical galaxy through its surrounding intracluster medium (ICM). This interpretation was first developed by Begelman, Rees, Blandford (1979) and applied by a number of investigators (e.g. Pinkney et al., 2000). In addition to ram pressure, buoyancy forces were introduced to explain this phenomenon: if the jet density is lower than the density of the surrounding medium, buoyancy forces will drag the jets towards regions of the ICM where the densities are equal (Smolčić et al., 2009).

Narrow-angle tail (NAT) or head-tail (HT) source describes an FR1 with a high brightness head that coincides with the nucleus of a giant elliptical galaxy and an elongated radio tail that often extends for several hundred kiloparsecs. Above all, it appears to be bent by ram pressure as it moves through a cluster. In fact, a NAT is almost always associated with a cluster of galaxies. The combination of high ambient density and modest speeds of the host galaxy with respect to the ambient medium are able to produce the bends.

However, the distinction between WATs and NATs depends strongly on the angular resolution and the distance to the radio source. A classic example is the tailed NGC 1265, which may be called a WAT at high resolution, but appears as a NAT at lower resolution.

1.5.3 Radio jets

Powerful and collimated jets of relativistic particles are found in radio-loud sources, that are $\simeq$ 10% of AGN. They can extend up to hundreds of kiloparsecs or even megaparsecs further away from the host galaxy, providing an important mechanism for redistributing matter and energy on large scales affecting galactic evolution.

The term "jet" for an extragalactic object was first used by Baade and Minkowski in 1954 to describe an "apparent flow" of optical knots from the core of M87, recalling droplets in a fluid. After that, radio detection of these optical structures led to a description of radio jets, as narrow features between compact central core and extended lobes. Actually, jets are most prominent in radio band observations, thanks to the resolution obtained by long baseline interferometry.

Jets are formed by an outflow of energetic and collimated plasma, which emanates from the region near the active nucleus. They appear with different aspects in length, curvature and morphology, sometimes due to projection effects. On the other hand, they are always characterized by a broad and non-thermal continuum from the synchrotron emission from particles in the jets.
What supports the idea that jets are formed with a process common to all extragalactic radio sources is that they can be found in sources of all luminosities, size and structures.
The existence of powerful and extended extragalactic radio objects implies the presence of a great energy reservoir and the possibility to transfer and then carry this energy into space.

What makes a narrow feature a jet is (Bridle & Perley, 1984):

- its length, which must be at least four times as long as its width;
- the possibility to separate at high resolution the jet from other extended sources, if any, either by brightness contrast or spatially;
- its alignment with the compact radio core in proximity to it;
- if made of knots, they must be more than two or elongated along it.

A distinction in morphology is the sidedness of the jets, in other words whether the jets are seen on both sides of the nucleus or only on one side. Then, they can be one-sided (like M87), two-sided (like 3C31, fig. 1.8 at the top) or one-sided at some distance from the active nucleus and then two-sided (like 3C129, fig. 1.12).

The most plausible mechanisms for powering extragalactic jets involve material being drawn inward by the strong gravitation of the black hole forming rapidly-spinning flat disk. Here, it occurs the extraction and conversion of the black hole rotational energy through the Blandford-Znajek (BZ) process (1977), whereby magnetic field lines cross the black hole event horizon, reconfiguration themselves in a helical configuration and launch outflows along the disk axis. In fact, a fundamental parameter is the magnetic field configuration: when the bulk of torus material reaches the innermost region close to a central black hole, a magnetically driven jet

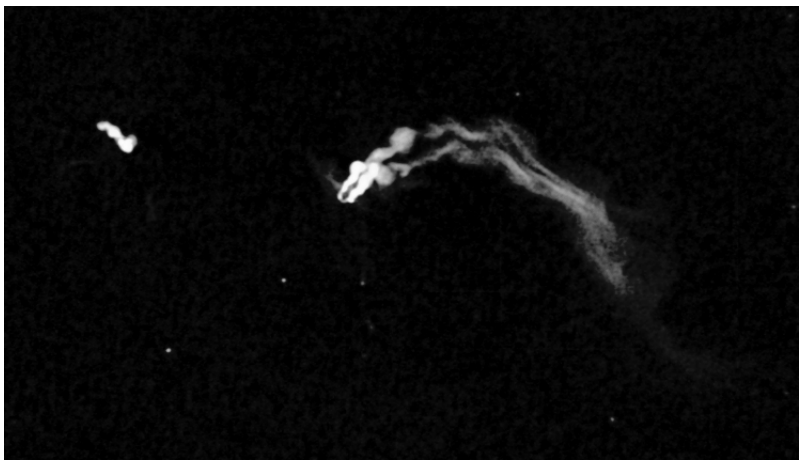

Figure 1.12. *Wide-field 90 cm image of the large narrow-angle tail radio galaxy 3C129. The bright source on the left is 3C129.1 (Lane et al., 2002).*

emerges. This magnetic jet is derived by vertically inflating toroidal fields with poloidal (vertical) fields, in a sort of magnetic tower (Kato et al., 2003). The collimation width of the jet depends on external pressure, pressure of ambient medium.
The more recent models assume a spinning black hole as a required in the BZ process as the fundamental ingredient for a jet (McKinney, 2006). In addition, an orbital angular momentum of the accretion flow antiparallel (retrograde) rather than parallel (prograde) respect to the black hole spin is more likely to form the jet (Garofalo, 2009).
As the disk spins, magnetic field lines are twisted tightly and then channel the electrically-charged particles into a pair of narrow jets. The geometry is called bipolar, meaning a jet symmetry between the sides of accretion disk. In order to collimate them, the accretion disk also launches a wind via the Blandford-Payne (BP) mechanism (1982). This BZ/BP combination forms a spine/sheath morphology, in which a narrow, electromagnetic, and initially non-radiative jet from the black hole is surrounded by a slower outflow originating from the inner disk. The jet acceleration probably occur gradually going away from the disk, otherwise in the inner region the jet particles would lose energy through inverse Compton scattering with the photons of the dense radiation field.
Inside the jet, shock waves produce high-energy electrons that spiral around the magnetic field lines and radiate by the synchrotron process, creating the observed radio, optical and X-ray knots on kiloparsec scales. The features in all the different bands are often closely aligned, as proved by the M87 jet (fig. 2.2). After dissipation for viscosity thermal emission in UV, optical and IR bands and IC emission from the hot corona above the disk.

Physical models of extragalactic jets is hampered by the impossibility of measuring directly important parameters, such as velocity of the jet. No emission lines are seen from the outflow of jet material, so Doppler shifted cannot be used. Moreover, there is little information on density, internal energy, composition[8] and magnetic field in the jet material.

[8] A matter in hand is the composition of jets: is to be preferred a leptonic or hadronic model for the acceleration of relativistic electrons? The presence of ultra-relativistic hadrons (mostly protons) in the plasma can influence the kinetic energy, while the presence of leptons influences the observed emission. The present model includes both protons and leptons forming the jet plasma.

Moreover, no observations to date have had the angular resolution required to detect and confirm structure on these scales (below 1 mas, Doeleman et al., 2012).

Objects that have jets resembling AGN jets, though on a much smaller scale, can be found in the Milky Way. They are known as microquasars: X-ray binary systems formed by a stellar black hole accreting mass from its companion star.
The first and famous microquasar discovered is SS 433, whose well-observed jet has a velocity of 0.23 c (subliminal relativistic microquasars [9]). It is also the only case among astrophysical jet where baryonic component is directly observed.
However, its most important characteristic is that the jet formation seems to occur when radio intensity increases roughly linearly with X-ray intensity. Then, superluminal knot ejection occurs and after that the jet apparently turns off.
Recently, it has been found a correlation in the radio-loud Seyfert galaxy 3C 120 between the time of the X-ray drops and the knot ejections of bright superluminal knots and between the total energy radiated in a radio flare was related to the equivalent width of the corresponding X-ray drop (Chatterjee et al., 2009). This behavior is strongly suggestive of a disk-jet connection analogous to the that in the galactic microquasars (Beckmann and Shrader, 2012).

1.5.4 Relativistic beaming and superluminal motion

There are many strong arguments in support of bulk relativistic motion in the jets of AGNs (Kharb, 2004):

- the highly variable flux densities of BL Lacs and OVV quasars can be explained by shortened time scales, over and above the time dilation effect, due to relativistic beaming;
- the one-sidedness of kpc-scale jets in the high-luminosity FR 2 and pc-scale jets in the low-luminosity FR1 AGN can be accounted for by Doppler boosting of the approaching jet and Doppler dimming of the receding jet;
- the Laing-Garrington effect (Laing, 1988; Garrington et al., 1988) that is the depolarization asymmetry observed in high-luminosity FR 2 shows that the observed jet is on the same side as the less depolarized lobe, indicating that it is nearer to the observer. It has also been observed, although less strong, for the low-luminosity FR 1 which have slower moving jets on kpc-scale but still have mildly relativistic pc-scale jets;
- the Compton catastrophe (see section "Other processes: inverse Compton and Bremsstrahlung") predicts SIC X-rays is much greater than observed X-ray flux densities telling that the true synchrotron photon density must be lower than what is inferred from assuming isotropy, meaning the emission is beamed.

A consequence of bulk relativistic motion is the intensity enhancement or "Doppler boosting" effect (Rybicki & Lightman, 1979):

$$I_\nu^{obs} = \delta^3 I_\nu$$

[9] It exists also an other kind of microquasars with relativistic superluminal jets, like GRS 1915+105

If the emission is isotropic in the source rest frame, the flux density, F_ν is given as:

$$F_\nu^{obs} = \delta^{3+\alpha} F_\nu$$

where

$$\delta \equiv \frac{1}{\gamma(1-\beta cos\theta)}$$

is the kinematic Doppler factor of a moving source, where $\gamma = (1-\beta^2)^{-1/2}$ is the Lorentz factor and $\beta = v/c$. The Doppler factor has a strong dependence on the viewing angle. The emission is concentrated at angles $\theta \leqslant 1/\gamma$ from the direction of motion. This effect is called "beaming".

An indirect measure of jet speed is provided by the side-to-side brightness ratios for the jet and the counterjet:

$$R_{jet} = (\frac{1+\beta cos\theta}{1-\beta cos\theta})^{2+\alpha}$$

its value can range from a few to several tens in case of strong asymmetry.

Proper motion of bright knots, which are moving away from the active nucleus, is commonly detected using very long baseline interferometry. One of the best studied superluminal radio sources is the blazar 3C 279 (fig. 1.14). The apparent velocities projected on the sky is superluminal, in other words bigger than the speed of light c. This is thought to be the result of a jet, with a speed close to c, at a small angle respect to the observer's line of sight. The apparent superluminal motion is, in fact, a geometric effect (fig. 1.13).
Considering an AGN emitting plasma blob with a velocity v at an angle θ respect to the line of sight at a given time t_1. The observer will measure the event at a time t_1^{obs}. After a time interval τ, at a given time t_2 the blob will have traveled a distance $\Delta x = v\tau$. The observed distance is $\Delta x^{obs} = v\tau sin\theta$. Knowing that the distance between the AGN and the observer is D, the observed time are:

$$t_1^{obs} = t_1 + \frac{D + v\tau cos\theta}{c} \qquad t_2^{obs} = t_2 + \frac{D}{c} \tag{1.4}$$

thus, for the observer the time interval for the blob movement is:

$$\Delta t^{obs} = t_2^{obs} - t_1^{obs} = \tau(1-\beta cos\theta) \tag{1.5}$$

and the observed speed, included in β^{obs}, is:

$$\beta^{obs} = \frac{v^{obs}}{c} = \frac{\Delta x^{obs}}{c\Delta t^{obs}} = \frac{\beta sin\theta}{1-\beta cos\theta} \tag{1.6}$$

Therefore, if the jet is oriented such that, for example, $\theta = 11^\circ$ and β of the jet = 0.999, then the $\beta_{obs} = 10c$.

1.5.5 Ultra high energy cosmic rays

Active galactic nuclei and, in particular, radio galaxies have been proposed as sites that can provide acceleration of charged particles up to ultra high energies that range from $10^{18} eV$ to above $2 \cdot 10^{20} eV$, surely originated outside of the Galaxy. Particles could be accelerated in the

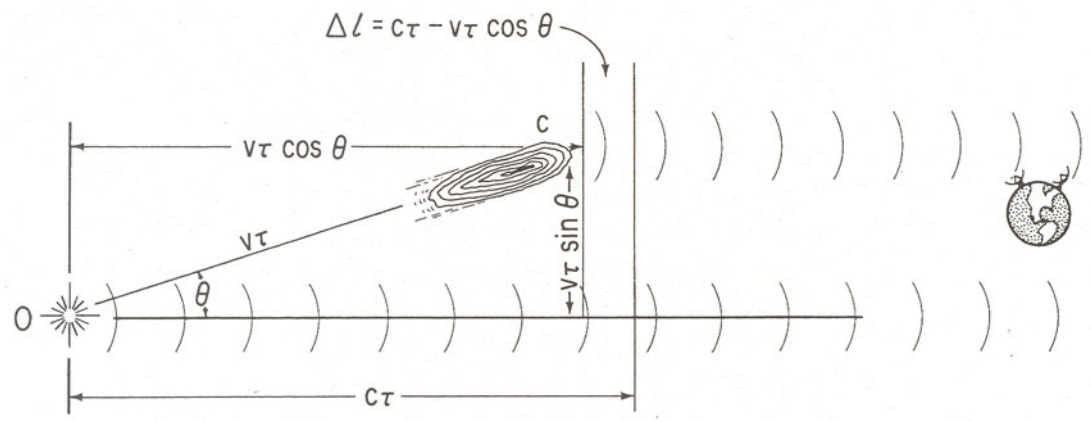

Figure 1.13. *Apparent superluminal motion results when the radiating source is moving so fast that it nearly catches up with its own radiation.*

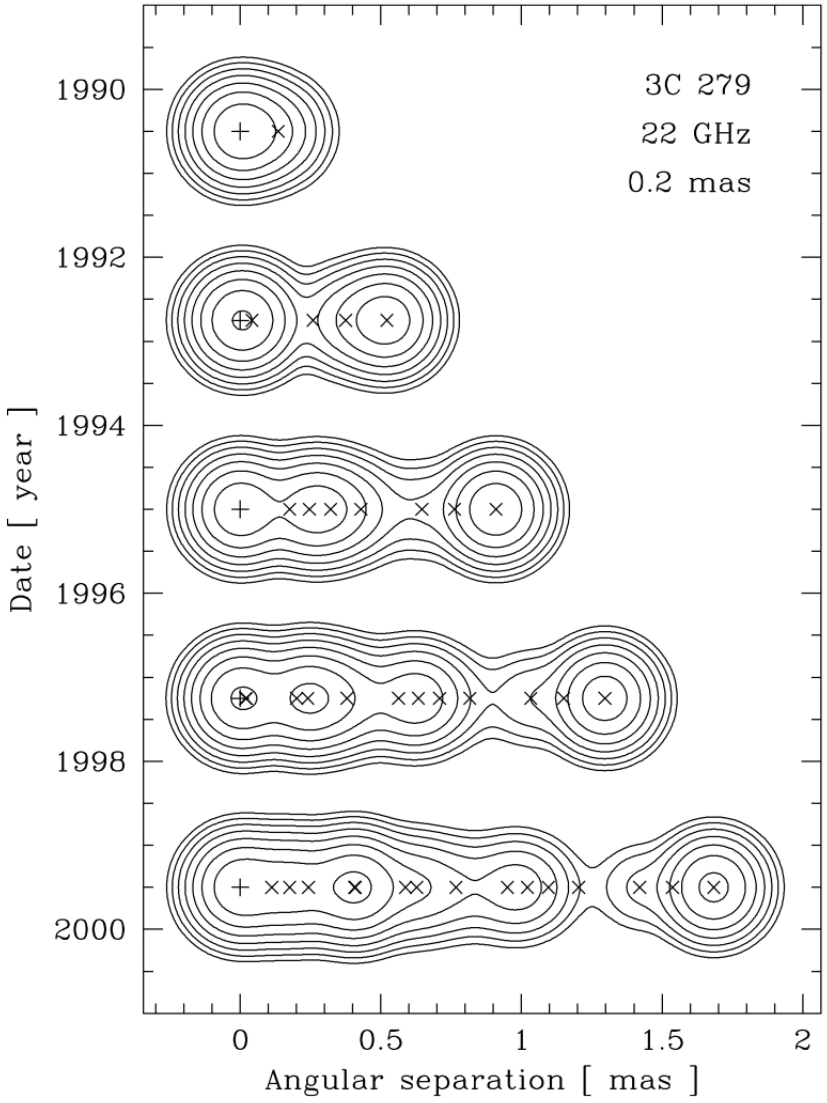

Figure 1.14. *A time sequence of five model VLBI maps of 3C 279 at 22 GHz between 1990 and 2000. The map resolution is 0.2 mas, with a lowest contour at* $50 mJybeam^{-1}$ *and subsequent contours increasing by factors of 2. Each component, marked with X, is assumed to move with a constant apparent velocity of* 5*c with respect to the core of the jet marked with + (Lindfors et al., 2006).*

black hole magnetosphere, in the inner jets, in the radio lobes, in the hotspots and in clusters of galaxies (Kotera & Olinto, 2011).
Ultra high energy cosmic rays (UHECR) acceleration should lead to a unique signature in the gamma-ray spectrum of AGN due for instance to proton synchrotron and photo-hadronic interactions that induce pair cascades. This is still matter of debate and research for many experiments. The Pierre Auger Collaboration in 2007 found a correlation between the arrival directions of cosmic rays ($E > 6 \cdot 10^{19} eV$) and the positions of active galaxies within $\simeq 75$ Mpc. It has been investigated whether regions like radio lobes can accelerate directly UHECR of $\simeq 10^{20} eV$. Centaurus A lobe ($r \simeq 100 kpc$, $B \simeq 1 \mu G$) satisfies the Hillas argument (Hillas,1984), which states that the maximum particle energy that can be accelerated inside a region is:

$$E = Z\, e\, B\, r_L \propto Z\, \frac{B}{10^6 G}\, \frac{r_L}{10^{-2} kpc}\ [eV]$$

where r_L is the Larmor radius of the accelerated particles and Z is the atomic number.
Even Virgo A lobes ($r \simeq 20 kpc$, $B \simeq 10 \mu G$) satisfies this argument, but plasma in the lobes are required to be predominantly relativistic and this is probably not the case of M87, as will be shown later. Moreover, no events were detected in its direction by the Pierre Auger Collaboration, whereas it has been found a small excess in the direction of Centaurus A.

1.6 Cluster of galaxies and the intracluster medium

Cluster of galaxies are the largest gravitationally bound systems in the Universe: they cover linear sizes of some Mpc and are characterized by masses of $\simeq 10^{15} M_{\odot}$, appearing different from field galaxies in their morphological type and color. A general difference in the emission of field radio galaxies and cluster radio galaxies have been first observed by De Young (1972). The former emit almost without interferences from the surrounding environment, while the emission of the latter is strongly disturbed by the interaction with the intracluster medium and with other cluster galaxies. In the local universe, $\simeq$ 90% of the member of core regions of rich clusters consists of ellipticals and lenticular (S0), while spirals dominate in the field (Dressler 1980). This could mean either that galaxies form differently in dense environments or that galaxies are affected by their surroundings.
A cluster contains a number of galaxies between few tens and thousands, an intracluster medium (ICM) that fills the space between galaxies (Forman et al., 1972) and dark matter (DM), whose presence, firstly suggested by Zwicky (1937), is indirectly inferred from optical and X-ray observations.
Overall, galaxies, ICM and DM account respectively for $(3-5)$%, $(15-17)$% and 80% of the total mass of the cluster (Vacca, 2012).
According to the hierarchical model of structure formation, clusters originate from the gravitational merger of smaller groups of galaxies. In these mergers a large fraction of gravitational energy is dissipated in the ICM, generating shock, turbulence and bulk motions, and heating it (Govoni & Feretti, 2004).
Galaxy clusters have been observed in the X band because of the ICM emission and also in the radio band because of the emission of their galaxies and in some cases a wide diffuse synchrotron radio sources which have no obvious connection with the cluster galaxies, but are rather associated with the ICM. This emission requires a population of relativistic electrons with $\simeq$ GeV energies and cluster magnetic fields on μG levels and the sources are called radio halos, relics, or mini-halos according to their morphology and location. These sources show low surface brightness, large size and steep spectrum, thus they are difficult to reveal.
Therefore, an indirect evidence of the existence of cluster magnetic fields comes from the diffuse radio emission and a probe of the existence of a population of relativistic electrons in the ICM can also be obtained from the detection of non-thermal emission.
The intracluster gas is:

- hot with a temperature $\simeq (10^7 - 10^8) K$, which corresponds to an energy $\simeq (1-10) keV$;
- low-density with an electron density $\simeq (10^{-2} - 10^{-3}) cm^{-3}$ in the central regions that decrease to $10^{-4} cm^{-3}$ in the outskirts;
- mainly composed by hydrogen and helium, with traces of heavier elements, kept in an ionized state because of the extremely high temperatures.

In the hypothesis that the ICM is isothermal and in hydrostatic equilibrium, its distribution can be described through a model, called β-model from the parameter that defines the ratio between the specific galaxy and gas kinetic energy:

$$\beta = \frac{\sigma^2 \mu m_p}{kT}$$

where σ is the galaxy velocity dispersion, assumed to be isotropic. The X-ray brightness distribution corresponding to this thermal gas distribution is:

$$S_X(r) = S_0[1 + (\frac{r}{r_c})^2]^{-3\beta+\frac{1}{2}}$$

where S_0 is the central X-ray brightness, r is the distance from the cluster X-ray center and r_c is the cluster core radius that identifies the linear size of the central part of the cluster,. In fact, the intracluster medium is detected through its luminous X-ray emission ($L_X \simeq 10^{43-45} erg\, s^{-1}$), produced by thermal bremsstrahlung process.

At radio wavelengths, the interaction between galaxies and the intracluster thermal gas is responsible of distortion in the morphology of the galaxies.
The interaction between galaxies moving at velocities v_{gal} and ICM with density ρ_{ICM} is driven by a ram pressure $P_{ram} = \rho_{ICM} v_{gal}^2$. The ICM exerts also a static pressure on the lobes equal to $2n_e kT$.
A dramatic example of the interplay between elliptical radio galaxies and intracluster medium is given by the tailed radio galaxies and by the X-ray cavities filled with non-thermal plasma. The observation of an X-ray cavity was firstly made in the Perseus cluster near NGC 1275 (Fabian et al., 1981) and led to an important clue for the interaction between radio galaxies and the surrounding medium. Then, this kind of cavities have been observed in 75% of galaxy clusters with strong cooling core or that need some form of heating at the center (Dunn et al., 2005). They are generated by pressure due to the synchrotron emission of electrons carried by the jets of the AGN inflating the thermal plasma.

Chapter 2

M87

M87 is a giant elliptical galaxy (cD) at a distance of $\simeq$ 16.7 Mpc (1 arcsec = 81 pc; Jordán et al., 2005; Mei et al., 2007) [1]. Note that the cosmology effects can be neglected since the position is within the local region (redshift $z << 1$). This galaxy is near the center of the Virgo cluster [2], which is the rich cluster nearest to the Local Group.
M87 hosts an active galactic nucleus that is harboring one of the most massive black hole among the supermassive ones that feeds a prominent one-sided jet, which is the nearest radio jet in the northern hemisphere. Its viewing angle is $\simeq 10^{\circ} - 19^{\circ}$, constraints put by superluminal motion and Doppler factors (Biretta, Sparks & Macchetto, 1999; Wang & Zhou, 2009).
The jet interaction with the dense intracluster medium forms a complex structure in the kiloparsec scale (10 - 100 kpc) with a projected end-to-end length, the halo diameter, of about 80 kpc (Owen et al., 2000), corresponding to $\simeq$ 16 arcmin. The inner region, known as cocoon, is 5 kpc wide ($1.3x0.5$ arcmin^2) and contains the jet which points towards the north-west.
Known as the radio source Virgo A, M87 is one of the nearest radio galaxies. It is usually classified as a FR 1 galaxy from its radio morphology, since the lobes are brightest closest to the core, but actually it does not fit properly. It does not possess coherent jets that become wider and fainter getting farther from the central source and it is just at the FR 1/FR 2 division, because its luminosity is $L_{178MHz} = 10^{25}\, W/m^2$.
In this sense, it is better to think M87 as a member of amorphous sources characterized by a steep spectrum, typically found in dense cores of galaxy clusters (Owen et al., 2000). A summary of its properties is given in table 2.1.

In M87, a mass of the black hole has been measured of $(3.5\,^{+0.9}_{-0.7}) \cdot 10^9 M_{\odot}$ from gas-dynamical models (Walsh et al., 2013) [3].

[1] The cosmology adopted is the standard ΛCDM cosmology: matter density $\Omega_M h^2 = 0.127^{+0.007}_{-0.013}$ where $h \equiv \frac{H_0}{100} km^{-1}\, s\, Mpc = 0.73 \pm 0.03$ where H_0 is the Hubble constant (Spergel et al., 2006).

[2] To be precise, M87 is in the center of the more massive northern part of the Virgo cluster.

[3] They map out the kinematic structure of the emission-line disk within about 40 pc from the nucleus, including the study of emission-line profiles through the Space Telescope Imaging Spectrograph observations from the Hubble Space Telescope. This accords well with independent calibrations, such as $M_{\bullet} - \sigma$ relation where σ is the bulge stellar velocity dispersion and $M_{\bullet} - bulge\, luminosity$ relation. These are empirical relationships between the mass of the black hole, whose gravitational influence is limited to a very small region at the center of the galaxy, and the large-scale properties of the host galaxy.

Object names	Messier 87
	NGC 4486
Galaxy classification	cD
Associated radio source	Virgo A
	3C274
Equatorial coordinates (J2000)	RA 12h 30m 49.4s
	DEC +12° 23′ 28″
Galactic coordinates	l = 283.7777978
	b = 74.4911308
Redshift	$z = 0.004283 \pm 0.000017$
Distance	16.7 ± 0.6 Mpc (Blakeslee et al., 2009)
Class	FR 1 radio galaxy
Cluster	Virgo cluster (X-ray cluster)
d_{jet}	1.8 kpc

Table 2.1. Basic data for M87, from NED.
cD = subtype of D-type giant elliptical galaxy, also known as supergiant ellipticals or central dominant galaxies, because they are generally found in the central parts of clusters of galaxies, with excess luminosity in their outer parts
J2000 = currently-used standard epoch
RA = Right Ascension, measured in hours, minutes and seconds
DEC = Declination, measured in degrees, arcminutes and arcseconds
l = galactic longitude
b = galactic latitude
d_{jet} = projected length of the brighter jet in kpc (Bridle & Perley, 1980).

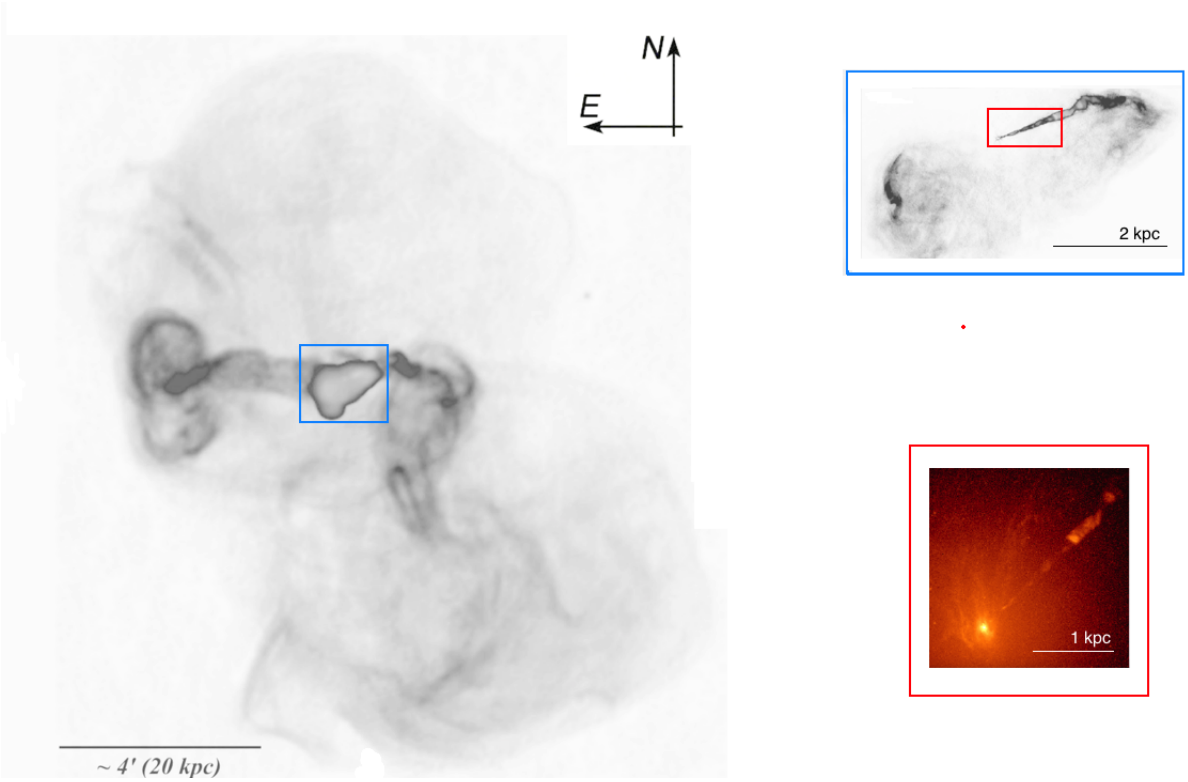

Figure 2.1. *M87 at different scales: on the left, the radio halo of M87 at 90 cm (VLA), on the upper right the inner region at 20 cm (VLA) containing the famous jet and on the bottom right gas disk in nucleus of active galaxy M87 (Optical band 658 nm; instrument: Hubble Space Telescope Wide Field Planetary Camera 2, STScI).*
Note that to see different scales is necessary to observe at different bands. The radio halo is visible only at low radio frequency, whereas the jet is visible at high radio frequency. The optical resolves the jet and the gas disk.

Using the mass measurement, the Schwarzschild radius of the M87 black hole can be estimated:

$$R_{SCH} = (1.038 \pm 0.002) \cdot 10^{15}\, cm = (3.363 \pm 0.006) \cdot 10^{-4}\, pc$$

subtending an angle of $(4.15 \pm 0.15)\mu as$.

The jet and the halo have been intensively observed in the radio on scales from 0.1 pc to 80 kpc. The analysis covers wavelengths between 90 cm and 7 mm with the VLA (Biretta et al., 1995; Owen & Biretta, 1999; Owen et al., 2000) and with VLBI (Reid et al.,1989; Biretta & Junor, 1994; Ly et al., 2004; Dodson et al., 2006). Note that the jet is also a strong optical and X-ray source (fig. 2.2). M87 has been observed in the ultraviolet and optical bands with HST (Biretta et al., 1999; Perlman et al., 2003; Waters & Zepf, 2005) and in the X-ray band with Chandra (Marshall et al., 2002; Forman et al., 2007). It has also been identified with the strong radio source, Virgo A, and is a powerful source of X-rays as it resides near the center of a hot, X-ray emitting cloud that extends over much of the Virgo cluster.

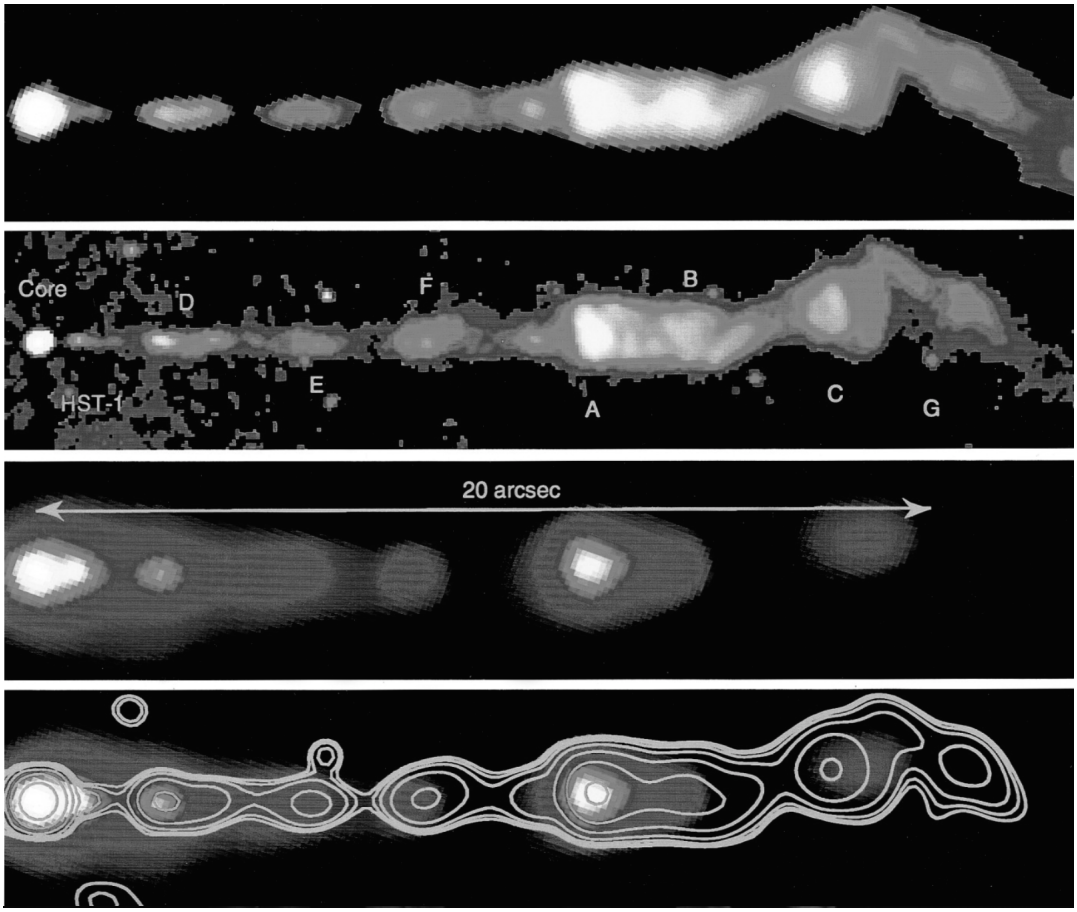

Figure 2.2. *The M87 jet is visible in three different bands and rotated to be horizontal (Marshall et al., 2002).*
First panel: radio image at 14.435 GHz (Instrument: VLA). The spatial resolution is about 0.2 arcsec.
Second panel: optical image (Instrument: HST Planetary Camera; Perlman et al., 2001). The brightest knots are labeled according to the nomenclature used by Perlman et al. (2001) and others.
Third panel: adaptively smoothed image of the X-ray emission from the jet (Instrument: Chandra X-ray observatory). The spatial resolution is about 0.2 arcsec.
Fourth panel: overlay of optical contours over the X-ray image. The X-ray and optical images have been registered to each other to about 0.05 arcsec using the position of the core.
The HST and VLA images are displayed using a logarithmic stretch to bring out faint features, while the X-ray image scaling is linear.
On arcsecond scale, the jet is characterized by many substructures and several knots, the innermost of which is known as HST-1 (at about 1 arcsec from the nucleus).

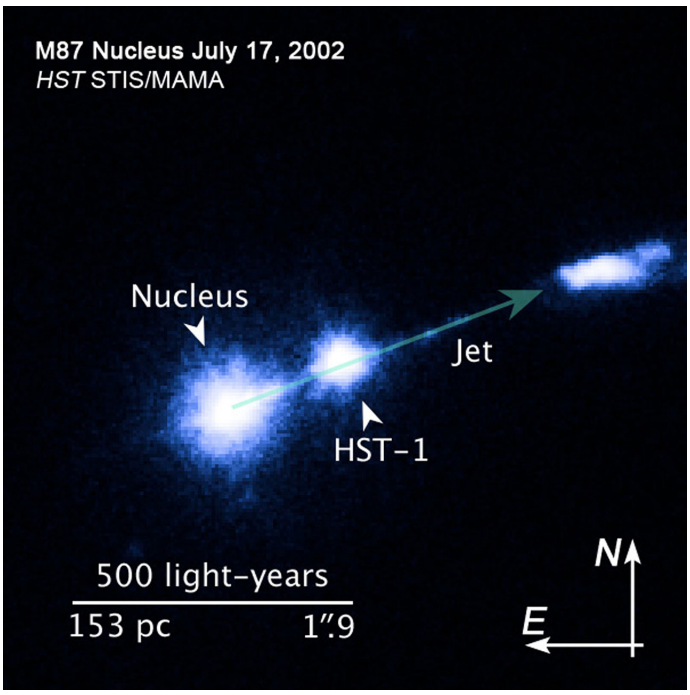

Figure 2.3. *Zooming in M87 jet in optical band. Near the nucleus, it can be seen the bright knot HST-1, first revealed by HST in 1999. It is also active also in the radio and X-ray bands and it might be the site of very high energy emission from M87. HST-1 is oriented in the east-west direction forming an angle of* $\simeq 20^\circ$ *with the jet axis, as detected in e-EVN observations. Its size is in agreement with a jet opening angle of* $\simeq 0^\circ$*, confirming the high collimation of the jet in the sub-arcsec region (Giovannini et al., 2010).*

2.1 Gamma-ray

With the advent of Fermi and Cherenkov telescopes, it has been possible to study M87 in the gamma-ray band from MeV up to TeV energies (Abramowski et al., 2012), therefore M87 is now a well known gamma-ray-emitting AGN.
Very High Energy (VHE, $E > 100$ GeV) emission was first reported by the High Energy Gamma-Ray Astronomy (HEGRA) collaboration (Aharonian et al., 2003), followed by the HESS collaboration that also revealed gamma-ray flux variability on timescales of two days (Aharonian et al., 2009). M87 often shows strong flaring events at TeV energies with rapid variability timescales ($\simeq$ few days), but constraining the site of this very high energy emission continues to be a subject of discussion. According to the short timescales that imply a compact emitting volume, the inner jet region is favored. Therefore, the two most promising gamma-ray production sites are the nucleus of M87 itself or the bright knot at $\simeq 1$ arcsec from the core, known as HST-1 (fig. 2.3). The TeV flare occurred in 2005 was accompanied by radio-to-X-ray flares from HST-1, whereas, in contrast, the one occurred in 2008 was accompanied by a strong enhancement of the radio and X-ray core emission while HST-1 did not give any sign of activity. The latter was in a low state also during the 2010 TeV flare (Hada, 2013). These conditions led to the conclusion that the TeV flares are likely to originate in the core region.

VHE radiation was detected also by VERITAS (Acciari et al., 2010) and in addition radiation above 100 MeV was revealed by Fermi/LAT observations (Abdo et al., 2009).

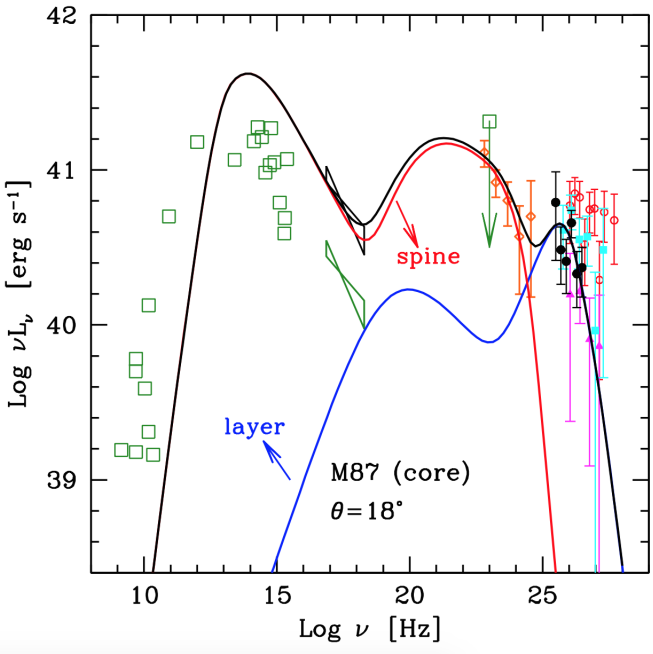

Figure 2.4. *Spectral energy distribution of the core of M87 (green open squares) together with the MAGIC data points (black filled circles), from Aleksic et al. (2012).*
For comparison the H.E.S.S. spectra taken in 2004 (magenta trangles) and 2005 (red open circles) and the VERITAS spectrum taken in 2007 (cyan filled squares). The green bow-tie and black bow-tie reports respectively the X-ray spectrum measured by Chandra in 2000 and the the X-ray emission of the period (2005 – 2007) assuming the same slope and a higher normalization. In the high-energy gamma-ray range the green open square corresponds to the EGRET upper limit and the orange diamonds to the Fermi-LAT energy spectrum. The lines report the emission from the spine (red) and from the layer (blue) and their sum (black).

The Major Atmospheric Gamma-Ray Imaging Cherenkov (MAGIC) collaboration started to observe M87 regularly in 2005 and several campaigns have followed until 2012 (e.g. Mariotti et al., 2010). The SED of the core of M87 in figure 2.4 summarizes the results. It shows two pronounced bumps, one peaking in the IR band that is the synchrotron peak and one extending from MeV to TeV energies that is the synchrotron inverse Compton peak (see "Other processes: inverse Compton and bremsstrahlung").

2.2 X-ray

At the center of a galaxy cluster the dense gas emits at X-ray wavelengths, cooling quickly in absence of a heat source. However, an AGN can provide an amount of energy, hence heating and turbulence, enough to offset the gas cooling. The energetic particles produced in the vicinity of the black hole rise through the X-ray emitting atmosphere of the cluster, lifting up the coolest gas near the center of M87. In fact, when a jet plows into the surrounding gas, a buoyant, magnetized bubble of high-energy particles is created and then rise like hot air from a fire or explosion in the atmosphere. Its signature is a bright region in radio images and dark cavity in X-ray images, surrounded by a bright X-ray arc, as it is possible to see in fig. 2.5, obtained by NASA's Chandra X-ray Observatory, a space telescope sensitive to X-ray

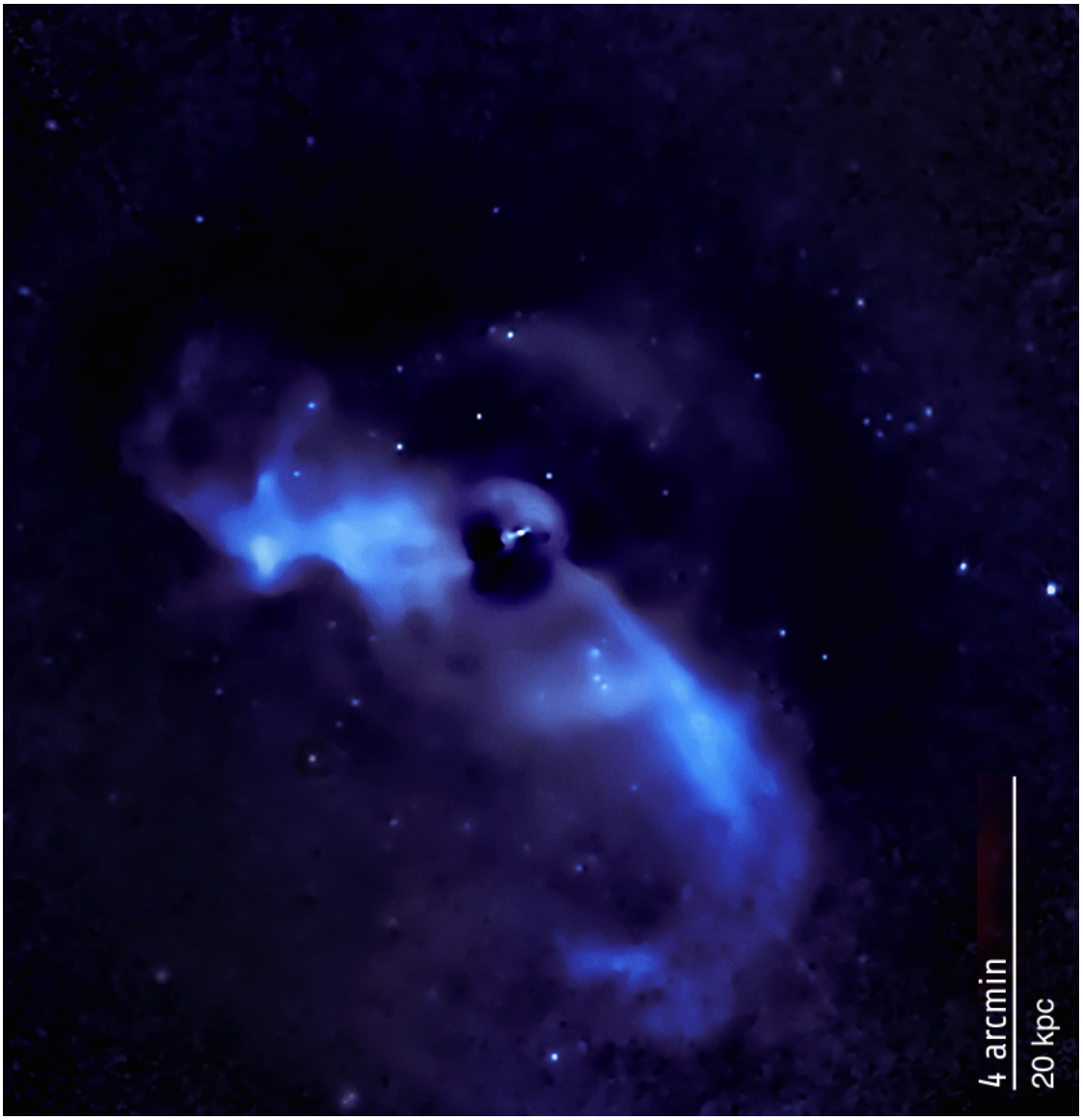

Figure 2.5. *M87 in a soft X-ray image (0.5 - 1 keV). The image shows the very prominent eastern and southwestern arms. The long southwestern arm appears to be composed of several filaments with widths of* $\simeq$ 300 *pc, whereas the eastern arm can be interpreted as a series of bubbles at different evolutionary stages as they rise in the circumgalactic medium. The filamentary structures are very soft and are not apparent at energies above 2 keV. The jet is inside the central region. Instrument: Chandra X-ray observatory (Credit: NASA/CXC/KIPAC/N. Forman et al., 2007).*

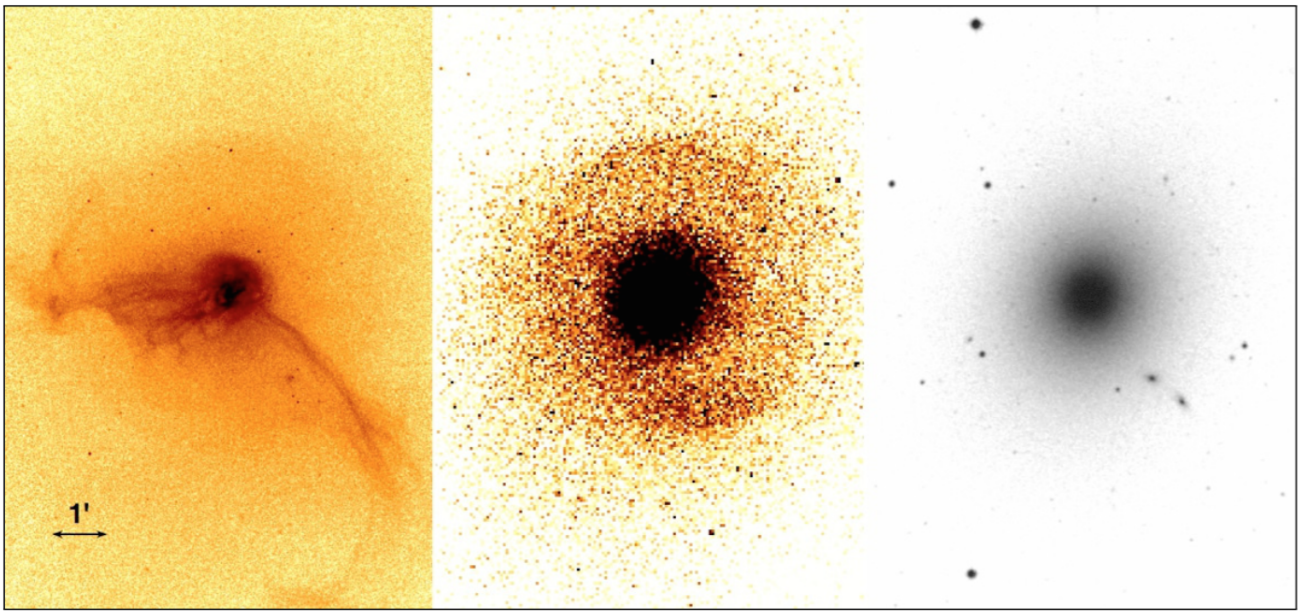

Figure 2.6. *A comparison of M87 in different X-ray bands and optical band.*
On the left, soft X-ray image that shows filaments and bubbles border (0.5-1.0 keV energy band, instrument: Chandra X-ray observatory) . At the center, hard X-ray image shows a ring of emission showing spherical shocks. It is a nearly circular ring of outer radius 2.8′ (13 kpc) which is signature of a weak shock, driven by an outburst from the SMBH (3.5-7.5 keV energy band, instrument: Chandra X-ray observatory). On the right, optical image that shows the stellar component. (Forman et al., 2007)

emission (Churazov et al., 2001). The gas in the inner 20 kpc show a complex structure: a very asymmetric distribution and the same extension as the radio halo, which consists of plumes of fast-moving gas from the jets rising into the hot intra-cluster medium (Ghizzardi et al., 2004). The halo was first detected with the Einstein Observatory (Fabricant et al., 1980) and then in 1987 two X-ray bright arms presumably driven by the AGN activity were discovered by Feigelson et al., who also noted an asymmetry in the emission and a correlation between X-ray and radio emissions confirmed later by Böringer et al. (1995). In fact, the arms of cool gas extend to the east and south-west of M87 as the radio emission does in the outflow structure. As previously said, they are likely to be the result of cooling gas uplift in the wakes of cosmic rays buoyant bubbles created by previous outbursts, as Churazov (2001) first hypothesized. Later, Chandra, ROSAT and XMM-Newton observations added more details (Forman et al., 2005; Forman et al., 2007). Chandra X-ray observations provide two major results:

- filamentary structures of width $\simeq$ 300 pc are seen in the eastern and southwestern arms in the soft X-ray band (0.5 - 1.0 keV); filaments can derive from buoyant bubbles at different heights in the atmosphere and different stages of evolution;
- a ring of hard emission (3.5 - 7.5 keV) that is nearly circular with an outer radius ranging from (11.6 - 13.3) kpc; it is a signature of a weak shock.

It was observed a thermal spectrum for the excess emission, which is cooler than the ambient gas that is at $\geqslant$ 2 keV (Böhringer et al., 1995). Chandra X-ray images confirmed the hypothesis that the mechanism causing the buoyant bubbles rise is the injection into the inner halo by the relativistic jet of high-energy particles through the cooling gas, excluding the first hyphotesis of X-ray emission trough IC scattering of CMB photons by the same relativistic electrons responsible for the synchrotron emission. In fact, within a distance of $\simeq$ 20 kpc from the galaxy's center, a series of unevenly spaced loops are visible in the hot gas.

X-ray features similar to those seen in M87 have been observed in other cD galaxies in the centers of galaxy clusters, like Perseus A. This suggests that episodic outbursts from supermassive black holes in giant galaxies may be common phenomena that determine how fast giant galaxies and their central black holes grow. As gas in the galaxy cools, it would flow inward to feed the black hole, producing an outburst which shuts down the inflow for a few million years, at which point the cycle would begin again (Feng et al., 2004; Forman et al., 2007).

The X-ray image reveals also the inner region with the bright galactic nucleus and an irregular, knotty structure of the jet similar to that detected in the radio and optical band (bottom image in fig. 2.2). However, the knots near the core are much brighter in X-rays than the farthest knots, relative to the optical and radio bands (Marshall, 2002). The exact reason for this dimming is unknown, but it is likely to be related to the slowing of the jet, which was discovered using HST.
Inside the jet, high-energy electrons radiate by synchrotron, creating the observed non-thermal radio, optical and X-ray emission from knots.
The spectrum and intensity of the X-rays from the galactic nucleus also indicate that this

radiation is not caused by hot gas produced by material falling into the supermassive black hole. An hypothesis is a high-energy outflow close to the black hole producing the X-rays by the same synchrotron process that explains the knots in the jet observed by Chandra. A particular feature is an X-ray enhancement near the brightest knot in optical and radio, suggesting a strong interaction between the jet and the X-ray gas in the core of the Virgo cluster.

2.3 Ultraviolet

The Ultraviolet Imaging Telescope (UIT) observations of M87 resolve the jet that is much brighter than the galaxy in this band (Greason et al., 1991).
Hubble Space Telescope was used to UV photometry of the jet of M87 (Waters & Zepf, 2005). These observations are essential for constraining the synchrotron emission and the break frequencies between the optical and X-ray band.

2.4 Optical

The Faint Object Camera on the Hubble Space Telescope revealed considerable detail in the optical jet (Boksenberg et al. 1992).
Hubble Space Telescope spectroscopy has given strong evidence for a rapidly rotating ionized gas disk at its center of M87 nucleus, from which the presence of a central supermassive black hole is inferred (Macchetto et al., 1997).
The optical spectrum is a featureless continuum that follows a power law and is highly polarized. Moreover, HST observations has been used to measure proper motion of the jet knots revealing superluminal motion (Biretta et al., 1999; Meyer et al., 2013).
Bright knots exhibit flatter spectra than inter-knot regions with maximum flatness in the two inner jet knots (D-East and HST -1), which contain the fastest superluminal components (Perlman et al., 2001).

2.5 Infrared

Ground-based observations of M87 in the mid-IR band revealed emission produced by synchrotron from the nucleus and the brightest knots of the jet (Perlman et al., 2001). The Infrared Space Observatory (ISO) and the Infrared Astronomical Satellite (IRAS) observed an excess in the far-IR emission above the synchrotron interpolation from the radio (Haas et al., 2004). Then, images from 3.6 to 160 μm obtained with Spitzer Space Telescope showed the same excess from radio to the non-thermal features in the mid-IR and optical.
A controversial issue is the origin of the FIR emission in M87, i.e., the question of whether the FIR emission is caused entirely by synchrotron emission or whether there is an additional contribution from dust associated with either the global interstellar medium or a nuclear dust component. This has been interpreted by Shi et al. (2007) as an effect of warm dust distributed

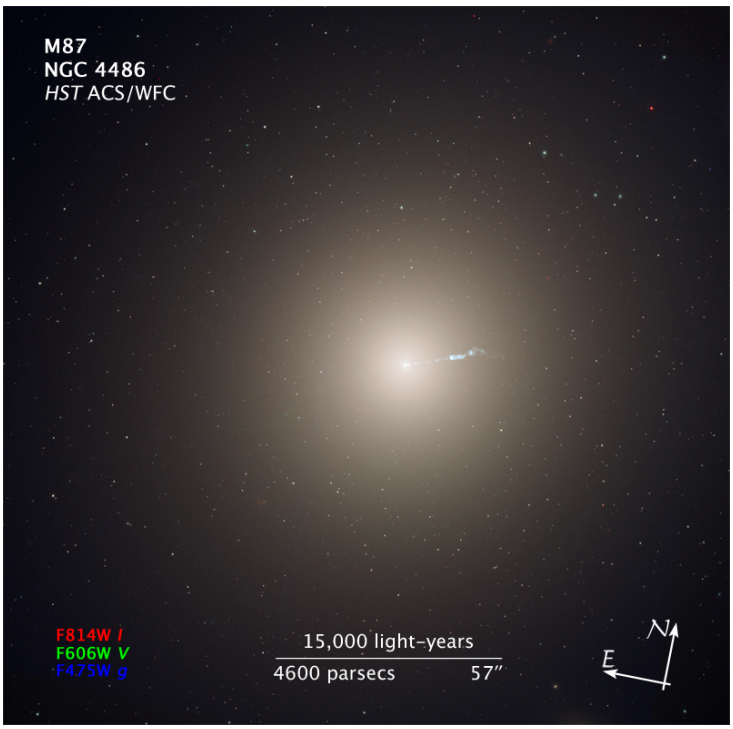

Figure 2.7. *Optical image of M87 taken with Hubble Space Telescope. The image is a composite of individual filtered data that cover the visible and infrared portions of the spectrum.*

throughout the galaxy with a far-IR luminosity typical of normal giant elliptical galaxies. In contrast, Base et al. (2010) found that synchrotron emission is an adequate explanation of the FIR emission with no reason to invoke the presence of smooth dust emission associated with the galaxy interstellar medium, as advocated by Shi et al. (2007). Seen from the FIR point of view, M87 is a passive object with a central radio source emitting synchrotron emission, without a substantial diffuse dust component (Base et al., 2010).

2.6 Radio

The total radio power of the source is $5.37 \cdot 10^{34} h^{-2}\, W$ for the emitted frequency range (10 MHz- 150 GHz) (Herbig & Readhead, 1992) [4].

Radio images of M87 at different scales show different areas of the source: it is possible to see the entire structure at a wavelength of 90 cm and above, while the jet structure is seen at 20 cm down to centimeter wavelengths, as it will be shown in the following images.

The inner region is visible at 20 cm: here, the radio emission is powered by the jets from the central black hole inflating giant, bubble-like structures. Decreasing the wavelength, it is possible to zoom in the jet zone, detecting the region close to the core where the jet is formed into a narrow beam.

In the formation region, that is a few tenths of parsec of the galaxy's core, the jet is seen opening widely, at an angle of about 60° nearest the black hole, but is squeezed down to only

[4]The bolometric luminosity is calculated at standard rest frequencies $P_{bol,emit} = 4\pi(R_0 r)^2(1+z)^2 F_{bol,obs} h^{-2}$ where $H_0 = 100h\, kms^{-1} Mpc^{-1}$ and $R_0 r$ is the coming distance to the source.

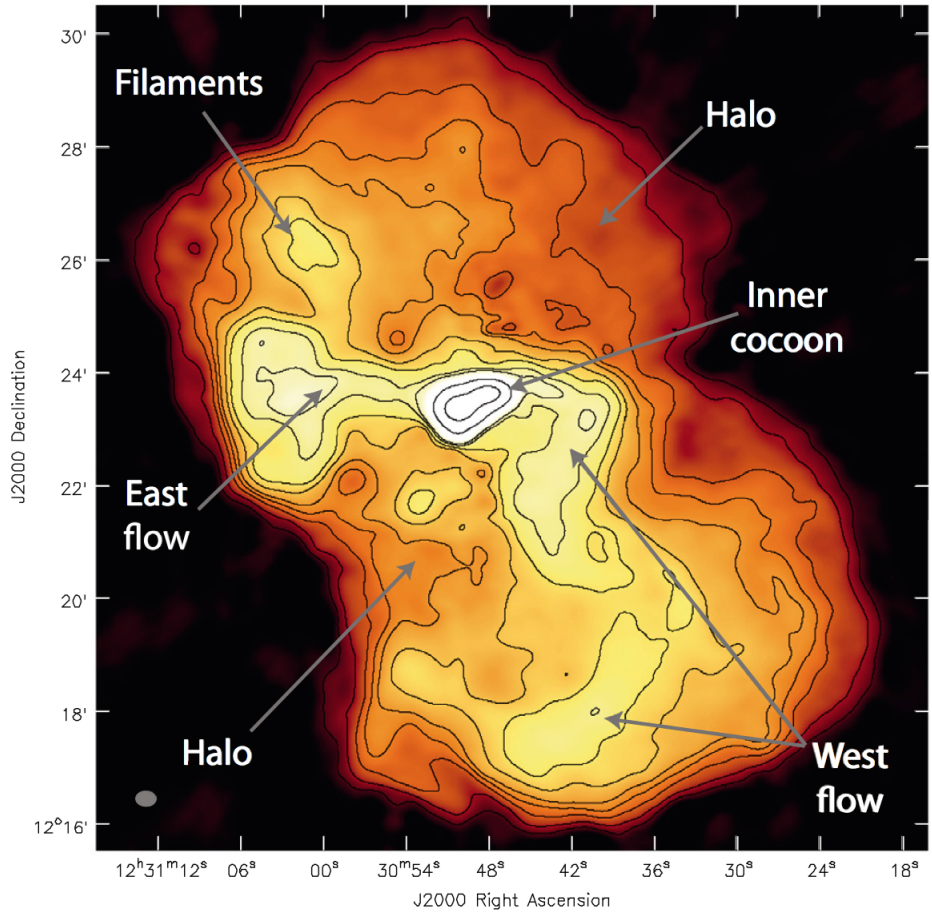

Figure 2.8. *The image of Virgo A at* $\simeq$ 2 *m (140 MHz). The image obtained at low radio frequency with LOFAR confirms the structure as obtained by Owen, with a clear distinction and analysis of the different regions. The central region containing the jet and inner radio lobes is in the inner cocoon (de Gasperin et al., 2012).*

6° a few parsecs away (Junor, Biretta & Livio, 1999).

In the large-scale images obtained at 2 m ($\simeq 140 MHz$; fig. 2.8, De Gasperin et al., 2012) and at 90 cm ($\simeq 327\,MHz$; fig. 2.9, Urvashi, 2010), some features of the overall structure can be distinguished:

- the inner region, frequently called the inner cocoon, is made by the galactic nucleus, the jet and the inner radio lobes and is contained in the white patch at the center of the figure 2.8, extending about 2 kpc from the core,with a sharp surface brightness drop between this region and the east and west outflows. The north-west pointing jet and the inner structure are not resolvable at this frequency;
- from the inner region toward east and north of west, there are two flows that connect the inner and the outer haloes; note that the westward flow is initially aligned with the inner jet but it quickly bends and twists toward south, while the eastward flow is straightforward until it ends in defined and bright circular lobes. An open question is why the east and west regions are different, this could be due to differences in the flows or in the environment;

- all these regions are immersed in a large structure of two buoyant bubbles made by inhomogeneous plasma; the bright and curved flows gradually disperse and form thinner structures, forming the so-called filaments characterized by an enhancement of radio emission and probably by strong magnetic fields. Each bubble extends $\simeq$ 40 kpc from the central source and ends abruptly with well-defined outer edges; in fact, the source appears well confined by the high pressure of the intra-cluster medium.

2.6.1 The radio halo

The interaction of the jet with the dense external medium forms the large-scale radio halo, which covers an area far larger than the optical galaxy. The outward flow from the active nucleus continues beyond the kiloparsec scale jet. The full extent of the radio source is about 80 kpc end-to-end with a well-defined outer edge. The size of the radio halo is the same at all observed frequencies from 25 MHz (LOFAR; de Gasperin et al., 2012), 74 MHz (VLA; Kassim et al., 1993), 140 MHz (LOFAR; de Gasperin et al., 2012), 327 MHz (VLA; Owen et al., 2000) to 10.6 GHz (Effelsberg; Rottmann et al., 1996). The radio-emitting plasma appears well confined by the high pressure of the ICM. For this characteristic of the halo, it is possible to exclude single-particle diffusion in the cluster gas as a mechanism of its formation, because the size would depend on frequency due to synchrotron aging.
The large-scale structure is made by two extended bubbles, inflated by the inner flow and overlapping in the central region due to projection effects. The gas emits by synchrotron while it is expanding outward, due to the energy input from the core transported by poorly collimated outflows. Therefore, these latter are the connection between the inner jet and the full scale of the halo.

The halo is complex as shown by the bright plumes emanating from the inner lobes and the large-scale structure, being supplied with energy by the relativistic radio jet. Although the jet does not remain well confined and directed, its mass and energy continue to flow into plumes, causing the halo pressure to rise. Therefore, the halo is not static and its radio-loud plasma slowly expands outward into the surrounding ICM with a well-defined edge between them. The jet is pumping at least at much energy into the local atmosphere, as is being lost by the cluster's atmosphere to X-rays. Therefore, the black hole in the galactic nucleus is currently supplying a power to the radio halo that is at least as large as the radiative losses from the core. The outflow of energy is dominating the slow, cooling-driven inflow of the hot cluster gas. Note that the activity is likely to be a transient phase, as often happens in radiogalaxies, and M87 may have been gone through various phases of on-off cycles of the central engine.
In conclusion, the fact that plasma emission is confined within the same boundaries down to 25 MHz, fresh energetic particles are continuously flowing from the central cocoon and part of the halo edges are limb brightened led to abandon the idea that this halo was a relic of a previous activity or outburst in favor of the picture of an active halo (Owen et al. 2000, de Gasperin et al. 2012).

To model the observations, it is necessary to know whether the halo region is dominated by thermal or relativistic particles. In the first case, synchrotron emitting regions contain a sig-

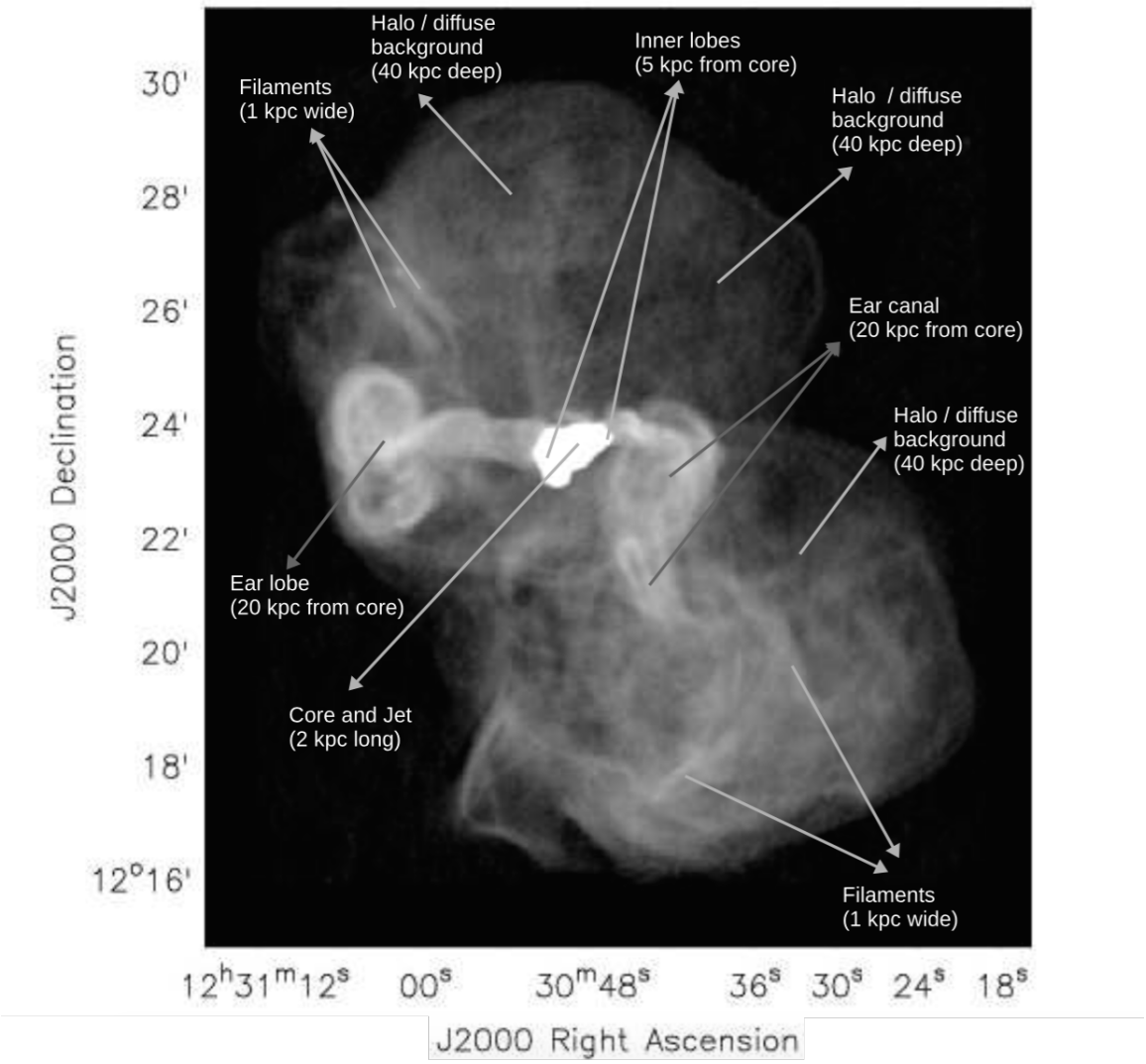

Figure 2.9. *The VLA image of M87 at* $\simeq$ 90 *cm (327 MHz) with labels. It shows a bright central region with a 2 kpc radio jet and 5 kpc inner radio lobes, a pair of* $\simeq$ 20 *kpc flows to the east and west of the inner region and two* $\simeq$ 40 *kpc fainter, larger bubbles to the north and south overlapping in the central region due to projection effect.*
The eastward-flow proceeds straight in a sort of cylinder and ends in a lobe, frequently called ear, whereas the westward flow, initially aligned with the jet, quickly twists towards south. Both flows come from the inner region and reach the halo edge, where they disperse (especially the westward one).
Narrow extended filamentary structure is seen throughout the ear lobe/canal structures and the halo, with low-level diffuse background emission in between (Urvashi, 2010).

nificant amount of thermal gas and are close to the minimum-pressure condition, whereas in the second case they are far from it and Virgo A is primarily a relativistic bubble and thermal material inside it must come from leakage through the boundary over the period of expansion.
The minimum-pressure analysis suggests that the region is thermally dominated (Owen at al., 2000). A significant mass of thermal gas is required in the region to maintain pressure balance with the unheated external gas in the X-ray atmosphere. In this model, the jet is depositing its matter and energy on scales of tens of kiloparsecs from the core in the form of turbulence and heat.

Considering the halo as a spherical bubble of radius R containing hot plasma undergoing steady energy input from the jet, energy conservation describes the expansion of the halo due to its own internal energy as follows:

$$\frac{dU_{int}}{dt} = P_j - p\frac{dV}{dt} - L_{rad} \tag{2.1}$$

where U_{int}, p, V are respectively the internal energy, pressure, volume of the halo plasma, P_j is the time-independent jet power and L_{rad} are the radiative losses from the halo (Eilek & Shore, 1989).
Assuming a slow expansion where the interior pressure remains comparable to the exterior pressure and assuming radiative losses neglectable respect to the jet power and $\frac{dU_{int}}{dt} = -L_{rad}$, the equation becomes:

$$4\pi R^2 p_x(R)\frac{dR}{dt} = \frac{\Gamma - 1}{\Gamma}P_j \tag{2.2}$$

where Γ is the plasma adiabatic index, which can assume the value $5/3$ in case of non-relativistic plasma (most of the content of the bubbles is thermal) or $4/3$ in case of relativistic plasma (bubbles dominated by relativistic particles and magnetic fields).

Owen et al. (2000) estimated [5] the current expansion rate of the outer edge $\frac{dR}{dt}$: $\simeq 100 P_{44} km\, s^{-1}$ if $\Gamma \simeq 4/3$, whereas $\simeq 160 P_{44} km\, s^{-1}$ if $\Gamma \simeq 5/3$. Note that the sound speed in the external gas is $c_s \simeq 400 km\, s^{-1}$, so that the expansion is subsonic.
Moreover, they estimated also the current age of the radio halo t: $\simeq 150(P_j/10^{44})^{-1} Myr$ if $\Gamma \simeq 4/3$, whereas $\simeq 96(P_j/10^{44})^{-1} Myr$ if $\Gamma \simeq 5/3$. It can be concluded that the halo is younger than the host galaxy.
On the other hand, De Gasperin et al. (2012) estimated the halo age using a continous injection model that gives a cut-off frequency value from which t can be found: $t \simeq 40 Myr$.
Finally, Churazov et al. (2001) hydrodynamics simulations gave the result that the halo edges can be reached by the buoyant bubbles in $42 - 67 Myr$.

The discrepancy in the halo age estimation can be explained with different situations:

- the magnetic fields in the different part of the bubbles may be stronger or weaker, influencing differently the electron lifetimes; in fact, electrons in a weak magnetic field can survive longer; this could also explain the observed filamentary structure;

[5] using $P_j \simeq 10^{44} erg\, s^{-1}$ and $R \simeq 35 kpc$

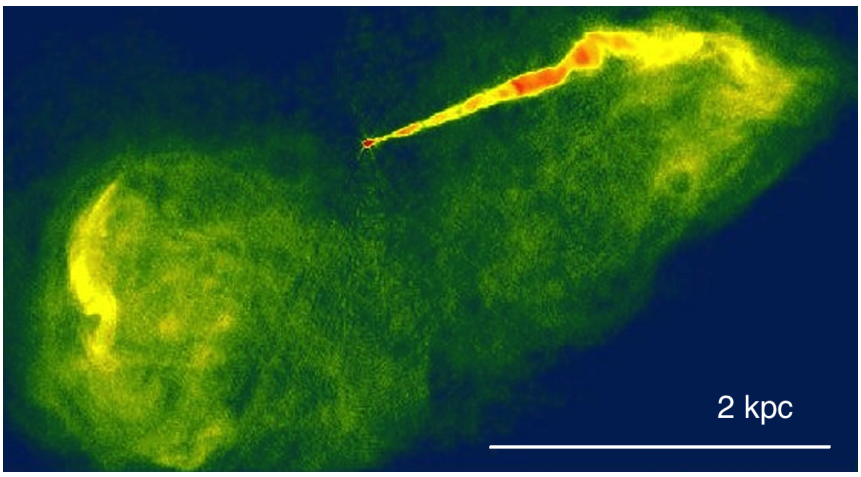

Figure 2.10. *The inner halo at 20 cm, from Owen (VLA). The scale from the bright core (at the left) to the outermost bright spot (where the flow starts to bend) is about 2 kpc.*

- the phenomena of electron re-accelaration;
- the presence of new plasma re-filling zones of aged plasma.

2.6.2 The inner halo

The inner halo or cocoon is a small, radio-loud region formed by lobes with an end-to-end extension of about 5 kpc (figure 2.10).
It is not yet clear how the flow connects from these inner lobes to the outer halo. What is observed is that approaching the outer halo there is a strong surface brightness drop.
In old models of M87 (Reynolds et al., 1996), this region was assumed to be the only active region of the source, trapping all of the energy coming from the inner part. In recent works (Owen et al., 2000; de Gasperin et al., 2012), it is thought to be a high-pressure structure that let most of the jet power go through it or a recent and short transient structure compared to the outer halo.

A continuous injection of relativistic electrons provides a scenario in which the lobes are still supplied by fresh relativistic particles from the active nucleus.

2.6.3 The jet

The non-thermal jet in M87 connects the innermost galactic nucleus to the outer parts of the source, supplying the surrounding region with energy and relativistic plasma.
It retains a self-similar structure as zooming in from the largest scale of a few kiloparsec to the smallest scale yet observed, that is about a parsec. Obviously, this similarity must break down approaching the nucleus. The physical scale of the innermost jet features, next to the unresolved core source, is about 0.1 pc, corresponding to $300R_{SCH}$.

As previously shown in fig.2.2, the one-sided jet is pointing towards north-west and it is detected in radio, optical, UV and X-ray bands, where the emission is primarily confined to knots along the jet. In 1999 the Hubble Space Telescope revealed a bright knot at $\simeq$ 1 arcsec

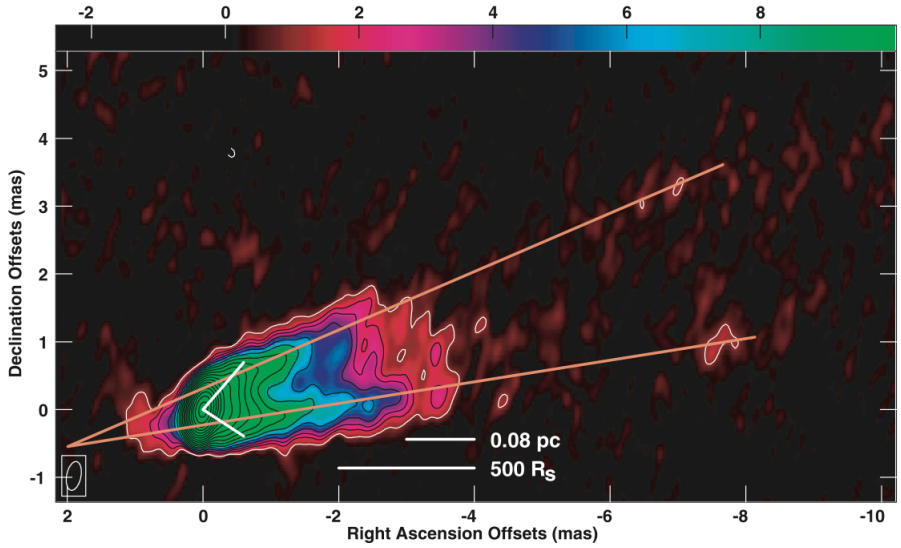

Figure 2.11. *Averaged image from 43 GHz observations. The orange lines follow the edge-brightened jet emission from 10 mas west of the core, with an opening angle of* 15°*, while the white lines represent the wide opening angle (Ly, Walker & Junor, 2007). Later studies demonstrated that the black hole is in the vicinity of the area identified by the white lines and not at red triangle vertex, giving a clue for the presence of a counter jet (Hada et al., 2012).*

from the core, then called HST-1 (see section "Gamma-ray").
A particularity of M87 is that its jet remain directed for only a few kiloparsecs from the galactic core and then it disrupt, while in most radio galaxies the jets can remain collimated until about 100 kpc. Moreover, the counter jet is not visible due to the effect of relativistic beaming, in this case de-boosting, but its presence can be inferred by its influence in the emission in the east part of the inner region. In fact, it will be important in constraining the geometry of the jet, because the flows seen in the halo suggests that a counter jet exists but is very faint. It has been observed with VLBA and Global VLBI observations at 22 GHz, 43 GHz (fig. 2.11; Ly, Walker & Junor, 2007) and 86 GHz 86 GHz (Krichbaum, 2006).
The jet orientation has been studied through years. First, it was estimated to be 10° and 45° from our line of sight (Biretta, Sparks & Macchetto, 1999; Ly, Walker & Junor, 2007) and then within the likely range of 15 ° to 25 ° (Acciari et al., 2009).

2.6.4 The galactic nucleus

The supermassive black hole in the galactic nucleus supplies a flux in energy $P_j \geqslant 10^{44} erg\, s^{-1}$ to the radio halo (Owen et al., 2000). Only a small fraction goes for radio emission and the bulk must be deposited in kinetic or internal energy of the plasma in the Virgo core to allow turbulence, bulk flows and heating. The input to the region from the nucleus exceeds radiative losses at the present epoch.

Because the jet is bright, the black hole is very massive, and M87 is relatively nearby, M87 is an ideal target to study the initial jet-formation process and to attempt imaging of the region close to the black hole.

To analyze the jet launching structure the Event Horizon Telescope, a telescope array [6] based on the VLBI techniques, has been set up. It has an angular resolution that allows to resolve the inner accretion disks of nearby AGN and that is comparable to the event horizon operating at 1.3 mm, where AGN start to become optically thin (Doeleman et al., 2012).
In M87, taking the 1.3 mm VLBI size as the innermost stable circular orbit (ISCO) diameter[7] it has been estimated the black hole spin, that is $a > 0.2$, and the sense of the accretion flow, that is prograde orbit (Doeleman et al., 2012). In fact, retrograde orbits would be larger than the core size derived. This result is consistent with generally accepted theories that the spin axes of the accretion disk and black hole will be brought into alignment through gradual angular momentum transfer from the orbiting disk (Gammie, Shapiro and Mc Kinney, 2004).

2.7 Superluminal motion

Proper motion measurement with high angular resolution is a useful tool for the kinematics of relativistic jets.
VLBI initially demonstrated that the speeds of knots in M87 are subluminal (Biretta, Owen & Cornwell, 1989).
In contrast, HST observations revealed superluminal motion in the region HST-1 near the core with a range of $(4-6)c$. Moreover, new observations through EVN (Asada et al., 2014) show a gradual acceleration of the bulk flow from sub to superluminal regimes, that is from $(0.67 \pm 0.63)c$ to $(3.74 \pm 1.18)c$. This is in agreement with the evidence of gradual collimation up to $5 \cdot 10^5 R_S$ from the central source.
Therefore, it can be established that superluminal motion has been detected in both radio and optical in M87 jet.

In fig. **??** the distance from the core of the knot HST-1 from e-EVN and VLA data is shown: before 2003, HST-1 is very faint but then becomes evident and well separated by the jet structure near the core. There is an evident change in the proper motion velocity during the epoch 2005, coincident with the TeV gamma-ray activity and the maximum radio and X-ray flux density of HST-1.
Before July 2005, the apparent velocity is $(0.5-0.6)c$ and then until April 2010 becomes $\simeq 2.7c$. Assuming a jet orientation angle equal to 25°, a proper motion equal to $\simeq 2.7c$ corresponds to an intrinsic velocity equal to 0.94 c (Giovannini et al., 2010). It is not yet clear if this is related to the M87 VHE activity and/or to the maximum radio and X-ray flux density of HST-1 at this epoch (Hada et al., 2014).

[6] The EHT array consists of four telescopes at three geographical locations: the James Clerk Maxwell Telescope (JCMT, partnered with the Submillimeter Array (SMA)) on Mauna Kea in Hawaii, the Arizona Radio Observatory's Submillimeter Telescope (SMT) in Arizona, and two telescopes of the Combined Array for Research in Millimeter-wave Astronomy (CARMA, located $\simeq$ 60 m apart) in California.

[7] Recalling that ISCO is the critical size scale within which matter quickly plunges to the event horizon. The ISCO diameter also marks the peak density and rotational speed of the accretion flow and it is related to the the black hole spin.

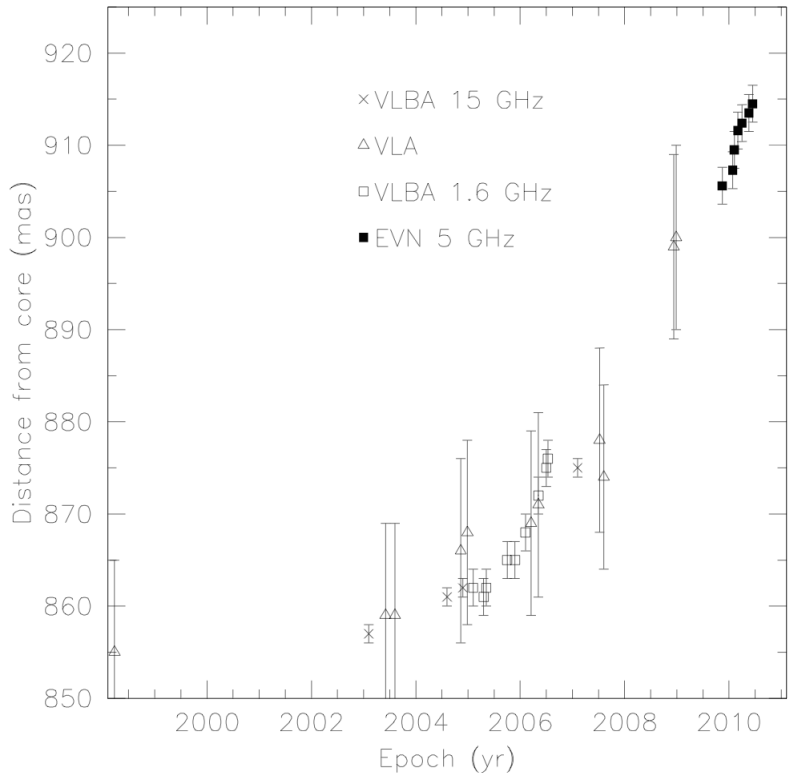

Figure 2.12. *Distance of HST-1 brightest peak from the M87 core at different epochs. (Giovannini et al.., 2010).*

2.8 The Virgo cluster

Virgo is the nearest rich galaxy cluster. Binggeli et al. (1985) have cataloged 2096 galaxies (Virgo Cluster Catalog) in $\simeq 140\,deg^2$ area centered $\simeq 1\,deg$ northwest of M87, whose $\simeq 1300$ galaxies have been identified as members based on their measured radial velocities. It is very irregular, making the mass distribution modelling difficult. The inner region of the cluster, traced by the atmosphere of hot, X-ray loud gas, is typical of galaxy cluster cores. At less than 40 kpc, there is a mixture of relativistic particles, thermal plasma and magnetic fields in a complex, turbulent and magnetized region. X-ray observations reveal the hot, diffuse gas that fills the cluster and show that a large part of the cluster mass is centered on M87, with smaller concentrations around M86 and M49 (ROSAT observatory, Böhringer et al., 1994). Assuming hydrostatic equilibrium, the hot X-ray gas directly traces the gravitational potential that is the dark mass of the system in which it is embedded:

$$\frac{dP}{dr} = -G\frac{M(r)n_{gas}(r)}{r^2}$$

where $M(r)$ is the total gravitating mass within radius r and n_{gas} and T are respectively the X-ray emitting gas density and temperature. Using the ideal gas law, the mass becomes:

$$M = -\frac{kTr}{G\mu m_p}\Big(\frac{dlog(n_{gas})}{dlog(r)} + \frac{dlog(T)}{dlog(r)}\Big)$$

where μ is the mean molecular weight and m_p is the proton mass.

The X-ray halo with a central luminosity peak and M87 is the nearest X-ray luminous galaxy center. Moreover, the temperature of the X-ray halo of M87 is relatively low with values in the range $1-3$ keV, a temperature range where spectra are very rich in emission lines (for these reasons, M87 was made one of the targets of the XMM-Newton mission).
The fact that Virgo cluster halo is nearly circular and smooth with a short cooling time suggested that M87 sits in the center of a modest cooling flow. Actually, the presence of filaments in the inner halo suggest disturbed and disordered flow rather than a simple cooling-driven inflow. On one hand, there is the slow cooling-driven inflow of the hot cluster gas and on the other hand the strong outflow energy from the supermassive black hole. However, this outflow is likely to be transient and if it decreases or stops, the cooling flow would dominate. The radio-loud and X-ray loud plasmas are interacting strongly in the core of the Virgo Cluster. The cooling flow caused by radiative losses from the ICM ($L_X \propto n_{gas}^2$ where n_{gas} is the gas density from X-ray measurements) as expected for a cluster-center galaxy is balanced in M87 by heating from the feedback by the AGN. In other words, what is seen in the radio halo is heating the cluster and may balance L_X. The total ICM thermal energy is given by its temperature ($E = \frac{3}{2}n_{gas}kT$) and the cooling time as the ratio between the total energy and the radiative loss rate is therefore:

$$t_{cool}[yr] = 1.4 \cdot 10^8 \Big(\frac{kT_{gas}}{2\,keV}\Big)^{1/2}\Big(\frac{n_{gas}}{0.1\,cm{-}3}\Big)^{-1}$$

meaning that high-density regions cool faster, which is the case of the core of a cluster.
This cooling time can be calculated by measuring T and n_X from ICM bremsstrahlung emission and for M87 is $\simeq 1$ Gyr. In this case, however, there is an internal source of energy that keeps the cluster core hot: the active nucleus with its jet outflows.

Chapter 3

Data analysis

3.1 Spectral analysis

The radio spectrum of galaxies and quasars is dominated by thermal (bremsstrahlung) and non-thermal (synchrotron) emission and both are continua.
Although the radio spectrum of only a few sources follows simple power law, a spectral index may be defined by the measurement of flux densities between any two arbitrarily selected frequencies. Therefore radio spectra are usually displayed in the form of a logarithmic plot $log\, F_\nu - log\, \nu$, where F is the flux density which correspond to the integral of its intensity over some solid angle and ν is the frequency. In radioastronomy, the flux is usually measured in Jansky (Jy), where $1Jy = 10^{-23} erg\, s^{-1} cm^{-2} Hz^{-1}$.
Spectral index maps represent a powerful tool to study the properties of the relativistic electrons and of the magnetic field in which they emit [1], and to investigate the connection between the electron energy distribution and the surrounding medium.

Considering the flux density of a source at two different frequencies, the spectral index is given by:

$$\alpha = \frac{log(F_{\nu_1}/F_{\nu_2})}{log(\nu_1/\nu_2)} \tag{3.1}$$

knowing that $F_\nu \propto \nu^\alpha$ in case of synchrotron emission, as shown in 3.10.
The observed spectrum of extended sources generally shows a negative curvature in the $log\, F_\nu - log\, \nu$ plane, meaning that the spectrum becomes steeper at high frequency. Typically the region of curvature extends over a decade or so of frequency (Verschuur & Kellermann, 1988). Far from the maximum curvature, the spectrum can be represented by two well-defined spectral indices. In general, regions of flatter spectra are indication of the presence of more energetic radiating particles, and/or of a larger value of the local magnetic field strength, considering that the electron lifetime depends on these parameters as will be shown in the next section.
Values of the spectral index of the extended radio features are usually in the range $(-1.3 - -0.5)$, with a strong concentration near the value -0.80 ± 0.15 (Kellermann & Owen, 1988).

[1] However, the index merely describes the relation between emission at different frequencies and is not always physically associated with a property of the electrons and/or field.

Regions of radio sources with spectra flatter than -0.5 are nearly always very compact and are coincident with an AGN. In these sources, the flat spectrum is thought to be the result of self-absorption, rather than a flat electron energy distribution. If the plasma of the compact emitting source is optically thick, the same population of electrons that produced synchrotron light can absorb it, as will be explained in the following section.

3.2 Non-thermal processes

Much of the electromagnetic radiation emitted by AGN is very different from a stellar emission, but it is dominated by non-thermal emission from processes such as synchrotron, inverse Compton and others. Non-thermal refers to the fact that the statistical motion of the particles, and so features of the emitted radiation, do not depend on the temperature, as happens in the Maxwell-Boltzmann distribution where the particles are assumed to be in thermodynamic equilibrium.

Diffuse synchrotron radio sources have been observed and radio halos are the clearest evidence of the presence of magnetic fields and cosmic ray mixed with the thermal intracluster medium in the central regions of clusters of galaxies, as for M87. Electrons (and positrons) injected in the ICM by the AGN lose energy mainly because of synchrotron emission. Other processes are inverse Compton scattering with the Cosmic Microwave Background (CMB) photons and the AGN radiation field, but also Coulomb interactions and bremsstrahlung emission.
Relativistic proton energy losses are due to pp inelastic scattering and Coulomb interactions, implying lifetimes comparable to the diffusion time scale over the cluster size, so that they can be accumulated in the cluster volume. The proton loading is bulk kinetic energy density and not constrained by the emissivity directly.

3.2.1 Synchrotron emission

Synchrotron emission plays an important role in active galaxies, from the large scale structure and lobes to the inner jets. The ingredients to prepare it in a certain region are: high-energy particles, radiation and magnetic field, all essential, especially the latter, and connected to each other. Synchrotron radiation is non-thermal emission of radiation by relativistic particles spiraling in a magnetic field. The particle is forced to move in a helix with its axis parallel to the magnetic field. Hence, there is emission of electromagnetic radiation in the direction of the particle's motion. From now, only electrons will be taken into account, considering that ions' synchrotron emission is usually negligible compared to electrons' one. This is almost always true within astrophysical plasma containing ions and electrons, because the emitted power as will be shown goes like m^{-2}, hence the synchrotron radiation comes mainly from the lightest particles [2].

[2]However, there are situation where protons synchrotron emission could be important. In fact, adopting magnetic field in jets ($B \geqslant 1mG$) larger than the field used in electron synchrotron or IC models and assuming proton acceleration in jets up to energies $E_p \simeq 10^{18}eV$ with slow propagation, it is possible to obtain effective cooling of protons via synchrotron radiation on reasonable timescales.

This non-thermal emission was first proposed by Shklovskii and Herlofson (1950) to be the radiation mechanism responsible for the then newly discovered radio sources, like local supernova remnants and AGN. Strong linear polarization was its first, and is still the strongest, signature. A preferred direction for the electric field is established by the fact that the acceleration of the charge is always perpendicular to the field, whereas thermal processes are unpolarized.
The first astrophysical source detected by synchrotron was the jet of M87 in 1956 (Burbidge).

The energy of the emitted photons depends on the electron energy (E_{el}), on the magnetic field strength (B) and on the pitch angle ($\mathscr{P}$), which is the angle between electron velocity (v) and the magnetic field lines.
The pattern of the emitted radiation here is completely different from the classical regime, where a non relativistic particle radiates in the observer's frame with a symmetric dipole power pattern around the direction of acceleration. The synchrotron radiation is concentrated in a narrow cone [3] around the electron's velocity vector with an opening angle $\phi \simeq 1/\gamma$, called the beaming angle, where $\gamma = (1-\beta^2)^{-1/2}$ is the Lorentz factor. Hence, the pattern for a relativistic electron is strongly beamed in the forward direction as a direct consequence of the aberration of light for relativistic particles and an observer will see it (i.e. will measure an electric field) within the beaming cone of total aperture angle $2/\gamma$.
Therefore, the received pulses have a duration Δt much smaller than the gyration period $\omega_g = 2\pi\nu_g = \frac{eB}{\gamma mc}$ and the observed frequency is:

$$\nu \simeq 1/\Delta t \simeq \gamma^3 \nu_g = \gamma^2 \nu_0 \tag{3.2}$$

where $\nu_0 = \frac{v}{2\pi r_L} = \frac{eB}{2\pi mc}$ is the non-relativistic gyration frequency and $r_L = V_\perp^2/a_\perp$ is the Larmor radius. The higher the velocity of an electron, the higher the Lorentz factor, the shorter the pulse duration and the narrower the cone.
Moreover, the synchrotron frequency is a factor γ^3 greater than the the fundamental frequency, and a factor γ^2 greater than the Larmor frequency, defined as the typical frequency of non-relativistic particles. Then the particle is expected to emit most of its power at this frequency.
The power per unit frequency emitted by an electron of given Lorentz factor and pitch angle is:

$$P_s(\nu, E, \mathscr{P}) = \frac{\sqrt{3}e^3 B sin\mathscr{P}}{mc^2} F(\nu/\nu_c) \qquad\qquad F(\nu/\nu_c) \equiv \nu/\nu_c \int_{\nu/\nu_c}^{\infty} K_{5/3}(y)\,\mathrm{d}y \tag{3.3}$$

where ν_c is the critical frequency:

$$\nu_c = \frac{3}{2}\,\gamma^3\,\nu_g\,sin\,\mathscr{P} \propto E^2\,B \propto \gamma^2\,B \tag{3.4}$$

This could be useful as interpretation of non-thermal X-ray emission from large-scale extragalactic jets (Aharonian, 2004).

[3] Actually, half of the photons are emitted within the cone. Note that this does not mean that half of the power is emitted within $\simeq 1/\gamma$, because the photons inside the beaming cone are more energetic than those outside, and are more tightly packed.

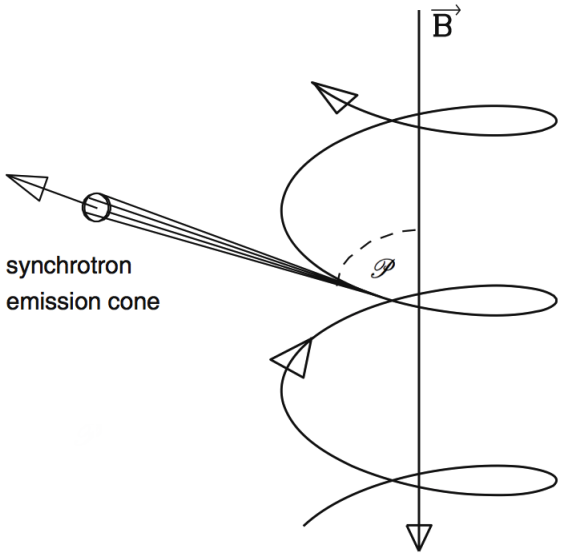

Figure 3.1. *The cone formed by the synchrotron emission of an electron, following an helical motion around magnetic field lines with pitch angle $\mathscr{P}$. The opening angle of the cone is inversely proportional to the Lorentz factor γ, in other words it becomes smaller for energetic electrons. When the particle is relativistic, the pattern strongly changes due to the aberration of light, and is strongly beamed in the forward direction (adapted from Beckmann & Shrader, 2012).*

This is the power integrated over the emission pattern and $K_{5/3}(y)$ is the modified Bessel function of order 5/3. The frequency dependence is given by $F(\nu/\nu_c)$, which peaks at:

$$\nu = 0.29\nu_c$$

The low-frequency asymptotic form of $F(\nu/\nu_c)$ is a power law of the form $\nu^{1/3}$, whereas the high-frequency one shows an exponential cutoff (Rybicki & Lightman, 1986).

The total radiated power averaged over an isotropic distribution of pitch angles, is:

$$P_s = -\frac{dE_{el}}{dt} = \frac{4}{9}\frac{e^4\,B^2\,\gamma^2\,v^2}{c^5 m^2} = \frac{4}{9}\frac{e^4\,B^2\,E_{el}^2}{c^7 m^4} \tag{3.5}$$

Note that this mechanism, because of the mass dependance, is much more efficient for electrons and positrons than for protons, and the formula can be written in a more compact form, using the Thomson cross section $\sigma_T = \frac{8\pi}{3}\cdot r_0^2$ where $r_0 = \frac{e^2}{m_e c^2}$ and the magnetic energy density $U_{mag} = B^2/8\pi$:

$$P_s = \frac{4}{3}\sigma_T\, c\, \gamma^2\, U_{mag} \tag{3.6}$$

valid for highly relativistic electrons (v $\longrightarrow$ c). Then, the synchrotron luminosity becomes a function only of the magnetic energy density and of the Lorentz factor.
Remember that this value has been averaged over an isotropic distribution of pitch angles $\mathscr{P}$ because an electron during its lifetime is randomly scattered. In conclusion, this is the average loss rate for an individual electron of energy E_{el}.

For a single radiating relativistic electron, it is possible to define a cooling time:

$$t_{cool} \equiv \frac{E}{P_s} \simeq \frac{400}{E[TeV]B^2[G]}[s] \tag{3.7}$$

In AGN jets, typical magnetic field are smaller than 1 G and electrons energies are about 1 TeV, hence cooling time less than 1 yr and synchrotron peaks are in the UV and X-ray wavelength region.

The synchrotron spectrum from an ensemble of electrons in the optically thin limit depends only on the energy distribution of the electrons. The population of relativistic electrons is described by a power law distribution (e.g. the observed energy distribution of cosmic rays)

$$N(E) = N_0 \cdot E^{-p} \tag{3.8}$$

where p is the spectral index assumed constant. Therefore, the total synchrotron emissivity, which is defined by the power per unit frequency and per unit volume, is:

$$\epsilon(\nu, \mathscr{P}) = \int_{E_1}^{E_2} P_s(\nu, E, \mathscr{P})\, N(E)\, \mathrm{d}E \qquad [erg\, cm^{-3} s^{-1} sterad^{-1}] \tag{3.9}$$

where E_1 and E_2 describe the energy interval of the electrons. Performing the integration, the result is a power law:

$$\epsilon(\nu, \mathscr{P}) \;\simeq\; B^{\frac{p+1}{2}}\, \nu^{\frac{1-p}{2}} \simeq B^{1-\alpha}\, \nu^{\alpha} \qquad \alpha \equiv \frac{1-p}{2} \tag{3.10}$$

where α is the spectral index. Therefore, a power law energy distribution of non-thermal particles radiates a power law emission spectrum and their spectral indices are directly connected.
What is really observed in a spectrum is a superposition of these single electron spectra, therefore the slope is less steep.

Note that to obtain a realistic synchrotron spectrum it is necessary to specify the pitch angle distribution. Although usually assumed to be isotropic, there are two scenarios, both with an initial energy spectrum of the form of eq. 3.8:

- the Kardashev-Pacholczyk (KP) model (Kardashev, 1962; Pacholczyk, 1970)
  the pitch angle of the synchrotron emitting electrons cannot change with time, therefore it remains in its initial orientation with respect to the magnetic field;
- the Jeffe-Perola (JP) model (Jaffe & Perola, 1973)
  the pitch angle are continously and quickly re-isotropized on a time scale shorter than the radiative time scale.

The JP model is more realistic in the sense that a pitch angle distribution gradually becomes isotropic due to scattering on the magnetic field strength.
Major differences between the two models are visible at frequencies higher than the break frequency ν_b that is related to the time elapsed from the injection and to the magnetic field.

The observed spectrum of synchrotron emission has not the form $\epsilon(\nu) \propto \nu^{\alpha}$ moving to lower frequencies. In fact, the spectrum breaks at a certain ν_{sa}, the so-called synchrotron self-absorption frequency. The point is that, at low-frequency, the plasma of the compact emitting source is optically thick, causing the absorption of synchrotron light by the same population of electrons that produced it, producing the synchrotron self-absorption process.

Considering the power law energy distribution as a superposition of Maxwellians of different temperatures, it is possible to relate the energy γmc^2 of a given electron to the energy kT of a Maxwellian:

$$kT \simeq \gamma mc^2 \simeq mc^2(\nu/\nu_0)^{1/2}$$

For a non-thermal emission, it is useful to define the brightness temperature T_b, which is the equivalent black body peak temperature for the observed emission. For an optically thick source, in other words at low-frequency in the Rayleigh-Jeans limit for a Planck function (B_ν), the brightness temperature is:

$$I_\nu = \frac{F_\nu}{\pi\Phi^2} = B_\nu = \frac{2k\,T_b\,\nu^2}{c^2} \quad \longrightarrow \quad T_b = \frac{I_\nu\,c^2}{2k\,\nu^2} \tag{3.11}$$

where I_ν is the surface brightness, f_ν is the flux observed at a frequency ν, θ_s is the angular dimension of the source and k is the Boltzmann's constant. For an absorbed source, the mean electron energy must be equal to $3/2kT_b$ and so the intensity in the optically thick case is:

$$I(\nu) \propto \nu^{5/2} \tag{3.12}$$

Note that the optically thick part of the spectrum does not depend on the power law index p of the electron energy distribution and also the particle density disappeared: the more electrons you have, the more you emit, but the more you absorb.
The transition frequency where the emitting region becomes optically thin is the already cited ν_{sa}. Here, the spectrum reaches its maximum, as it is shown in figure 3.2. Now, going from the intensity to the flux, that is integrating $I(\nu)$ over the angular dimension of the source θ_s, the following relation is obtained:

$$F(\nu) \propto \theta_s^2\,B^{-1/2}\,\nu^{5/2}$$

therefore, observing a self-absorbed source of known angular size, it is possible to derive its magnetic field (only if homogeneous) even without knowing its distance.

3.2.2 Other processes: inverse Compton and Bremsstrahlung

In AGN, there are other observed processes beyond the synchrotron emission, which lead to electron energy losses. In fact, synchrotron dominates the jets physics but for instance inverse Compton emission is the responsible for radiation from the accretion disk and its proximity. Moreover, in clusters of galaxies the population of relativistic electrons responsible for the diffuse non-thermal synchrotron radio emission can scatter the CMB photons, producing hard X-ray radiation.

A brief description of these processes is following, while a complete discussion can be found in Rybicki and Lyghtman (1986).

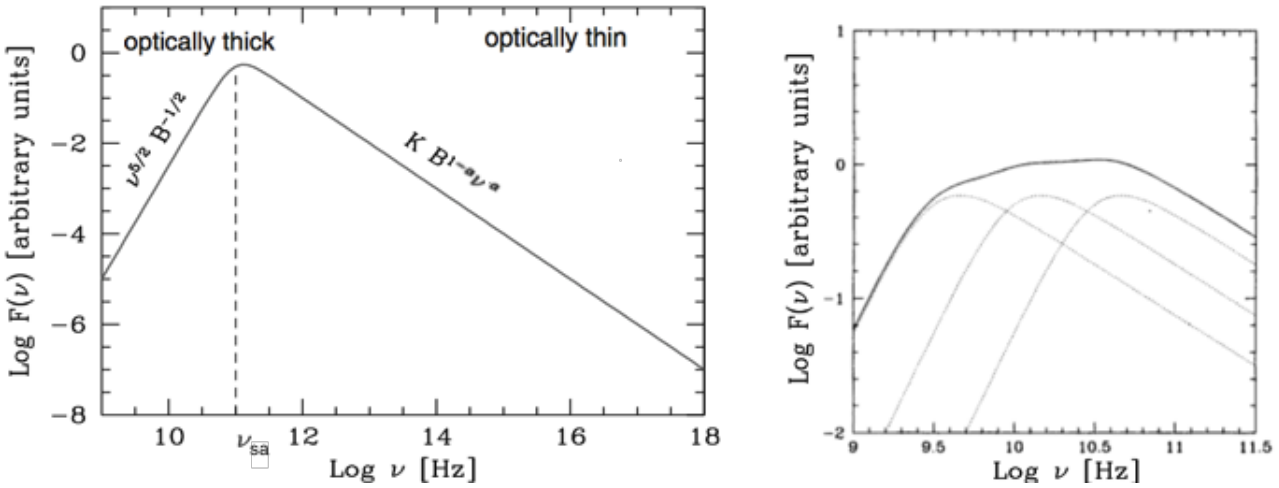

Figure 3.2. *On the left, the synchrotron spectrum for a single electron, represented with a logarithmic scale for the observed flux and for frequencies. Note the different slope and dependance from p (power law index of the electron energy distribution) before and after the self-absorption frequency. Observations of the self absorbed part could determine B, whereas observations of the thin part can then determine K and the electron slope p.*
On the right, the flat spectrum made by superposition. Each of the dotted curves represents the emission from a single region; the solid curve is their sum. Each region has the same $F(\nu_{sa})$, but the values of ν_{sa} are $\simeq 3, 10, 31$ GHz respectively (Krolik, 1999).

- Inverse Compton scattering (IC)
  describes when a relativistic electron scatters a photon, increasing the photon's energy. This is opposite to Compton scattering, where a photon transfers energy to an electron. For instance, radio and infrared photons can be "up-scattered" to X-ray or gamma-ray energies, depending on how relativistic the electrons are. In AGN, X-ray emission is produced by IC scattering of the jet electrons with the CMB photons.

  Performing a Lorentz transformation between the electron's frame and the laboratory frame and using the relativistic Doppler shift formula, it is possible to calculate the final photon energy E_2 in term of the Lorentz factor and the initial energy E_1:

$$E_2 \simeq \gamma^2 E_1 \tag{3.13}$$

  There is a maximum in the energy gain determined by the energy conservation of the process (which is a conservative single scattering process): $E_2 \leqslant E_1 + \gamma mc^2$.

  The total power, of this process is a function of the radiation energy density U_{rad}:

$$P_{IC} = -\frac{dE_{el}}{dt} = \frac{4}{3}\sigma_T\, c\, \gamma^2\, U_{rad} \tag{3.14}$$

  Note that synchrotron (eq. 3.6) and IC (eq. 3.14) losses both have the same electron energy dependence, so their effects on radio spectra are indistinguishable and the cooling time trend is exactly the same.

Moreover, comparing the synchrotron and IC emitted powers, a relation between magnetic field energy density and photons energy density can be found:

$$\frac{P_s}{P_{IC}} = \frac{U_{mag}}{U_{rad}} \tag{3.15}$$

- Synchrotron inverse Compton (SIC)
  known also as synchrotron self-Compton (SSC), consists of synchrotron emission followed by inverse Compton process. It occurs when photons, emitted by an ensemble of relativistic electrons through synchrotron mechanism, are then up-scattered by the same ensemble, increasing their frequency. Note that this is only possible if the radiation energy density (U_{rad}) is high enough in order for the photons to interact with the electrons population. This is the case of an optically thick plasma. Note that also the up-scattered photons might contribute again to U_{rad}.
  The SIC spectrum has the same spectral index α as the synchrotron component, therefore $\epsilon_{SIC}(\nu) \propto \nu^{\alpha}$. However, the maximum energy of the SIC component, which usually is also the peak energy in a SED representation, is a factor γ^2 higher than the maximum energy of the synchrotron component. An example of this process can be found in blazars, where there is a typical double-peaked SED (fig. 3.3).

Knowing the ratio between the two processes' luminosities, it can be derived that:

$$\frac{P_{SIC}}{P_s} = \frac{U_{rad}}{U_{mag}} \propto \left(\frac{T_b}{10^{12}}\right)^5 \tag{3.16}$$

The brightness temperature is limited by the fact that the radiation energy cannot exceed the electron mean energy, then:

$$kT_b \leqslant k\frac{\gamma mc^2}{3k} \quad \longrightarrow \quad T_b \leqslant \left(\frac{B}{1\mu G}\right)^{-1/2}\left(\frac{\nu}{1GHz}\right)^{1/2} \cdot 10^{12}\, K \tag{3.17}$$

knowing that $\gamma = \sqrt{2\pi\nu\frac{mc}{eB}}$. Therefore, T_b does not significantly exceed $10^{12}\, K$, in order to maintain an optically thin source. This value is also called Compton limit temperature for an incoherent synchrotron source. In fact, as soon as T_b sighltly exceeds $10^{12}K$, the inverse Compton branch will dominate very rapidly on the synchrotron emission, causing the so-called inverse Compton catastrophe. However, this result is not observed; therefore there must be some mechanism that is physically limiting the possible values of the brightness temperature in an electron plasma of AGN. Sources might still appear "hotter" when they are Doppler boosted towards the observer (T_b depends on quantities, such as flux, frequency and angular dimension, that are affected by Doppler boosting) or the emission might come from a coherent ensemble of electrons.

- Thermal bremsstrahlung
  is an other important mechanism for electron energy losses. It is also called free-free emission because the electron and the interacting particle are not bound before and after the scattering. In fact, the electron interacts with a free charged particle, usually a ion, emitting radiation. The free-free scattering takes place in hot, non-relativistic plasma, like the intracluster gas.

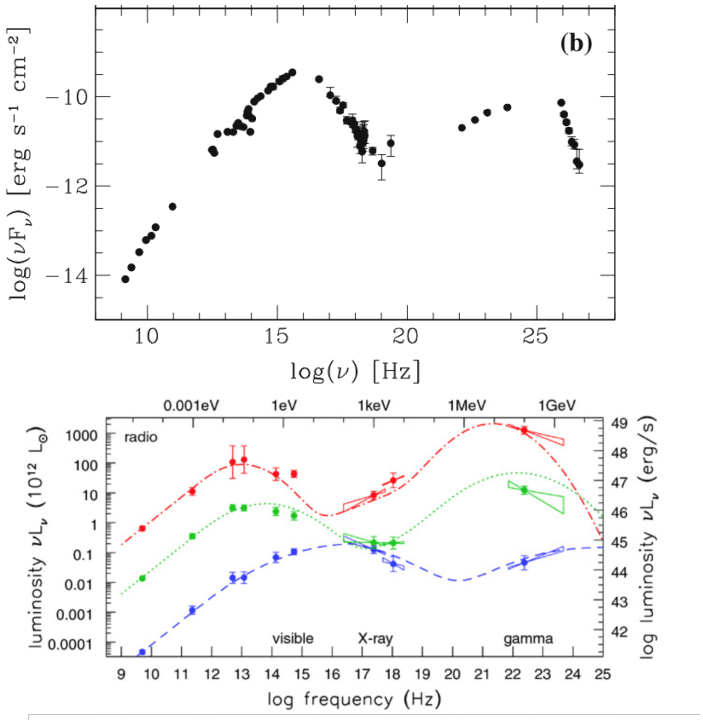

Figure 3.3. At the top, SED of the BL Lac PKS 2155-304. The gamma-ray spectral shape is determined by the high-energy tail of the electron distribution and by the shape of the spectrum of the scattered photons, which can be either optical-to-soft-X-ray synchrotron photons (SIC) or photons external to the jet, like those from the accretion disk, BLR and dust torus (external Compton) (Falomo et al., 2014).
At the bottom, average SED for blazars, grouped by radio power: the most radio-bright are also the most luminous in gamma-rays. The lower-energy peaks in the UV and X-ray regions represent synchrotron radiation from electrons in the jet; these photons scatter from the same spiralling electrons to produce the gamma-ray peak. When the electrons are more energetic, both peaks move to higher frequency (Fossati et al., 1998).

3.2.3 Equipartition

As previously said, the field strength cannot be derived from the synchrotron spectrum alone. Since observed emission also depends on the electron number density and geometry. If an equilibrium condition is reached, for instance for extremely tangled fields and trapped particles with no further acceleration and dominating synchrotron losses, an estimate can be obtained by minimizing the total energy constrained by the non-thermal luminosity and spectral index. In other words, since the energy density in the magnetic field and in the relativistic particles both enter the synchrotron luminosity, the energy is minimized within some (possibly unknown) volume (V) of the radio source (Pacholczyk, 1970).
Under some assumptions about physical properties of the radio source, the derivation of magnetic field strengths averaged (over the entire volume of the beam) as a function of the radio source luminosity is possible.
The total energy density of a synchrotron source is $U = U_e + U_p + U_{mag}$ due to the energy in relativistic particles only (electrons and protons, U_e and U_p respectively) and the energy in magnetic fields (U_{mag}).
The latter is defined as:

$$U_{mag} = \int \frac{B^2}{8\pi} \, \mathrm{d}V = \frac{B^2}{8\pi} f V$$

where f is the filling factor that is the fraction of the source volume V occupied by the magnetic field.
Note that the energy contained in the heavy particles U_p can be related to U_e assuming $U_p = kU_e$. If the population of relativistic electrons have an energy spectrum described by the equation in 3.8, therefore the electron energy is:

$$U_e = V \cdot \int_{E_1}^{E_2} E \cdot N(E) \, \mathrm{d}E = V \cdot \frac{N_0}{2-p} \cdot (E_2^{2-p} - E_1^{2-p}) \tag{3.18}$$

where E_1 and E_2 describe the energy interval of the electrons and N_0 is a constant that can be evaluated if the distance to the source is known.
The source luminosity is:

$$L = V \cdot \int_{E_1}^{E_2} P_s \cdot N(E) \, \mathrm{d}E = V \cdot \frac{N_0 \, \frac{4}{3} \sigma_T c \, U_{mag} \, m^2 \, c^4}{3-p} \cdot (E_2^{3-p} - E_1^{3-p}) \tag{3.19}$$

where P_s is the energy loss rate defined by eq. 3.6. Now, it is possible to solve for N_0, using eq. 3.18 and 3.19 with the following result:

$$U_e = C_e \cdot \frac{L}{B^{3/2}} \tag{3.20}$$

where all the constant factors are in C_e, such as the spectral index and the cutoff energies. Note that for the latter ones, it was assumed the relation $\omega_i = \gamma_i^3 \cdot \omega_L \propto E_i^2 \cdot B$ (where i = 1, 2) expressing the energies in terms of the respective observed frequency and B. The observer measures a frequency $\omega_i = \gamma_i^3 \cdot \omega_L$ where $\omega_L = \frac{eB}{m\gamma c}$ is the Larmor frequency for a relativistic electron. The gamma factors arise when the frequency is measured in the rest frame of the observer: one factor is due to the transformation from the particle frame into that one and one factor is due to the relativistic beaming effect on the cone of particle emission.
Finally the total energy is obtained as a function of the magnetic field:

$$U = (1+k)U_e + U_{mag} = (1+k)C_e \cdot \frac{L}{B^{3/2}} + \frac{B^2}{8\pi} f V \tag{3.21}$$

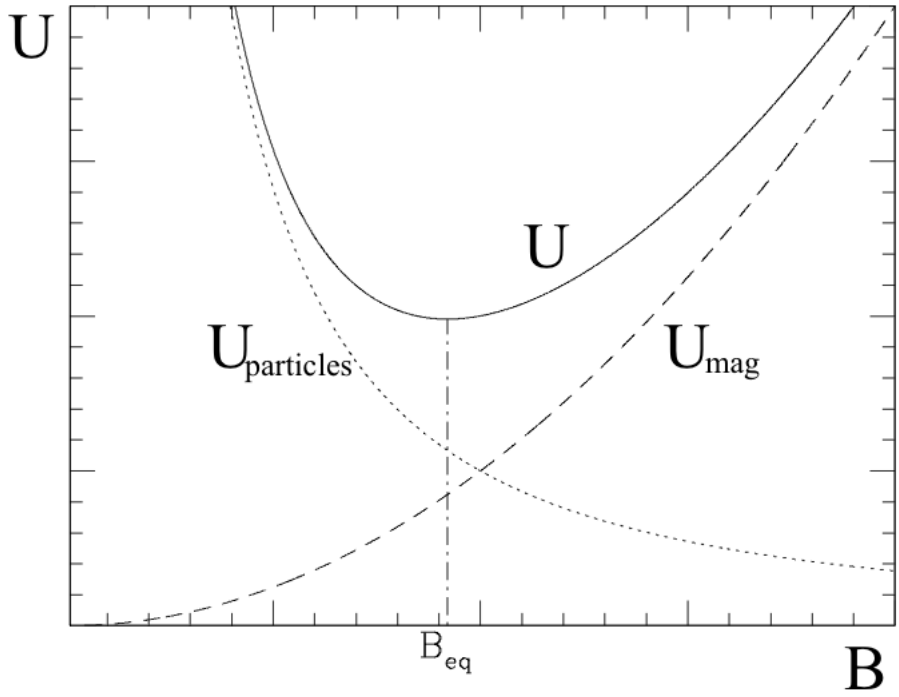

Figure 3.4. *Energy content in a radio source in arbitrary units. The magnetic energy is $U_{mag} \propto B^2$, whereas the energy in relativistic particles is $U_e + U_p \propto B^{-3/2}$. The total energy content U is minimum when the contributions of magnetic fields and relativistic particles are approximately equal, that is the equipartition condition, and B_{eq} is the corresponding magnetic field value (Govoni & Feretti, 2004).*

To estimate the magnetic field strength, it is necessary to make some assumptions about how the energy is distributed between the fields and particles. A useful estimate is the condition of minimum energy: the magnetic field strength that minimizes U within a specified volume, luminosity and number of particles is the value that verifies this equation $(\partial U/\partial B)_{V,L,N} = 0$. Therefore, the "equipartition" field is:

$$B_{eq} = \left[6\pi(1+k)C_e \frac{L}{fV}\right]^{2/7} \tag{3.22}$$

where L/V is the synchrotron emissivity. The minimum energy is:

$$U_{min} = C(1+k)^{4/7} f^{3/7} V^{3/7} L^{4/7} \tag{3.23}$$

and the minimum energy density is:

$$u_{min} = \frac{U_{min}}{fV} = C(1+k)^{4/7} f^{-4/7} V^{-4/7} L^{4/7} \tag{3.24}$$

and

$$U_{mag} = \frac{3}{4}(1+k)U_e$$

.

The minimum energy is obtained when the contributions of the magnetic field and the relativistic particles are approximately equal (fig.3.4), hence "equipartition". Note that this assumption was first proposed by Burbidge in 1956 applied to the optical synchrotron emission of M87 jet.

Expressing the parameters in commonly used units, the equipartition magnetic field of a radio source can be written in terms of observed quantities:

$$B_{eq}[G] = \sqrt{\frac{24\pi}{7} u_{min}[erg\, cm^{-3}]} =$$

$$= \sqrt{\frac{24\pi}{7} \xi(\alpha, \nu_1, \nu_2)\, (1+k)^{4/7}\, (\nu_0[MHz])^{4\alpha/7}\, (1+z)^{\frac{12+4\alpha}{7}}\, (I_0[mJy\ arcsec^{-2}])^{4/7}\, (d[kpc])^{-4/7}} \tag{3.25}$$

where α is the spectral index between two frequencies ν_1, ν_2, z is the source redshift, I_0 is the source brightness at a frequency ν_0, d is the source depth [4], and ξ is a function equal to $\frac{2\alpha-2}{2\alpha-1} \cdot \frac{\nu_1^{(1-2\alpha)/2} - \nu_2^{(1-2\alpha)/2}}{\nu_1^{(1-\alpha)} - \nu_2^{(1-\alpha)}}$ (Govoni & Feretti, 2004). Moreover, the filling factor f is chosen equal to 1, meaning that particles and magnetic fields occupy the entire volume, filling it homogeneously

This result is based on several assumptions, whose validity is not obvious, on the properties of the radio emitting region and on the condition of minimum energy of the observed relativistic plasma, such as (Pacholczyk, 1970; Miley, 1980):

- the volume filling factor, which is usually assumed in literature equal to 1 for clusters;
- the field is considered completely tangled with no preferred direction;
- the value of the ratio of the energy in relativistic protons to that in electrons, which depends on the mechanism of generation of relativistic electrons is poorly known. The value k = 1 is usually assumed, meaning that the particle energy is equally divided between electrons and protons, or the value k = 0, where all of the particle energy is in the relativistic electrons (and positrons), in line with the idea that the jets could be mainly composed of these constituents (Reynolds et al., 1996). In literature, there is also the results for the assumption of k = 10, as an upper limit from what predicted by electromagnetic acceleration models involving protons and electrons (Bell, 1978).
- the source along the line of sight is another parameter difficult to infer;
- integration of the radio spectrum usually from 10 MHz and $10 - 100$ GHz, that is the typical range accessible to observations [5];

[4] The source depth is estimated from the spatial extent of the observed emission for a constant homogeneous magnetic field filling the entire source volume.

[5] The computation of equipartition parameters based on the integration of the synchrotron radio luminosity between two fixed frequencies has some problems. In fact, a fixed frequency range corresponds to an energy range that depends on the magnetic field, which varies in different parts of the source. The corresponding electron energies depend on the magnetic field value, thus the integration limits are variable in terms of the energy of the radiating electrons. The lower limit is particularly relevant, owing to the power-law shape of the electron energy distribution and to the fact that electrons of very low energy are expected to be present. See Beck & Krause (2005) for an other approach.

3.2.4 Aging and spectral models

When dealing with extragalactic sources, the lifetime of the radiating electrons is an important factor, known as the synchrotron age. This depends on B and U_{rad}. The electron energy spectrum evolves with time and so does the luminosity of source.
Even if electrons are initially produced with a single power law distribution, differential energy losses make the spectrum steeper at higher energy because the particles emit at different rates.
Relativistic electrons lose energy by synchrotron and by the inverse Compton processes (subscript s), which are both proportional to the square of the energy; by ordinary bremsstrahlung and adiabatic expansion (subscript b), which are directly proportional to the energy; and by ionization (subscript i), which is approximately proportional to the logarithm of the energy. Approximating the logarithmic term by a constant, the general rate of energy loss may be written:

$$b = -\frac{dE}{dt} = -\dot{E} = A_s \cdot E^2 + A_b \cdot E + A_i \tag{3.26}$$

It is of interest to consider the case where synchrotron and IC losses dominate, with neglectable expansion losses and re-accelaration processes: $A_b = A_i = 0$. As shown in eq. 3.5, the value of A_s is $\frac{4}{9}\frac{e^4 B^2}{c^7 m^4} = C\,B^2$ and so $\dot{E} = -C\,B^2\,E^2$.

The synchrotron age for an ensemble of particles with the same initial energy due to synchrotron radiation is:

$$t_s = \frac{E}{\dot{E}} \propto \frac{E}{E^2 B^2} \propto \frac{1}{E B^2} \propto \frac{1}{\gamma B^2}$$

In an ensemble of particles with a wide range of initial energies, the higher-energy particles radiate faster so, after a time t, all particles with $t_e < t$ would no longer be radiating, causing a break in the power law of the observed synchrotron spectrum at a critical frequency

$$\nu_b \propto B^{-3} t^{-2}$$

known as break frequency, given by eq. 3.4.
The shape of the spectrum on either side of ν_b depends on the initial particle energy distribution and how it evolves with time. This break will displaces to lower frequencies over time and its value is fundamental to estimate the age of a population of relativistic particles (in addition to the magnetic field values).
For a more precise analysis, one can define $B_{rad} = \sqrt{8\pi U_{rad}}$, the equivalent field [6] due to IC scattering on CMB photons (Slee et al. 2001), in addition to the local field associated with the synchrotron emission $B(t)$. In this case, the energy loss rate is given by:

$$\dot{E} = -C\,[B(t)^2 + B_{rad}^2]\,E^2$$

from which it is possible to find the cutoff energy that is the maximum particle energy (and so for the break frequency) present in the ensemble after a time t_s known as synchrotron lifetime. Therefore, given ν_b that is a measured quantity, t_s can be calculated in case of homogeneous or inhomogeneous magnetic field:

[6] Note that B_{rad} is only a parameter, not a magnetic field, added for convenience in the formalism.

- if the particles see a constant field over their entire lifetime, either by moving through a homogeneous field or by not moving very far in an inhomogeneous field, then $B(t) = B$ and:

$$t_s \propto \frac{B^{1/2}}{B^2 + B_{rad}^2} \nu_b^{-1/2}$$

  In the synchrotron loss dominated regime, it is possible to neglect B_{rad} (IC scattering against the CMB are not important) and, as previously shown, computing all the constants, then

$$t_s[Myr] = 1610 \, (B[\mu G])^{-3/2} \, (\nu_b[GHz])^{-1/2}$$

- if the particles have encountered varying fields during their lifetimes, t_s must be modified. If they have spent a large fraction of their lifetime in a low field region before moving to a high-field region from where they are currently radiating, a synchrotron lifetime calculated from the observed ν_b will give ages that are shorter than the true lifetime of the particles.

Quantitative analysis of synchrotron aging in radio galaxies is difficult, since the spectra may vary across the source, particularly if the magnetic field is not constant and the high-frequency steepening occurs over a very broad range in frequency.
Relativistic electrons reach different regions at different times, so that the break frequency is an estimate for the time elapsed since their production (if the field is ordered). Generally, the hot spots and jets appear to have flatter spectra than the more extended diffuse components, apparently reflecting their younger ages and correspondingly smaller synchrotron radiation losses. The very diffuse components associated with clusters have the steepest observed radio spectra with indices generally steeper than -1.

As previously seen, the age of a population of particles is related to ν_b but the shape of the observed spectrum below and above this break depends on the initial particle energy distribution and its evolution with time.
The electron energy distribution function change obeys an equation of continuity in energy (Pacholczyk, 1970):

$$\frac{\partial N(E,t)}{\partial t} + \frac{\partial}{\partial E}[N(E,t) \cdot b] = Q(E,t) \tag{3.27}$$

where b is the loss and gain of energy by the electrons and Q(E,t) is the source term that gives the rate of injection into the radiating region at unit time and per unit energy interval.
Note that considering scattering of particles by magnetic field inhomogeneities adds a diffusion-like term:

$$\frac{\partial}{\partial E^2}[D \, N(E,t)]$$

where D is the diffusion coefficient along the energy axis.

There are many spectral aging models for equation 3.27, as shown in fig. 3.5, characterized by different forms of the source term:

- initial injection model
  here, $Q(E,t) = E^{-p}\delta(t - t_0)$ meaning that an initial power law distribution is allowed to

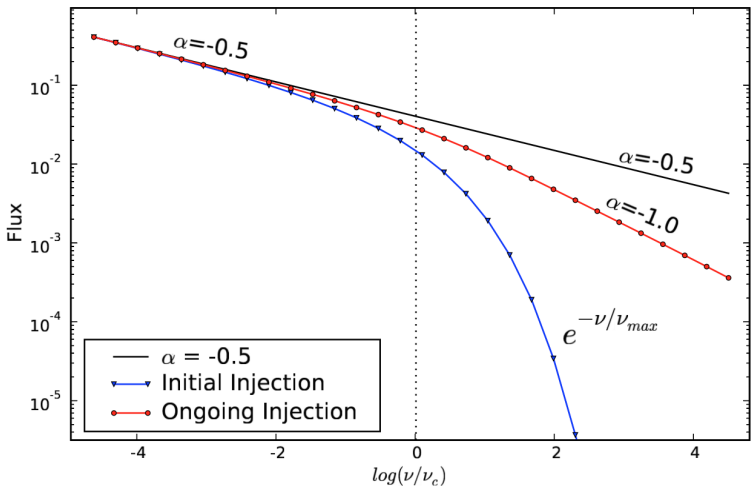

Figure 3.5. Spectral aging models resulting from no aging (solid line) that is the initial condition, aging via the initial (blue line) and ongoing (red line) injection models.
The chosen energy distribution is $N(E,0) \propto E^{-2}$, which corresponds to an initial power law spectrum with α = -0.5 (Urvashi, 2010). The flux is in arbitrary units.

age without replenishment. Particle aging produces a spectral break. Within the energy range over which this initial synchrotron spectral power-law holds, the spectral index on the low-frequency side of this break is $\alpha = -(p-1)/2$ and the spectrum on the high-frequency side shows exponential decay (from the single-energy power-spectrum at the highest surviving energy);

- ongoing injection model at steady state
  here, $Q(E,t) = E^{-p}$ meaning a constant input of particles with the same energy distribution and $\partial N(E,t)/\partial t = 0$ meaning a steady-state solution above ν_b. A set of particles with a power-law distribution of energies is continually injected into the system. Electrons at all energies are therefore aging as well as being replenished. However, since the high energy particles age faster, there will still be a break in the spectrum, but this break is not as sharp as for the initial injection model. The solution is given by $N(E) \propto E^{-p-1}$ and the resulting spectrum has a steepening of the spectral index by 0.5 across the break ($\alpha - \frac{1}{2}$);

- other models
  there are several other theoretical models for the evolution of synchrotron spectra that are based on non-uniform or time-variable magnetic fields and turbulence.

3.3 Intensity images

The Very Large Array can cover the low-frequency range from 73.8 to 330 MHz with a field of view from 700 to 150 arcmin, a sensitivity from 20 to 0.2 mJy and with a resolution from 24 to 5 arcsec. Note that in the case of M87, which is $\simeq$ 16.7 Mpc distant, the scale for angular resolution gives 1 arcsec = 81 pc.
The approximate synthesized beam size, as the full width at half-power, in arcsec for the central frequency is: for 4 band 24, 80, 260 or 850 and for P band 5.6, 18.5, 60 or 200 depending on which configuration of the array, respectively A, B, C and D (from the maximum to minimum antenna separation, see "Radio Interferometry" appendix).
Here, in figure 3.6, the intensity images of M87 that were used for this analysis:

- VLA image at 327 MHz (90 cm, P band; PI: F. Owen) with 7 arcsec resolution; the observation date is 1998/07/12 and the pointing center is 12:30:48.9 +12.23.26.3;
  it shows a bright central region that contains the jet and inner radio lobes, outflows to the east and west of the inner region and two fainter, larger regions to the north and south. The eastward-flow proceeds straight in a sort of cylinder and ends in a lobe, frequently called "the ear", whereas the westward flow, initially aligned with the jet, quickly twists towards south. Both flows come from the inner region and reach the halo edge, where they disperse (especially the westward one). Narrow bright extended filamentary structure is seen throughout the ear lobe/canal structures and the halo, with low-level diffuse background emission in between and with a typical length of $\simeq 10 arcsec \cdot 3 arcmin$;
  Owen et al. (2000) presented minimum pressure analysis for the magnetic fields and relativistic particles at the positions indicated in fig.3.7. All the filaments have somewhat lower minimum pressures than the surrounding thermal gas. This could imply that the synchrotron emitting regions are far from the minimum-pressure case, that the filling factor of the emitting regions is much less than 1, or that the thermal gas is mixed with synchrotron emitting regions and provides much of the pressure inside the filaments.

- VLA image at 74 MHz (4 m, 4 band; PI: R. Perley, N. Kassim) with 25 arcsec resolution; the observation date is 2001/01/19 and the pointing center is 12:30:49.5 +12.23.28;
  although less resolved than the 7" resolution 327 MHz image, it confirms some characteristic of the halo, showing the same structure observed for the 327 MHz image; moreover, a systematic error is present in the form of a sort of honeycomb structure. This is an artifact of deconvolution and it will affect the spectral index map with increased systematic errors, above all in the halo diffuse emission.

Together, these images well resolve the structure of the radio halo, showing a bright compact region of emission on top of a relatively faint diffuse background. They also show the same size of the radio halo with a sharp edge, the confinement of the radio-emitting plasma within its boundaries and the high surface brightness [7] of the compact central region with respect to the faint surface brightness of the extended radio emission.
M87 is a bright (200 Jy) radio galaxy located at the center of the Virgo cluster. The spatial

[7] The surface brightness is the measure of brightness (or flux) per area on the sky and it measured in $erg \cdot s^{-1} \cdot cm^{-2}$

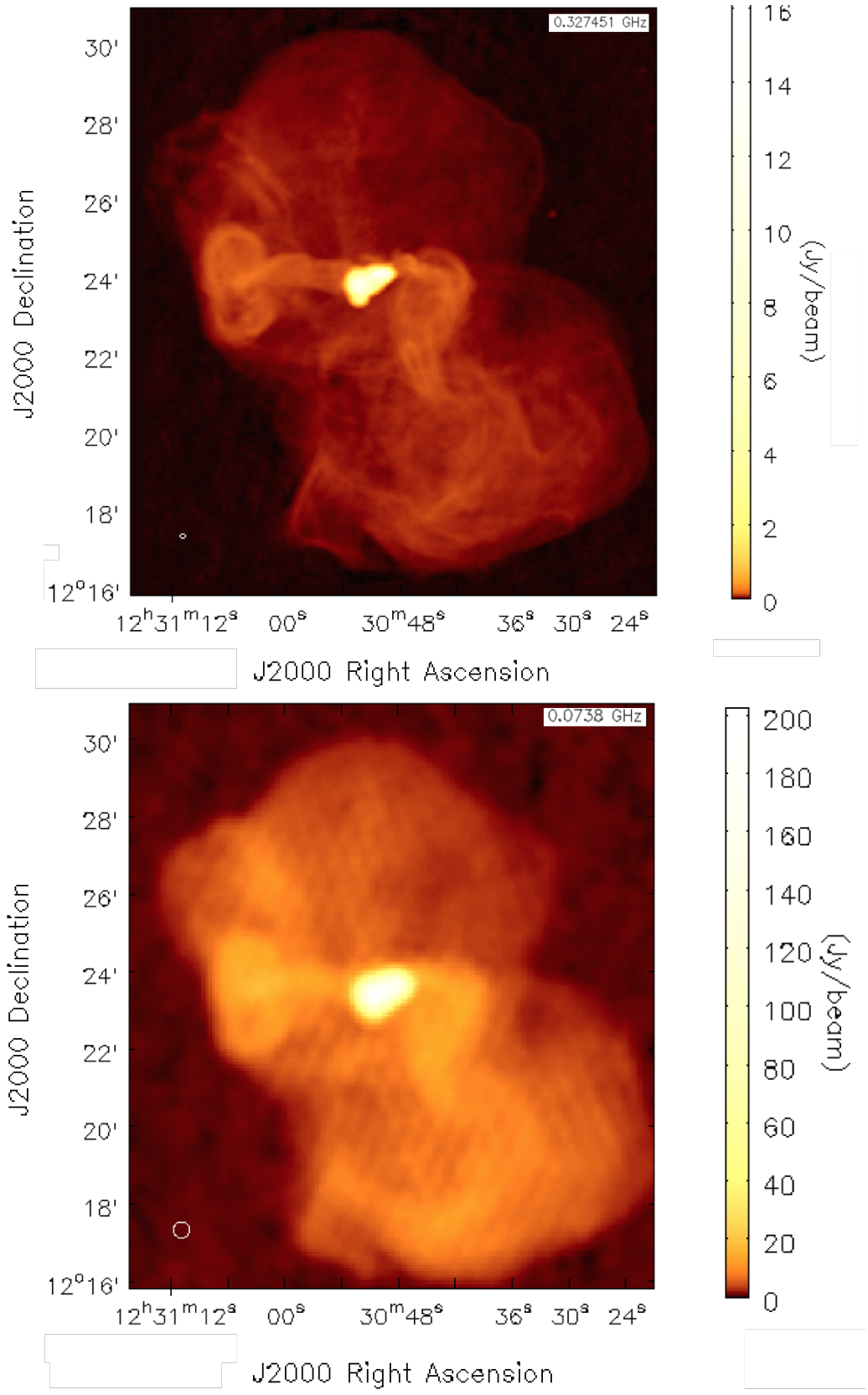

Figure 3.6. At the top, M87 image at 327 MHz (Instrument: VLA, A configuration, 90 cm) with 7 arcsec resolution. The rms noise level is 1 mJy/beam and the flux peak is 16.1 Jy/beam. The resolution and high dynamic range of this image are high.
At the bottom, M87 image at 74 MHz (Instrument: VLA, A configuration, 4 m) with 25 arcsec resolution. The rms noise level is 44 mJy/beam and the flux peak is 204.5 Jy/beam. The total-intensity images are displayed with the same flux-scale with a different range. The synthesized beam is shown in the bottom-left corner of each image.

distribution of broad-band synchrotron emission from this source consists of a bright central region (spanning a few arcmin) containing a flat-spectrum core, a jet with known spectral index of - 0.55 and two radio lobes with steeper spectra from - 0.8 to - 0.5 (Rottmann et al., 1996; Owen et al., 2000). This central region is roughly two orders of magnitude brighter than the brightest filaments in the extended diffuse radio halo that surrounded it (7 to 14 arcmin).

High resolution images of the 40 kpc-scale structure in the M87 halo have been made, in addition to the 327 MHz image by Owen et al. (2000), at higher frequencies by Rottmann et al. (1996) with the single-dish Effelsberg radio telescope at 69 arcsec resolution at 10.55 GHz.

To compare these images, it is necessary to match their angular resolution, convolving the 327 MHz image to the resolution of the 74 MHz image. All the measured flux values therefore will be in units of $Jy/beam = Jy/(25arcsec)^2$).
In order to match the coordinate system and the image pixel size, the 74 MHz image was regridded[8] with respect to the 327 MHz image.

[8]using the task "imregrid" in CASA that allows to regrid one image onto the coordinate system of another.

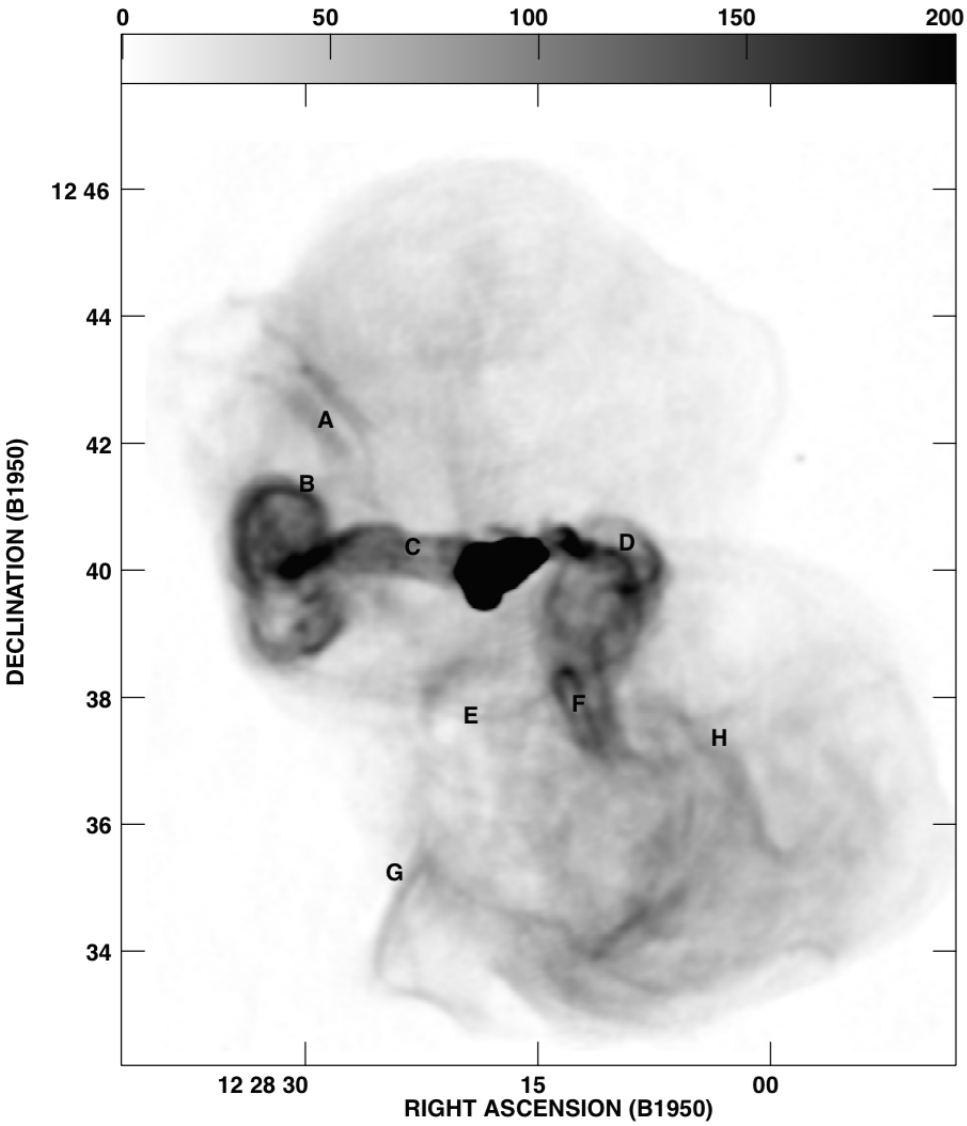

Figure 3.7. *Gray-scale intensity image of M87 (range from 0 to 200 mJy/beam) and the location of minimum pressure analysis regions (Owen et al., 2000).*

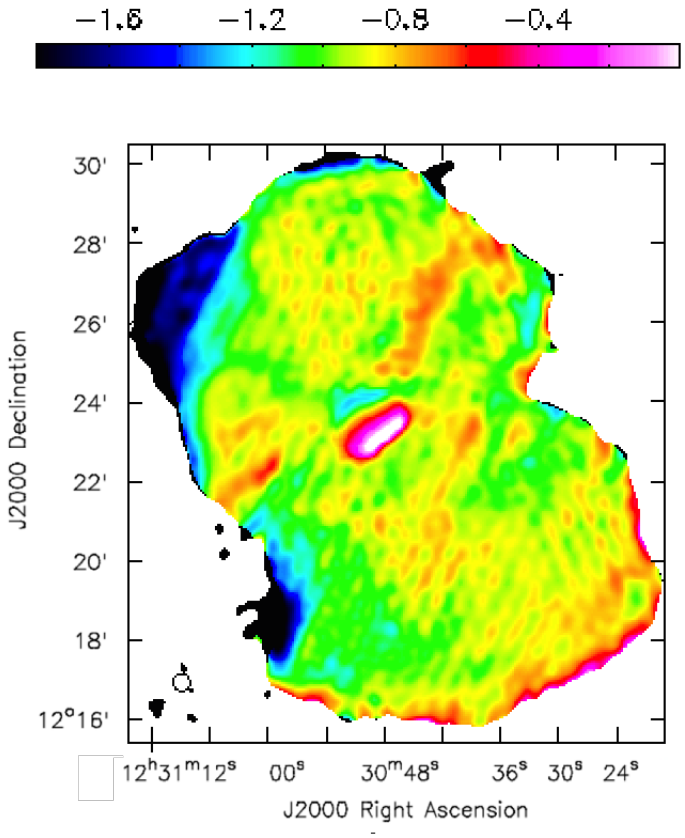

Figure 3.8. *Spectral index map between 327 MHz (90 cm) and 74 MHz (4 m) images. Pixels where the error were above 3σ are blanked. The synthesized beam is shown in the bottom-left corner of the image.*
This map shows the products of a shift in the coordinate systems. The spectral index values in the cocoon should be constant (ranging from 0.55 to 0.6 in the literature; Biretta et al., 1991; De Gasperin et al., 2012), while here there is a gradient in the core. Moreover, in the south-west region there is a wide flattening not consistent with the steepening in the other boundaries.

3.4 Spectral index map

A low-frequency spectral index map of M87 was obtained by combining the 327 MHz image with the 74 MHz image, produced with the same beam and cellsize. The result is shown in figure 3.8.

The spectral index map shows a shift in the coordinate systems. It appears clear from the spectral index values in the cocoon that should be constant (ranging from 0.55 to 0.6 in the literature; Biretta et al., 1991; De Gasperin et al., 2012) and in the south-west region where there is a wide flattening not consistent with the steepening in the other boundaries.
Ionospheric fluctuations can easily affect a map producing shifts of many arcminutes even for sources that have been phase-aligned to a model. In particular, at low frequencies, it can both shift and stretch the map so at times there is no simple linear solution to match the images. This happens because the ionosphere is inhomogeneous and various directions have different

values of refraction indices introducing a phase shift.[9]

Comparing the brightest pixel positions in the images, the 330 MHz image results shifted towards south-west. Using contour lines with respect to the maximum of the emission, it is possible to find a value in right ascension and declination to shift the 330 MHz image coordinate system.
To test the alignment performed by shifting the centroid of the 74MHz one, I realized a cross correlation between the regridded intensity images and the result is shown in figure 3.9.
The maximum value of the correlation is located in (0,0) point, so the re-alignment is correct. The new spectral index map is shown in figure 3.10.

The central cocoon has a spectral index ranging from - 0.6 to - 0.55, consistent with De Gasperin et al. (2012) in the radio band and at higher frequencies up to the optical band (Biretta et al., 1991). A steepening of the spectral index is present at the north-east and south-east edges of the map with values from -1.8 to -0.9, where the emission is weaker, whereas a flattening is visible in some of the flow-active locations, e.g. the east lobe (the "ear" zoomed in fig. 3.11) and the initial part of the west flow. In the southern lobe the spectral index flattens assuming values in the range from -1 to -0.75 where the bright flow twists and bends with respect to the surrounding regions and it is comparable to what is observed in the east lobe in the radio-brightest zones, where α ranges from -1 to -0.8.
Differences between the lobes were also found by Rottmann et al. (1996) at 10 GHz. They observed a higher degree of polarization in the southern lobe due to the Laing-Garrington effect (see section "Relativistic beaming and superluminal motion") and a total flux from the southern lobe that is 20% higher than from the northern one.
The faint extension towards the north-east is the steepest part of the halo, reaching a spectral index of 1.8. Interestingly, this feature is collocated with what Forman et al. (2007) identify as an external cavity in the X-ray halo. Note that the northern halo is related to the counter-jet (that is not directly observable), and therefore farther away from the observer. Moreover, it has the lowest signal-to-noise ratio of the map, therefore it could be affected by spurious features.

[9]Since the refractive index of the atmosphere is not equal to 1, an electromagnetic wave propagating through it will experience a phase change, according to the Snell law. The phase change is related to the refractive index of the air n and the distance traveled D by $\phi = (2\pi/\lambda) \cdot n \cdot D$.

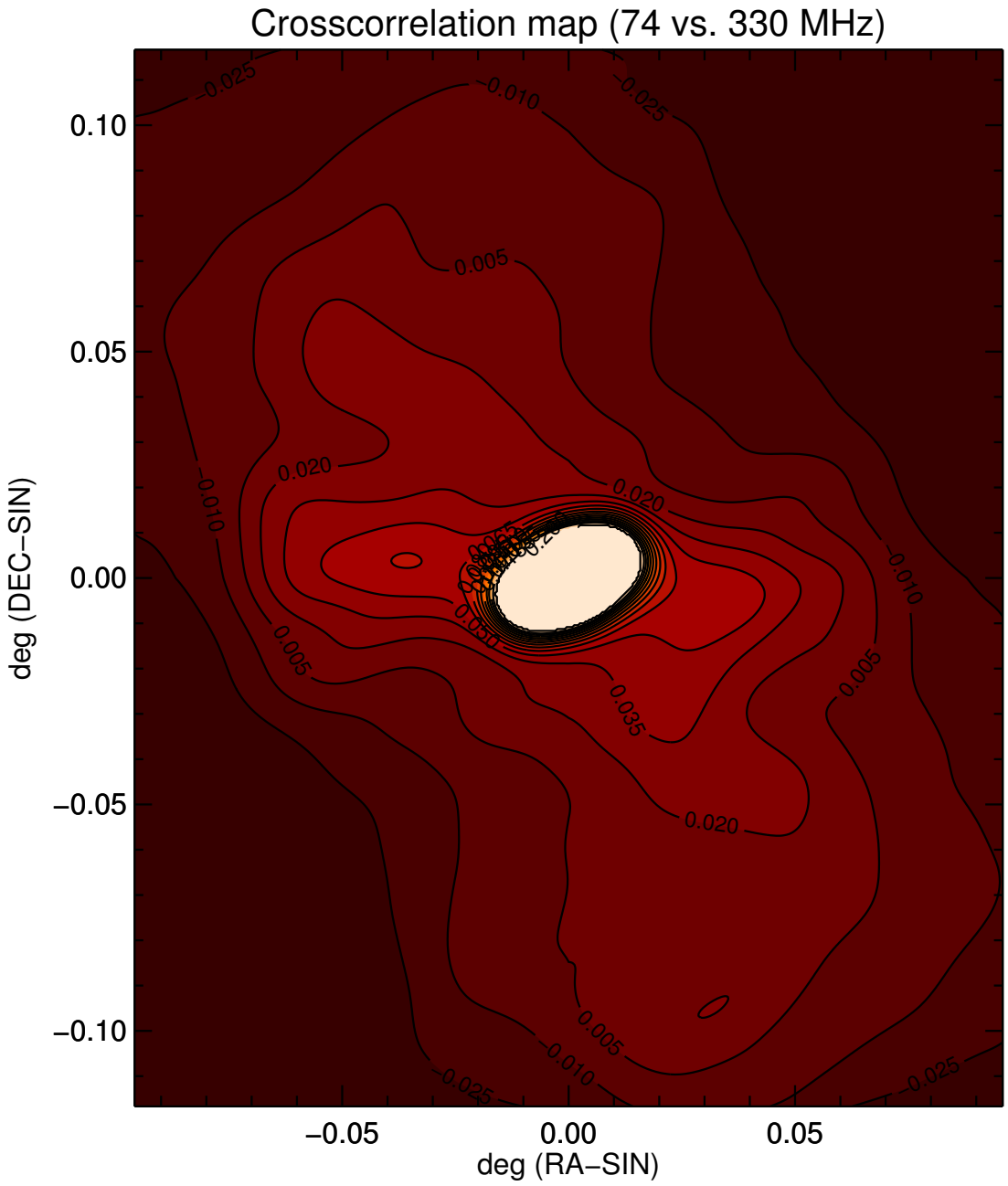

Figure 3.9. *Cross correlation map between the regridded intensity images. The (0,0) point correspond to the equatorial coordinates (J2000) RA 12:30:49.4 DEC +12.23.28. The maximum value of the map is located there, meaning that no shift in the coordinate system is needed to align the intensity images.*

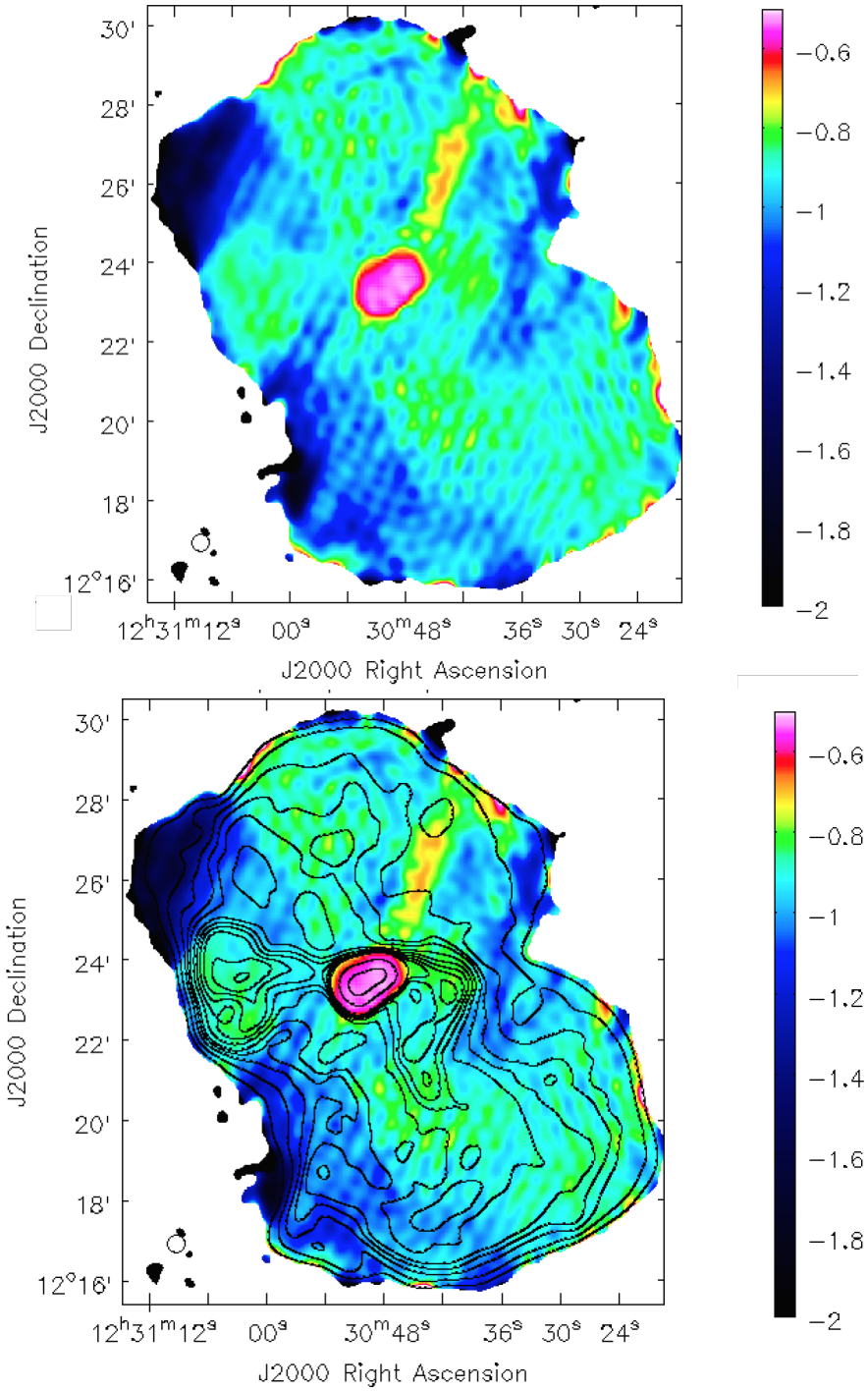

Figure 3.10. Spectral index map between 327 MHz (90 cm) and 74 MHz (4 m) images. Pixels where the error were above 3σ are blanked. a systematic error is present in the form of a sort of honeycomb structure. This is an artifact of deconvolution. At the bottom, the map with contour lines from the 327 MHz at $(1, 2.5, 5, 7.5, 10, 15, 20, 25, 30, 35, 45, 250, 1000)x3\sigma$. The synthesized beam is shown in the bottom-left corner of each image.
The central cocoon has a spectral index ranging from - 0.6 to - 0.55. A steepening of the spectral index is present at the north-east and south-east edges of the map with values from -1.8 to -0.9, where a reduction in the emission is present, whereas a flattening is visible in some of the flow-active locations, like the east lobe. In the southern lobe the spectral index flattens assuming values in the range from -1 to -0.75 where the bright flow twists and bends with respect to the surrounding regions and it is comparable to what is observed in the east lobe in the radio-brightest zones, where α ranges from -1 to -0.8.

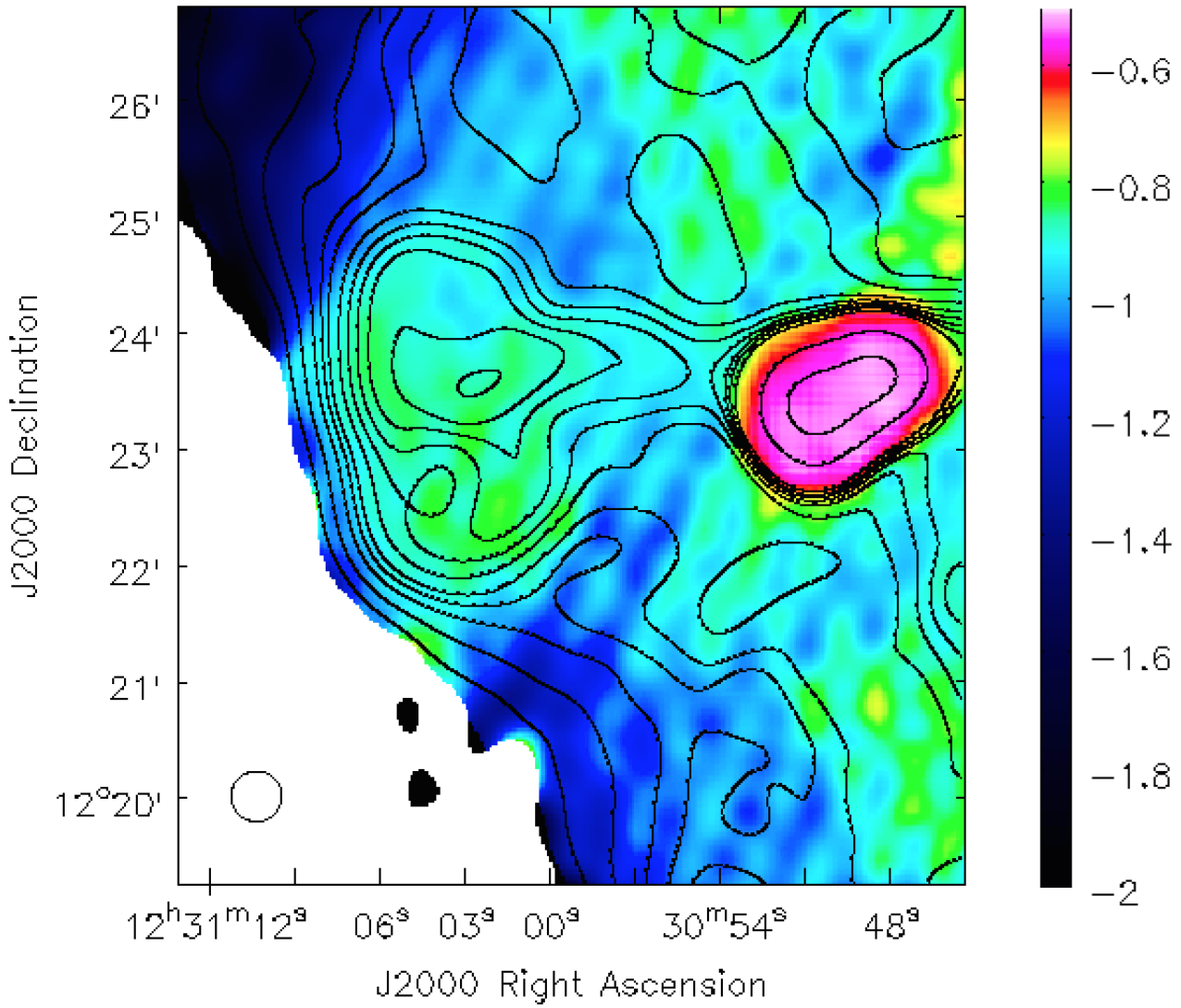

Figure 3.11. *Spectral index error map zoomed in the ear-lobe region. The contour lines are from the 327 MHz at* $(1, 2.5, 5, 7.5, 10, 15, 20, 25, 30, 35, 45, 250, 1000)x3\sigma$. *The synthesized beam is shown in the bottom-left corner of the image.*

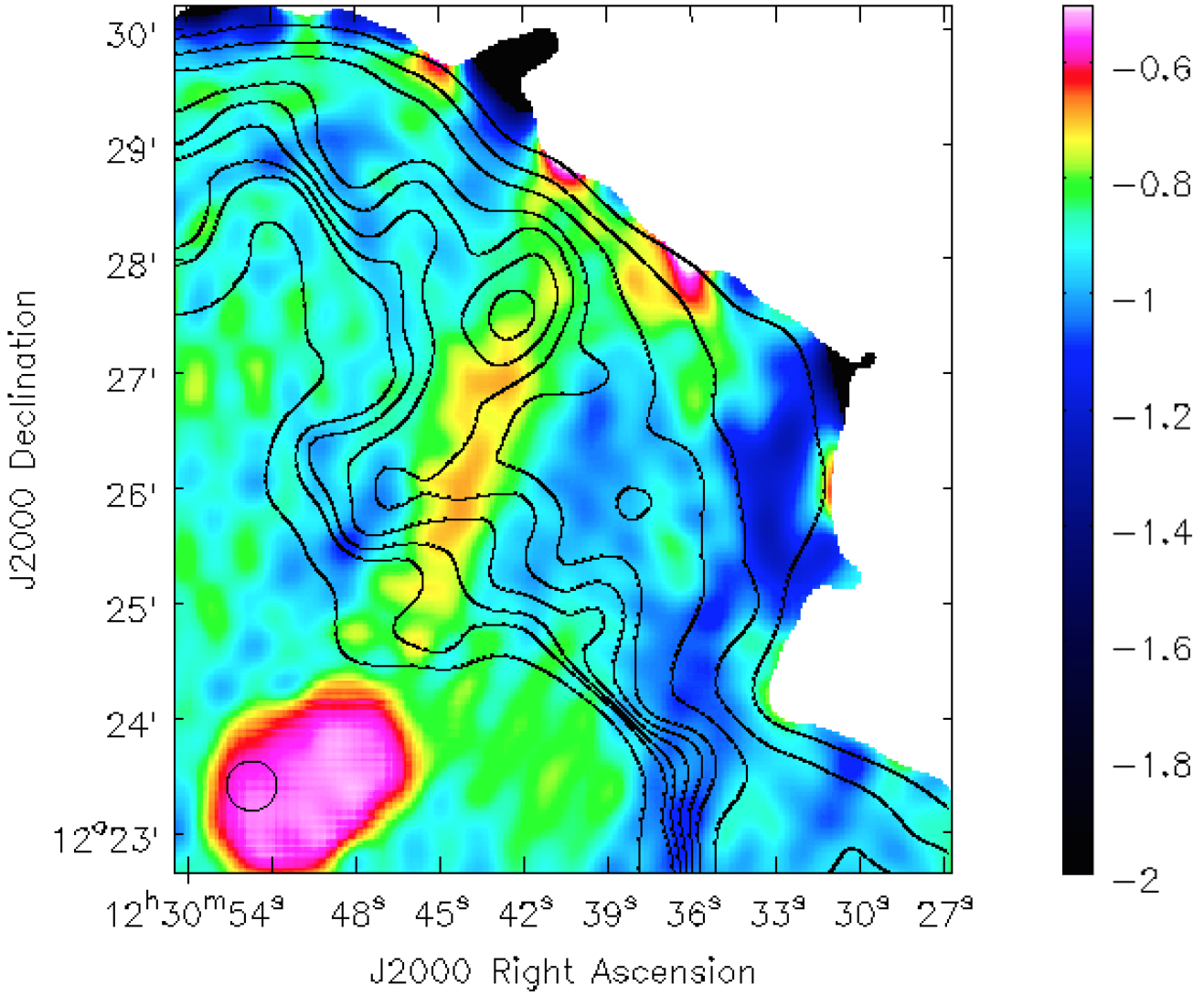

Figure 3.12. *Spectral index map zoomed in the feature region. The contour lines are from the 327 MHz at* $(1, 2, 3, 4, 4.5, 5, 5.5, 6, 8)x3\sigma$. *The synthesized beam is shown in the bottom-left corner of the image.*

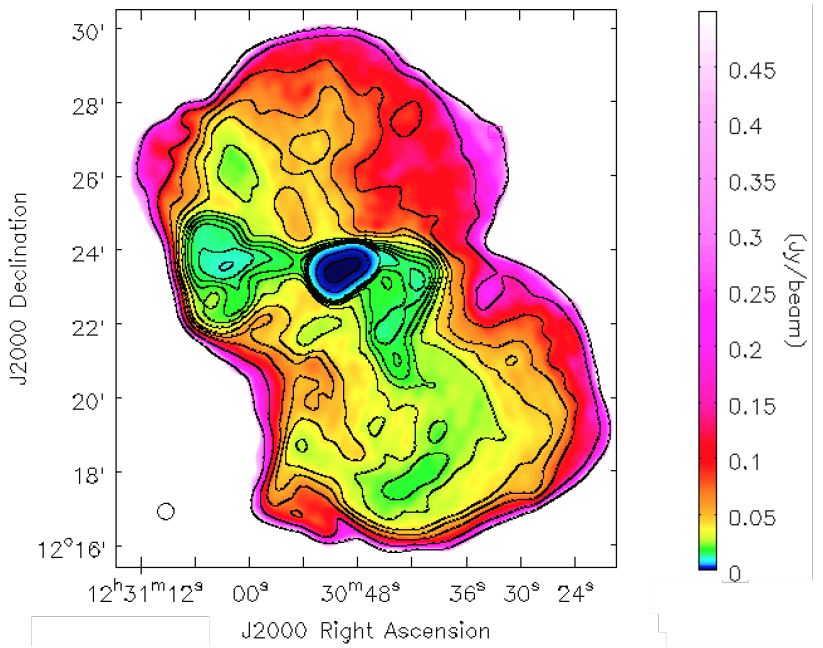

Figure 3.13. Spectral index error map between 327 MHz (90 cm) and 74 MHz (4 m) images. Pixels where the error were above 3σ are blanked. At the bottom, the map with contour lines from the 327 MHz at $(1, 2.5, 5, 7.5, 10, 15, 20, 25, 30, 35, 45, 250, 1000)x3\sigma$. The synthesized beam is shown in the bottom-left corner of each image.

3.5 Spectral index error map

The error on the spectral index is:

$$\Delta\alpha = \frac{1}{log(\frac{\nu_1}{\nu_2})}\Delta log(\frac{S_1}{S_2}) = \frac{1}{log(\frac{\nu_1}{\nu_2})}\sqrt{(\frac{\Delta S_1}{S_1})^2 + (\frac{\Delta S_2}{S_2})^2} \tag{3.28}$$

using the statistical formula $\Delta f = \sqrt{\sum_i (\frac{\partial f}{\partial x_i}\Delta x_i)^2}$ where $f(x_i)$ is a generic function. Considering the two images S_1 and S_2, the relative errors ΔS_1 and ΔS_2 are calculated as rms noise level. The result is presented in figure 3.13 and as expected the error distribution follows the intensity distribution (fig. 3.6). The relative error range is $(0.0004 - 0.5) Jy/beam$.

However, a systematic error is present in the form of a sort of honeycomb structure in the 74 MHz image. This is an artifact of deconvolution and affects the spectral index map with increased systematic errors, above all in the halo diffuse emission.

3.6 The feature

The major result in the spectral index map obtained in this work is the presence of a flattening of the spectral index in the north-west region, as shown in the zoomed image in fig. 3.12. It appears as a nearly linear feature with a length of $\simeq$ 16 kpc. This feature is particularly important because it does not appear in previous spectral index maps. In the LOFAR paper (De Gasperin et al., 2012), a low-frequency spectral index map was obtained combining images in the LBA range (from 45 to 77 MHz) with those in the HBA range (from 115 to 162 MHz) and

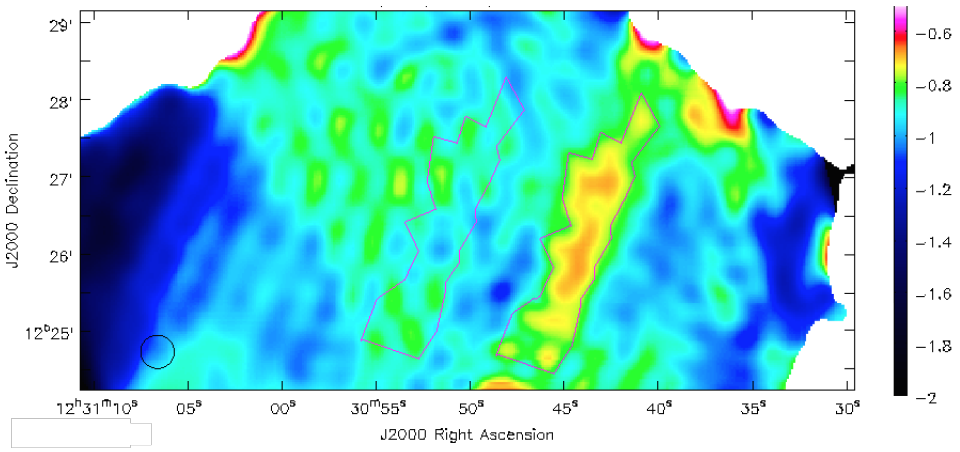

Figure 3.14. *The spectral index map with the irregular region around the feature and a control region surrounding the feature but containing the same area.*

the 327 MHz image, convolving all the images to a resolution of 50 arcsec.
They report a flattening of the spectrum by 20% compared to the rest of the halo in the north-west part of it, asserting that it seems not to be related with any structure in the brightness maps. However, we will show that it is actually related to a low-emissivity region in the 74 MHz image.

By integrating the flux along the length of the feature, it is possible to derive an integrated spectral index with smaller errors. The result can be compared to the integration of a control region surrounding the feature but containing the same area.
The irregular region around the linear feature and the control region are shown in figure 3.14. The first approximately covers the region with $\alpha > -0.8$, whereas the latter is obtained by shifting that irregular region onto the background.
The statistical value for the feature (f) is:

$$\alpha^{f}_{mean} = -0.75 \pm 0.04$$

and the statistical value for the control region (c) is:

$$\alpha^{c}_{mean} = -0.88 \pm 0.04$$

So, $\alpha^{f}_{mean} - \alpha^{c}_{mean} = 0.13$, which is greater than 3σ where σ is the standard deviation of the control region.

Considering $\alpha^{f}_{mean} = -0.75$, the electron energy spectral index p is equal to 2.5, from $\alpha = \frac{1-p}{2}$. Note that the feature region contains the effect of deconvolution errors and low signal- to-noise of the halo emission.

3.7 Minimum energy analysis and synchrotron ages

Synchrotron age, that is the timescale for the radiation by the particle, is highly dependent on magnetic field estimates and the chosen model for the evolution of the energy distribution of

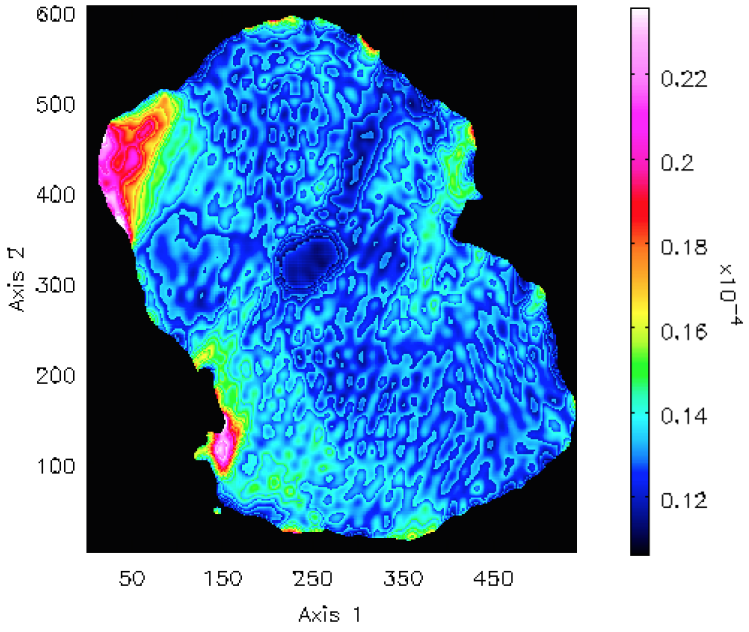

Figure 3.15. *Minimum magnetic field distribution map. The values are expressed in Gauss, therefore the range is* $(10.6 - 23.6)\mu G$. *Note that using discrete values for the function* ξ *for intervals of* α *causes edge effects in the map.*

the ensemble of radiating particles.

The minimum magnetic field can be written as in eq. 3.25.
Tabulated values of $\xi(\alpha, \nu_1, \nu_2)$ are presented for ν_1 = 10 MHz, ν_2 = 10 GHz, for α between -0.4 and - 2 in increments of 0.1, assuming that the spectral index changes by less than 0.1 between 10 MHz and 10 GHz (Govoni & Feretti, 2004).

Considering the 327 MHz intensity image with a conversion from $Jy/beam$ to $mJy/arcsec^2$, a distribution map of the minimum magnetic field can be made with the source brightness values and $\xi(\alpha, 10MHz, 10GHz)$ where α values are from the spectral index map shown in figure 3.10.
The other chosen parameters are k = 1 (which is usually assumed, meaning that the particle energy is equally divided between electrons and protons), z = 0.004 (which is actually irrelevant) and d = 0.12 kpc, considering that 1 arcsec = 81 pc and 1 pixel = 1.5 arcsec (from the image header).
The minimum magnetic field distribution map and the relative histogram are shown in fig. 3.15 and 3.16. The values are in the range $(10.6 - 23.6)\mu$G.
Considering the region selected in fig. 3.7, Owen et al. (2000) show that the magnetic field consistent with the minimum pressure in various parts of the outer halo lie between 7 and $10\mu G$.

To estimate the synchrotron age of the feature using the minimum field values, a mean value for B_{min} is calculated using the same profile around the feature in fig. 3.14: $B^f_{min} = 12\mu$G.
Recalling that

$$t_s[Myr] = 1610\,(B[\mu G])^{-3/2}\,(\nu_b[GHz])^{-1/2}$$

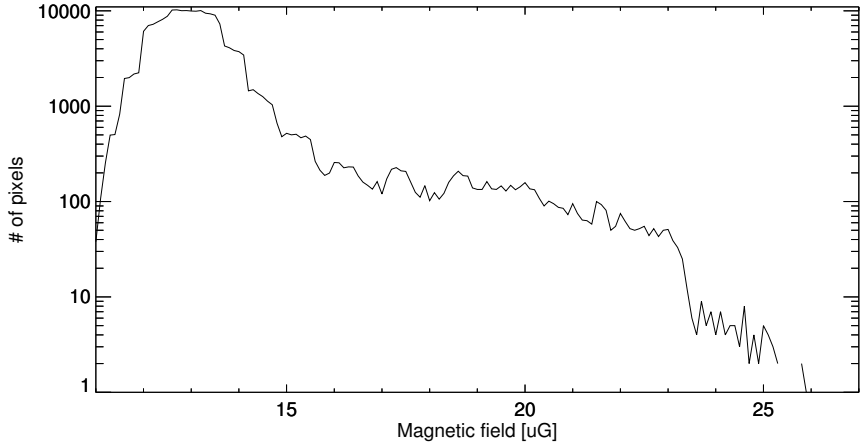

Figure 3.16. *Histogram from the minimum magnetic field distribution map.*

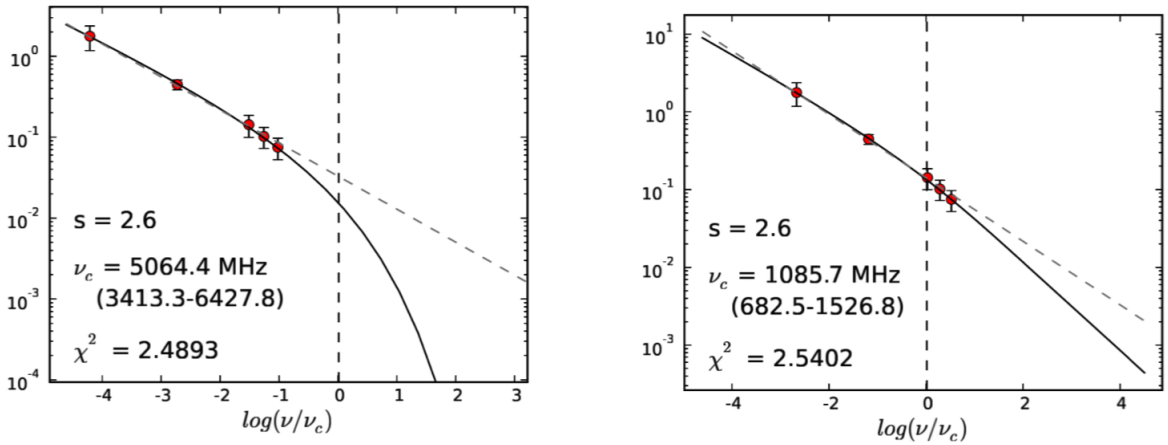

Figure 3.17. *On the left, spectral fit for the initial injection model. On the right, spectral fit for the ongoing injection model (Urvashi, 2010).*

the break frequency is needed.
For p = 2.5, I used the values for ν_b found out by Urvashi (2010) for p = 2.6 (named 's' in her notation), shown in fig.3.17. The data consist of 5 flux measurements between 75 MHz and 1.8 GHz (or 4.8 GHz). For each value of p, a critical frequency that gives the best fit of the data to the model is found, obtaining best-fit solutions for both the initial injection and ongoing injection models. The expected region of spectral turnover is 1 - 10 GHz. Across the range 75 MHz - 1.4 GHz, there is no clear sign of a spectral break or cut-off.
These solutions were obtained for the initial injection as well as ongoing injection models that differs only for form of the source term, as explained in section "Aging and spectral models":

- the initial Injection model for p = 2.6 has $\nu_b \simeq 5GHz$ and $t_s = 17.3\,Myr$;
- the ongoing Injection model for p = 2.6 has $\nu_b \simeq 1GHz$ and $t_s = 38.7\,Myr$.

Note that the ongoing-injection model applies only to regions that are continuously fed by an energy source, or to regions where there is some local form of particle injection. On the other hand, the initial-injection model applies when energetic particles are produced in the jet and the travel outwards in the form of buoyant or expanding bubbles and age via synchrotron

$D(kpc)$	$\rho(10^{-3}cm^{-3})$	$V_{min}(10^8 cm/s)$	$V_{max}(10^8 cm/s)$	$V_{mean}(10^8 cm/s)$
4.1	82.4	3.45	7.68	4.23
8.2	32.6	5.49	12.22	6.73
12.3	18.7	7.25	16.13	8.89
16.4	14.7	8.17	18.19	10.02
20.6	11.3	9.32	20.75	11.43
24.7	9.06	10.41	23.17	12.77
28.8	7.53	11.42	25.42	14.00
32.9	6.56	12.23	27.23	15.00

Table 3.1. The Alfvén velocities corresponding to the following values for the minimum magnetic fields $B_{min} = 10.6\,\mu$ G , $B_{max} = 23.6\,\mu$ G, $B_{mean} = 13\,\mu$ G.
D is the length scale and n_e is the X-ray density values from Nulsen & Böhringer (1995) scaled to the distance of 17 Mpc.

$D(kpc)$	$\tau_{min}(Myr)$	$\tau_{max}(Myr)$	$\tau_{mean}(Myr)$
4.1	1.16	0.52	0.95
8.2	1.46	0.66	1.19
12.3	1.66	0.75	1.35
16.4	1.96	0.88	1.60
20.6	2.16	0.97	1.76
24.7	2.32	1.04	1.89
28.8	2.47	1.11	2.01
32.9	2.63	1.18	2.15

Table 3.2. Alfvén timescales for the Alfvén velocities corresponding to the following values for the minimum magnetic fields $B_{min} = 10.6\mu$ G , $B_{max} = 23.6\mu$ G, $B_{mean} = 13\mu$ G.

radiation with no additional sources of energy.

An other useful estimate for timescale can be obtained calculating the Alfvén time t_A, which the time-scale on which Alfvénic magnetohydrodynamic effects can occur.
Using the X-ray density values from Nulsen & Böhringer (1995) scaled to the distance of 17 Mpc, as in Owen et al. (2000), it is possible to estimated t_A, knowing that:

$$v_A[cm/s] = \frac{10^6\, B[\mu G]}{\sqrt{4\pi\rho[g/cm^{-3}]}}$$

$$t_A = \frac{D}{v_A}$$

where v_A is the Alfvén velocity[10], ρ is the density and D is the length scale.
The results are shown in tab. 3.1 and 3.2 for three values of the minimum magnetic field previously calculated: $B_{min} = 10.6\,\mu$ G , $B_{max} = 23.6\,\mu$ G, $B_{mean} = 13\,\mu$ G.

[10] v_A is the velocity of propagation of Alfvén waves in the direction of the magnetic field

Therefore, the mean Alfvén timescale lies in the range (0.95 - 2.15) Myr. Comparing these values to the estimated synchrotron ages 17.3 Myr and 38.7 Myr, respectively for initial injection and ongoing injection models, the analysis supports an adiabatic expansion of the plasma.

Since the electron diffusion speed is limited by the Alfvén speed, during their lifetimes they can cover distances that are smaller than the observed extension of radio halos. The radial spectral steepening cannot be simply due to aging of radio-emitting electrons.To explain their emission, a mechanism of in situ reacceleration of relativistic electrons has been proposed: MHD turbulence that stochastically accelerates pre-existing electrons through a Fermi process. Therefore, a high frequency cut-off is expected in the synchrotron source spectra because of the low efficiency of this acceleration mechanism. Moreover, turbulence can cause a radial steepening and a complex spatial distribution of the spectral index due to different acceleration processes in different cluster regions and a complex radio halo morphologies due to intermittence of turbulence.
Therefore the spectral steepening observed in radio halos going from the core to the outskirts must be related to the intrinsic evolution of the local electron spectrum and to the radial profile of the magnetic field (Feretti, 2004; Vacca, 2012).

Other estimates of the halo age as dynamical ages:

- if the bubble motion is driven by an energy source, then for an expanding lobe powered by a constant energy source at the center and overpressured with respect to its surroundings, the age of the source can be estimated as the time taken for the outer edge of the lobe to expand to a certain size (volume). The volume of the lobe V(t) is related to the input power, external density and lifetime as $t_{dyn} \simeq 120$ Myr for $\dot{E} \simeq 10^{44} erg/sec$ and $n_X \simeq 0.01$ (Owen et al., 2000).
- if the bubble motion is buoyant, then it rises up through an atmosphere of hot plasma and for a distance of $\simeq 40$ kpc $t_{buoyant} \simeq 40 - 60$ Myr (Churazov et al., 2001).

The overall picture for the extended radio halo dynamic of Virgo A can be describes as a composite of many plasma bubbles. These bubbles are inflated in the central nucleus of M87 by the powerful jets. There, in fact, cavities in the thermal gas are visible.
As soon as they leave the dense core, a strong adiabatic expansion shifts their radio emission towards lower frequencies and lower fluxes. Then they buoyantly rise towards the halo outskirts where they disperse. During their motion, the bubbles lift up cold X-ray emitting gas from the centre of the cluster.

Chapter 4

Discussion

4.1 Multiwavelength comparison

A composite of optical, X-ray and radio images of M87 (fig.4.1) was produced using an X-ray in the keV band (0.5 - 1 keV, Chandra Observatory, NASA/CXC/CfA/W. Forman et al., 2007), the 327 MHz radio image (VLA, Owen et al., 2000); and an optical image (SDSS, 7500 Å).
It is clear that no optical counterpart is found in the region of the radio halo, whereas on the other hand radio and X-ray structures present a correlation.
The apparent correlation between structures seen in the radio and X-ray in the ear-lobe and ear-canal regions suggests some form of local activity that might contribute to the transfer of energy between the radio plasma and the surrounding thermal ICM.

Note that towards north-west in the region of the feature, no optical or X-ray counterparts are visible. Therefore the feature observed in the halo is formed by the radio-emitting plasma.

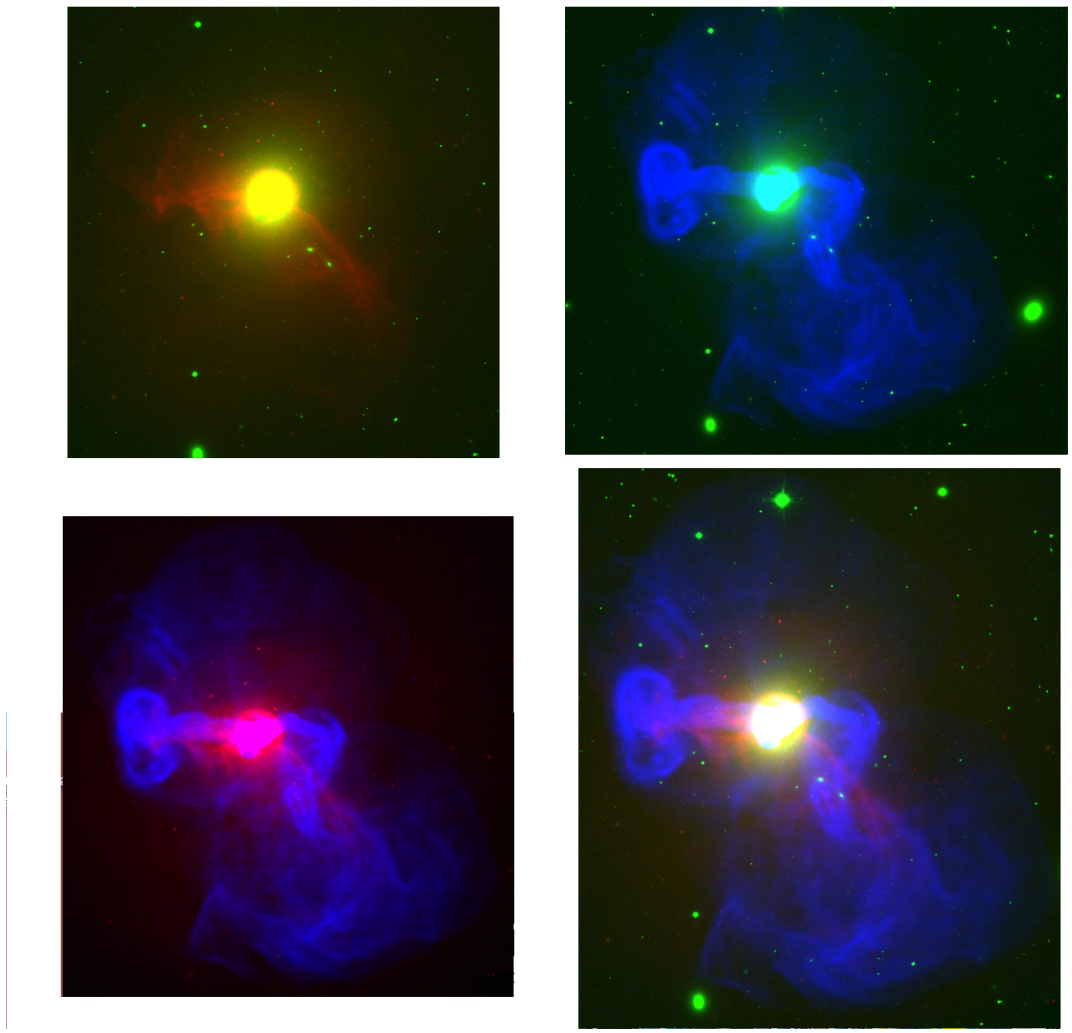

Figure 4.1. *Top left: composite of optical (green) and X-ray (red) images of the M87.*
Top right: composite of optical (green) and radio (blue) images of the M87.
Bottom left: composite of radio (blue) and X-ray (red) images of the M87.
Bottom right: composite of optical (green), radio (blue) and X-ray (red) images of the M87.
Credits: X-ray NASA/CXC/CfA/W. Forman et al. (broadband keV); radio NRAO VLA Owen (90 cm); Optical: SDSS (7500 Å)

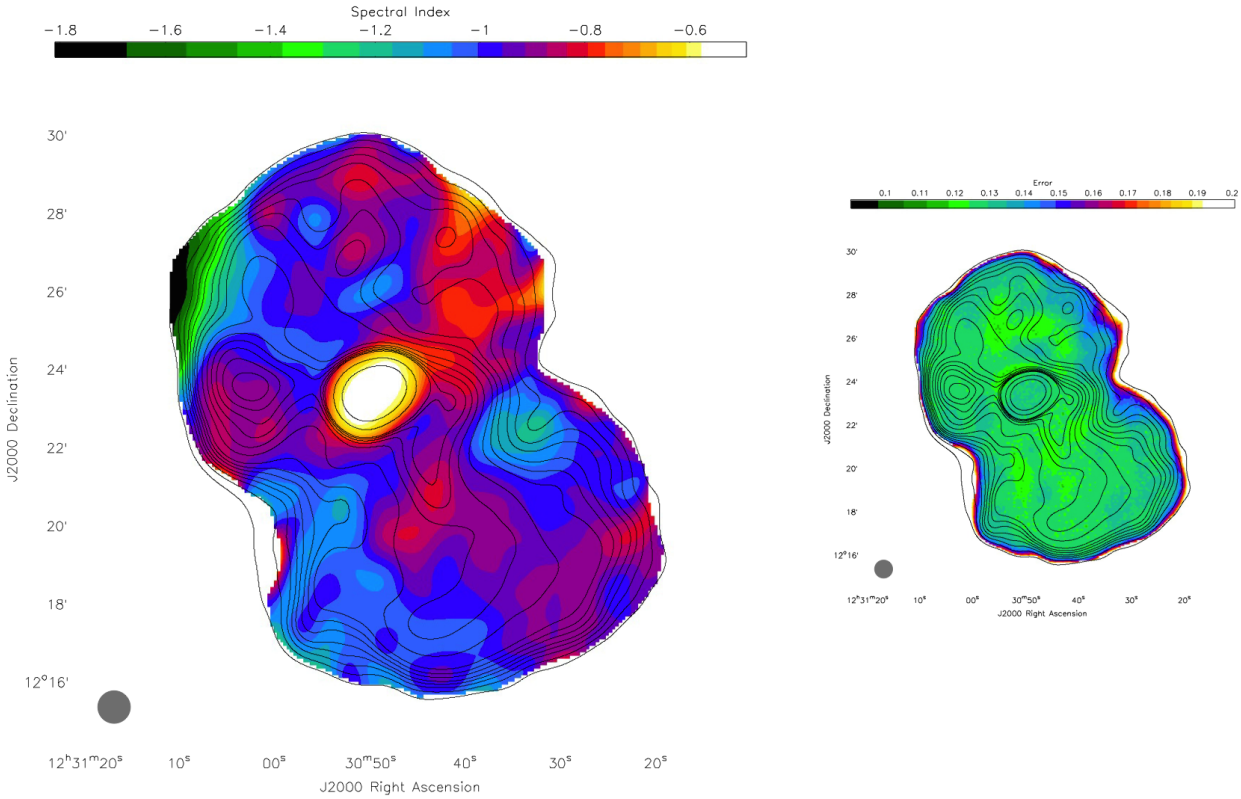

Figure 4.2. *Low-frequency spectral index map obtained from LOFAR-LBA (45 – 71 MHz only) and LOFAR-HBA (115 – 162 MHz) observations, together with VLA map at 325 MHz. Contour lines are from the 325 MHz map. On the right: spectral index 1σ error map. (de Gasperin et al., 2012)*

4.2 Comparison

The spectral index map obtained in this work can be compared to the LOFAR one's (De Gasperin et al., 2012). They used an averaged image in the HBA frequency range (115 – 162 MHz, with 50 arcsec resolution) and one in the LBA frequency range (45 – 77 MHz, with 50 arcsec resolution) obtained with the LOFAR instrumentation. Then, a low-frequency spectral index map (fig.4.2) was obtained by superposing those two images and using the VLA image at 327 MHz (convolved at the same resolution of 50 arcsec) and calculating the spectral index for each pixel using a linear regression.
Therefore, they present in addition to the images of this work a frequency range that is intermediate between 74 MHz and 327 MHz. They observe a flattening in the north-west part of the map, but it does not clearly appear as a linear feature and the flattening is more diffuse. However, they averaged several images in the LBA and HBA range and the resolution is lower.

They do not discuss any possible interpretation: "Although in the lowest signal-to-noise zone of the map, we report a flattening of the spectrum by 20% compared to the rest of the halo in the north-west part of it. This feature seems not to be related with any structure in the brightness maps. [...] A low-frequency spectral index map of Virgo A shows no obvious relation between spectral index and brightness. A flattening of the spectral index, instead, is visible at the northern lobe towards west and in the position of enhanced radio flux density." (De

Gasperin et al., 2012).

By courtesy of De Gasperin, it was possible to calculated directly the mean value of spectral index from the map presented in De Gasperin et al. (2012) and shown here in fig.4.3. With the same profile around the feature used on the map in fig. 3.14, the LOFAR mean value in the region of the feature is:

$$\alpha^{f}_{mean-LOFAR} = -0.82 \pm 0.05$$

and the statistical value for the control region (c) is:

$$\alpha^{c}_{mean-LOFAR} = -0.95 \pm 0.06$$

Recalling the value for the feature in the map obtained in this work:

$$\alpha^{f}_{mean} = -0.75 \pm 0.04$$

$$\alpha^{c}_{mean} = -0.88 \pm 0.04$$

Therefore, it can be concluded that the flattening is of the same order going to the background to the feature region. However, the instrument has different bandpass and the curvature of the spectrum can be different at different frequencies.

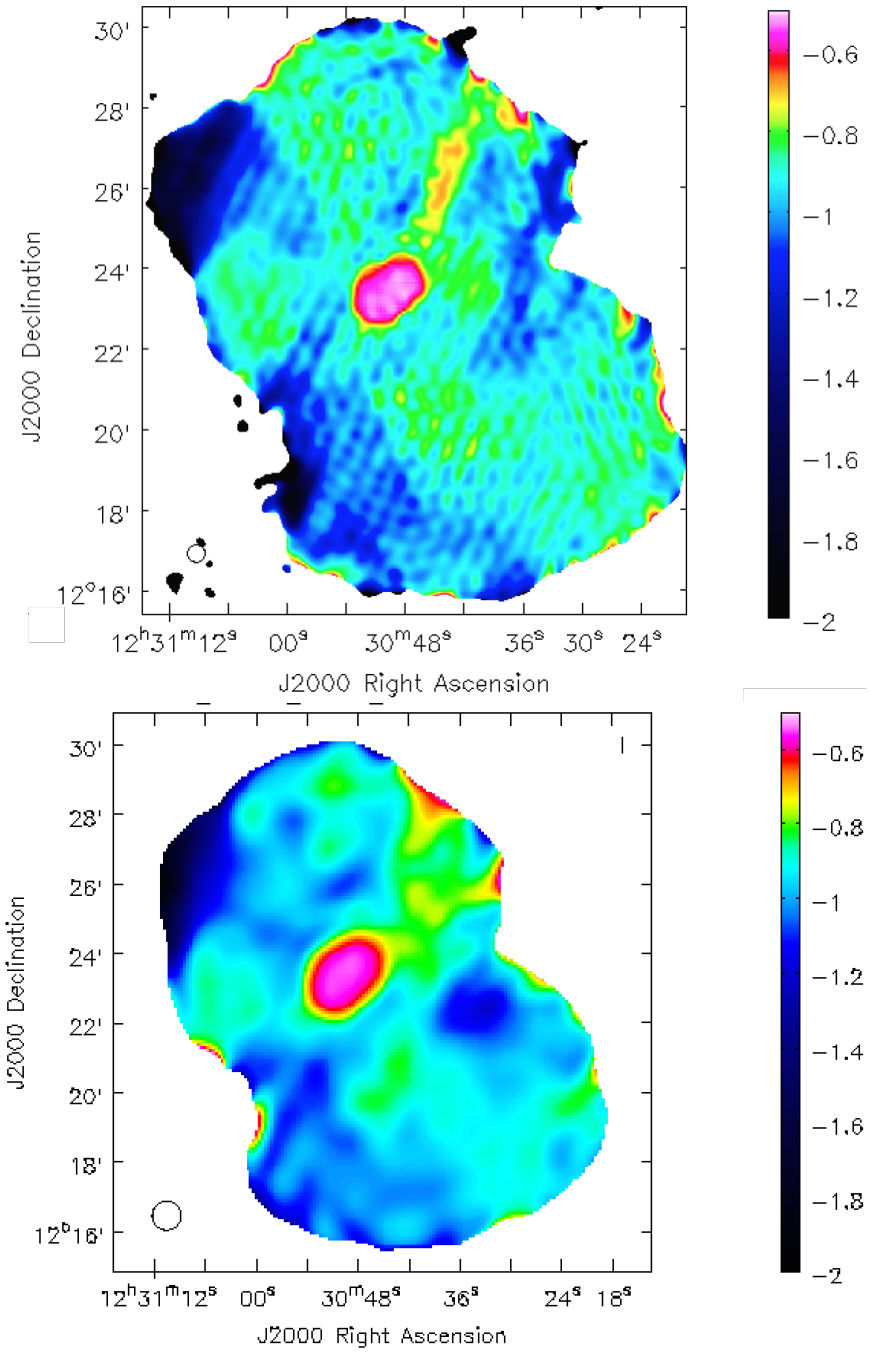

Figure 4.3. Spectral index map between 327 MHz (90 cm) and 74 MHz (4 m) images with a range from -2 to -0.5. Pixels where the error were above 3σ are blanked. A systematic error is present in the form of a sort of honeycomb structure. This is an artifact of deconvolution. The LOFAR spectral index map (by courtesy of De Gasperin) presented in fig. 4.2 but with the same range and scale of the map obtained in this work.

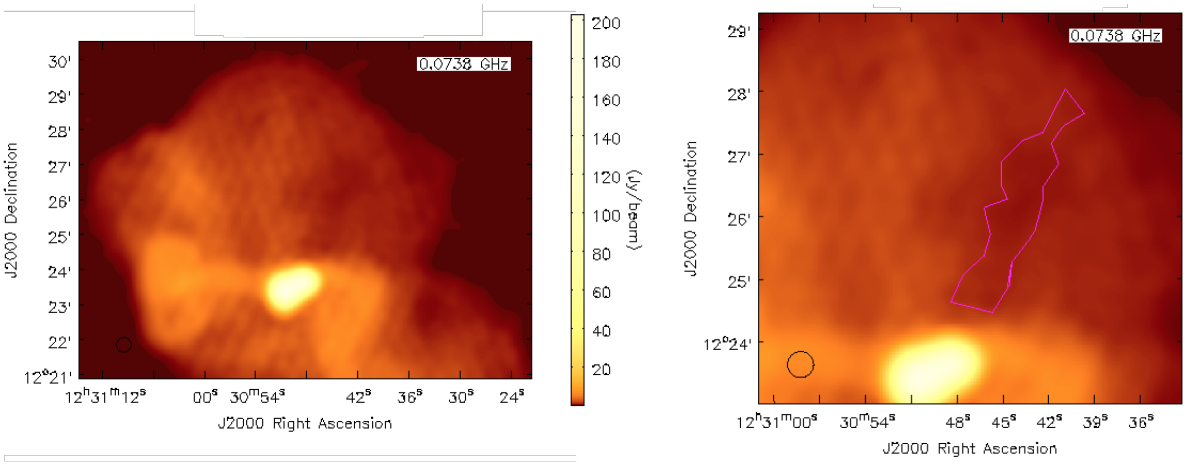

Figure 4.4. *On the left, the 74 MHz image zoomed in the region of the feature from the spectral index map (fig.3.12). On the right, the same image with the irregular region around the feature chosen in fig. 3.14.*

4.3 The feature interpretation

The feature found in the spectral index map corresponds to a region in the 74 MHz image characterized by the lowest emission of intensity, as it is possible to see in the images in fig. 4.4.
Superposing the same irregular profile chosen in fig. 3.14 on the 74 MHz image in the region corresponding to the feature, a mean value of intensity is 0.81 $Jy/beam$. The mean value in the surrounding halo is 1.45 $Jy/beam$.

A minimum in the radio emission could mean that the particles on the feature region are aging trapped in a region with a low magnetic field.
The synchrotron source is optically thin everywhere so another explanation has to be sought for why there is a flattening of the spectral index. Any loss mechanism increases α. Only injection, e.g. reconnection, provides an effective injection mechanism, and this must be local (i.e. within a single filamentary structure). The jet cannot account for the low index since it shows a steeper spectrum than the feature. Further, any relic from the jet or lobes will equally show *at least* as high a spectral index as the jet and core from propagation. We are left with only one simple option, that the magnetic field and relativistic particle density are both lower in the feature – and in its less prominent counterpart on the opposite side of the lobes – than elsewhere in the radio halo. Two specific physical conditions favor this explanation. One is that the emissivity in the feature is lower than the rest of the lobe. The other is the relative confinement of the feature within the overall tangle of field and emission regions. Aging is easily included in the propagation equation (eq. B12, Eilek & Shore 1989). Note that the energy density is low and the structure is far from the nucleus so the radiation energy density is also. All particles will undergo inverse Compton losses. But that means if there is a difference it is attributable to the local field. A highly tangled, homogeneous, space-filling turbulent magnetic field will produce pitch angle scattering throughout its length. In this case, however, a weak ordered field B_0 provides a guiding center for the streaming electrons that will radiate efficiently once they reach the outer lobes, for which the magnetic energy (entirely

concentrated in knots and filaments) is about the same but the field configuration is random. Hence, for much of the lobe volume, the minimum energy argument applies. For the low field strength regions, while a value for the (volume averaged) magnetic field energy density will be about the same as the jet, the tangled structure is closer to the conditions required for the argument to be valid.

4.4 Aging model

Standard aging models assumes that the particles are well mixed in a uniform magnetic field. However, magnetic fields in synchrotron sources are almost certainly inhomogeneous, mixing high-field and low-field regions. In the M87 case, in fact, the halo region appears inhomogeneous with a plasma highly filamented.
This inhomogeneity affects the evolution of the electron distribution due to the rate of energy loss changing as electrons move between regions of different magnetic field strengths (Eilek, Melrose & Walker, 1997). Let consider the halo plasma containing regions that are distinguished by the strength of the magnetic field: a high-field region and a low-field region. The regions of high magnetic field, which could be the filaments, are separated by low magnetic field regions. If a relativistic electron spends much of its life in a low-field region, and then moves into a high-field region in which it can radiate efficiently, on average it loses energy more slowly than if it were continuously in the high-field region. Thus the source looks younger than it is, as could be the case of the feature characterized by a synchrotron age lower than 40 Myr.
The finite thickness L of the interfaces between the high- and low-field regions is important when assuming the particles initially or continually injected into the low-field region, slowly propagating into the high-field region. The propagation across field lines is probably diffusive in nature. So a diffusion coefficient D and its timescale $\tau = L^2/4D$ play a role.
Therefore, a given relativistic particle spends only a fraction of its time in the high-field region but its synchrotron losses are important only while it is in the high-field region.

4.5 Conclusion

M87 is a large elliptical galaxy hosting an active nucleus and one of the first identified radio sources, called Virgo A. In fact, it lives at the center of Virgo cluster that is the nearest cluster of galaxies, giving the possibility to study one of the most clear examples of AGN-cluster interaction.
Most radio galaxies at similar power are supported by jets that remain collimated until 100 kpc. However, the M87 jet is collimated for only a few kiloparsecs, disrupting close to the galactic center. The interaction with the ICM creates the large-scale radio structure of M87, known as the halo, which show a complex radio emission formed by flows from the M87 nucleus that extends well beyond the inner region containing the jet.
The halo region is inhomogeneous with a highly filamented radio-loud plasma. These regions could present high magnetic field strength, high relativistic particle density, or both, whereas the interfilament regions could simply be low-field, or low particle density, regions. Alternatively, they could be regions dominated by thermal plasma from the cluster atmosphere.
In general, during their lifetime, relativistic particles cross a wide range of magnetic field strengths, experiencing different aging. As a result, the final particle spectral distribution will be a sum of spectra with many break frequencies. In fact, particles that have spent much of their life within strong magnetic fields will have a very low break frequency, which can modify the low-frequency slope of the radio spectrum.

Two intensity maps of Virgo A are presented in this thesis: a VLA image at 327 MHz (90 cm, P band; F. Owen) with 7 arcsec resolution and a VLA image at 74 MHz (4 m, 4 band; N. Kassim) with 25 arcsec resolution. These images well resolve the structure of the radio halo, showing a bright compact region of emission on top of a relatively faint diffuse background.
Assuming that $F_\nu \propto \nu^\alpha$, a low-frequency spectral index map was then obtained by combining the 327 MHz image with the 74 MHz image, produced with the same beam. This map shows values for α in the range from -2 to -0.5, in agreement with what found by De Gasperin et al. (2012).
The central cocoon has a spectral index ranging from - 0.6 to - 0.55, whereas a steepening of the spectral index is present at the north-east and south-east edges of the map with values from -1.8 to -0.9, where a reduction in the emission is present. A flattening is visible in some of the flow-active locations, but the major result in the spectral index map obtained in this work is the presence of a flattening of the spectral index in the north-west region. It appears as a sort of linear feature with a mean spectral index of -0.75 ± 0.04. This feature is particularly important because it does not appear so clearly in previous spectral index maps. In the LOFAR paper, they just observe a flattening in the north-west part of the map, but it does not appear as a linear feature and the flattening is more diffuse.
Being aware that the feature region contains the effect of deconvolution errors and is a low signal-to-noise region of the halo emission, it corresponds to a a region in the 74 MHz image characterized by the lowest emission of intensity. A minimum in the radio emission could mean that the particles on the feature region are aging trapped in a region with a low magnetic field where electrons live longer. In fact, if a relativistic electron spends much of its life in a low-field region, and then moves into a high-field region in which it can radiate efficiently, on average it loses energy more slowly than if it were continuously in the high-field region.

Thus the region looks younger than it is, as could be the case of the feature characterized by a synchrotron age lower than 40 Myr (for both particle injection models), calculated using minimum energy estimate for the magnetic field realized on the 327 MHz image and break frequencies from Urvashi (2010).
In the equipartition analysis, an average magnetic field strength of 12μG was found in the feature region, while a magnetic field of 30μG is present in the inner cocoon (De Gasperin et al., 2012).
The Alfvén timescale estimate gives a value of $\simeq$ 2 Myr for a particle to reach the halo boundaries. Therefore, the dynamic can be described as adiabatic expansion.

Studying the low radio frequency emission of the M87 halo, from 330 MHz down to 25 MHz, the source appears well confined within boundaries that are identical at all frequencies.
Observations at these frequencies should enable us to probe older populations of electrons, recalling that the characteristic frequency at which an electron emits synchrotron radiation [1] is $\nu_b = B^{-3} \cdot t^{-2}$. Those are expected to accumulate at lower energies, which would imply a low-frequency spectral steepening.

However, low-frequency observations of Virgo A, as the maps here presented in addition to the ones from Owen et al. (2000) and de Gasperin et al. (2012), do not reveal a previously hidden spectral steepening toward low frequencies and show the extended radio halo to be well confined within boundaries. Moreover, the low-frequency halo spectrum outside the central region is considerably steeper (in general with α < - 0.8, except for the feature region) with respect to the core region. Simple synchrotron aging would have left untouched the low-frequency part of the spectrum.
As suggested by Murgia et al. (1999) and de Gasperin et al. (2012), the most probable explanation of this steepening at low frequencies is strong adiabatic expansion of the plasma bubbles that happens as soon as they leave the dense central region. This occurs in combination with a superposition of differently synchrotron-aged electron populations. Adiabatic expansion of the relativistic plasma will shift the spectra towards lower frequencies down to the MHz region and lower intensities, therefore can also affect the low-frequency end of the spectrum.
What is certain is that the gas is expanding into the surrounding cluster gas and not flowing inward as proposed in the cooling flow model. In fact, the halo is expanding outward into the cluster gas thanks to a continuing energy input from the jet. It can be described as a bubble, with a well-defined outer boundary that separates the internal, radio-loud plasma from the external, thermal cluster gas with approximate pressure balance between them (Owen et al., 2000).

The gas clouds out of which galaxies and clusters form were heated by the energy released during their initial gravitational collapse. Some of the gas then cooled to form the objects that can be observed. The gas particles in the hot atmosphere in the central cluster region lose much of their thermal energy to X-ray bremsstrahlung radiation. In the core of a cluster, in fact, the atmosphere is naturally densest, therefore the radiative cooling time due to the emission of the observed X-rays is shortest there.This time in general is significantly shorter than

[1] assuming the strong-field limit for which inverse Compton cooling is negligible.

the Hubble time, therefore if no additional heating mechanism is present, the gas cools and is expected to flow inwards, forming a cooling flow (Fabian, 1994). In fact, when cooling reduces the gas temperature, the gas density must rise in order to maintain the pressure therefore the diffuse radiating gas must flow towards to the center of cluster forming a pressure-driven flow.
However, the cooling rate in some clusters is in reality much smaller than what expected. In these cases, there is the possibility that the gas is prevented from cooling by some heating mechanism, like the presence of an AGN with powerful jets.
Some fraction of the jet energy could go to turbulence or bulk flows, while the rest could go to heating. The heat will directly drive an outward expansion of the gas into the cooler, lower pressure gas sitting above it. Therefore, competing processes like heating, radiative cooling, expansion and turbulence play a role. This can be the overall picture for M87, sitting in the center of a cluster.
In fact, measurements of the jet power suggest that the active nucleus plays a significant role in reheating the intra-cluster medium preventing cooling below a certain temperature. However, the mechanism by which this feedback may be occuring is not well understood.
Feedback processes and timescales for the Virgo cluster can be studied by modeling the formation and evolution of various features in the M87 radio halo. Ages of the observed radio halo estimated from models of bouyant or driven bubbles are an order of magnitude smaller than the expected cooling time. So, mechanical energy transport alone is not enough. However, observations of X-ray emission show possible correlations with some features in the observed M87 radio halo, suggesting that these are sites of possible energy transfer between the radio plasma and the thermal ICM.

More intensity images of M87 are needed for future works at frequencies lower than 74 MHz, as new LOFAR radio telescope can do. This would be useful to check the presence of the flat feature in the north-west part of the halo. Moreover, the filamentary structure can be studied in more detail to understand its nature.
Also to ultimately draw conclusions the AGN and the surrounding medium, further analyses will be useful. New LOFAR and VLA observations are necessary to provide the higher angular resolution (less than 5 arcsec) maps of the Virgo A halo ever obtained and a continuum coverage from 30 MHz up to 8 GHz, thanks also to single dish observations as possible with the Green Bank Telescope (GBT, fully steerable 100m radio telescope in West Virginia, USA).With this information it will be possible to study the many interesting phenomena that occur in M87.

Appendix A

Radio Interferometry technique

A.1 Angular resolution

The main great advantage of radio interferometry is the large improvement of resolution. From diffraction theory, it is well-known that the image resolution for an aperture of diameter D at wavelength λ has a diffraction limit equal to $\theta(rad) \simeq \frac{\lambda}{D}$ or $\theta(arcsec) \simeq 2\,\lambda(cm)/D(km)$ in practical units.
The resolution of a large optical telescope is limited to $\simeq 0.5$ arcsec by atmospheric fluctuations (seeing), although the diffraction limit is much smaller.
Because of the longer wavelengths, radio telescopes have fuzzier vision than optical telescopes. For a single dish antenna, the angular resolution is:

$$\theta(rad) = k\,\frac{\lambda}{D} \tag{A.1}$$

where k is a factor of order unity that depends on details of antenna illumination (Wilson, Rohlfs & H$'$uttermeister, 2009).
The point is that to improve angular resolution the diameter D must be increased (for a given wavelength). However, practical issues, such as tracking accuracy and deformations, limit the size of a single dish telescope.
Using as example Effelsberg 100 m radio telescope near Bonn, which is one of the currently largest single, fully-steerable aperture, the angular resolution at 21 cm (HI line) is 420 arcsec. In this case, to obtain a resolution equal to 1 arcsec typical of the optical band, the diameter should be $\simeq 42$ km. A single dish of this size would collapse under its own weight.

Michelson was the first to show that a better resolution, necessary for extragalactic radio sources [1], could be obtained coherently combining the output of two reflectors both of diameter D separated by a distance $b \gg D$.
Then, the first radio interferometers were used in the late 1940's and interferometry was developed in order to synthesize an equivalent aperture through summations of separated pairs of antennas, laying the groundwork for the aperture synthesis method, formulated by Ryle and Hewish in 1960.
Using this approach, a remarkable improvement in radio astronomical imaging was possible.

[1] The majority of extragalactic radio sources are smaller than 1 arcmin.

At centimeter wavelengths, and increasingly in the millimeter region as well, using an array of telescopes for aperture synthesis is now the rule.
Note that the contribution and variation of the radio sky do not affect the observations, therefore there is no need to subtract them as occurs in the visible wavelengths. However, radio telescopes can suffer interference of terrestrial origin and from strong radio sources in other parts of the sky.

A.2 The two-element interferometer

An image of a distant source is formed when electromagnetic radiation from the source passes through an aperture of finite size and falls on a screen that can save the information about the intensity of the incident radiation. The aperture can be a lens as well as an antenna.
To measure the power of the radiation field produced along a set of directions covering different parts of the source, the latter needs to be spatially incoherent: the radiation produced by one part of the source is not correlated with that from any other part of the source.
So images of a distant radio source can be made by measuring the mutual coherence function of the electric fields at pairs of points in a plan normal to the direction of the source. This requires basic concepts of wave interference and Fourier transforms.
The mutual coherence function describes the cross correlation of the radiation field at two given points. This has the dimension of power and can be easily measured using two element interferometers through sequential measurements with different baselines.

In the single dish case, the power response of a single uniformly illuminated aperture has a main beam and sidelobes, whereas in the interferometer case, for instance two small antennas separated first by a distance b and then by a distance 2b, there are fringes centered about zero due to the correlation of the antennas' output and the sidelobe level does not decrease with increasing angular offset from the axes of the antennas. This analysis led to the downside that for a given spacing only a source structure comparable to, or smaller than, a fringe is fully recorded.
Note that by doubling the separation of the antennas, the fringe width is halved. This means that for larger antennas distance, the interferometer angular resolution is greater. Moreover, if the shortest distance between any pair of small telescopes is b_{min}, then sources that cover an angle on the sky larger than λ/b_{min} will hardly be detected at all.
Therefore, the fundamental parameter here becomes the distance between two antennas: the baseline $\vec{b}$, which defines the direction and separation of the antennas.
In an interferometer array of N antennas, the total number of baselines is $N(N-1)/2$ and the image resolution is then given by the maximum baseline b_{max}:

$$\theta(rad) \simeq \frac{\lambda}{b_{max}} \tag{A.2}$$

Note that the field of view of the primary beam is still $\theta \simeq \frac{\lambda}{D}$, so increasing D, finer and finer source structure can be measured. Each dish of diameter D receives radiation only from a patch on the sky which is λ/D across; this limits the region we can map with each pointing of the synthesis array.
In conclusion, this technique allows better resolution but not a better sensitivity. In fact, the

synthesized telescope has a collecting area smaller than a filled single dish of the same diameter would have; thus, mapping faint sources can require longer expositions.

However, combining the outputs of independent data sets for different baselines allows to analyze different structural components of the source and finer structure can be recorded if more antennas are added. The current method in radioastronomy to obtain high quality images is the aperture synthesis.
In the 1980s, arrays such as the VLA were built. These are interferometers whose individual antennas are connected in real time by cables, optical fibers or microwave links.
However, in order to go beyond these results and gain more in resolution, a way to increase the baseline was required. The antennas must have been spaced of about thousands of kilometers, therefore the Very Long Baseline Interferometer (VLBI) was born. In VLBI, the antennas have such large separations that real time links are difficult. Currently, the link is achieved by precise timing, with data and time recorded at each antenna. Producing fringes requires aligning the data recorded at each antenna using the time signals and additional software techniques. [2]

Let now consider the most simple interferometer in order to seek basic relations between the characteristics of the product of signals from two separated antennas and the distribution of the source brightness.
Some simplifications are necessary:

- emission in the far field;
- sinusoidal signals (quasi-monochromatic radiation);
- no distortions during propagation due to the earth's atmosphere;
- idealized electronics (no receiver noise or instrumental effects);
- antennas sensitive only to the same state of polarization.

The two-element interferometer, as shown in fig. A.1, is a system of identical antennas, separated by a vector distance $\vec{b}$, that are receiving signals from the unit vector $\vec{s}$, which specify the direction of the source. The extra time taken for the signal to reach the more distant antenna, called geometric time delay, is $\tau_g = \frac{\vec{b}\cdot\vec{s}}{c}$ and the corresponding phase is $\phi = \omega\tau_g = \frac{2\pi\vec{b}\cdot\vec{s}}{\lambda}$.
The coherence function is measured by correlating the outputs of two antennas:

$$V_1 = v_1\, cos[\omega(t-\tau_g)] \qquad V_2 = v_2\, cos(\omega t) \tag{A.3}$$

Then, in the correlator step the signals are input to a multiplying device followed by a time average operation. After removing rapid oscillations, the result is the mutual coherence function of the received wave, therefore a fringe pattern.
The average product $r_C(\tau_g)$ is dependent on the receiver power ($\propto v_1\, v_2$) and geometric delay, hence on the baseline orientation and source direction:

$$r_C(\tau_g) = v_1 v_2 cos(\omega\tau_g) = v_1 v_2\, cos(2\pi\frac{\vec{b}\cdot\vec{s}}{\lambda})$$

[2] There is progress in using near real-time links via internet connections, however. This technique is known as e-VLBI.

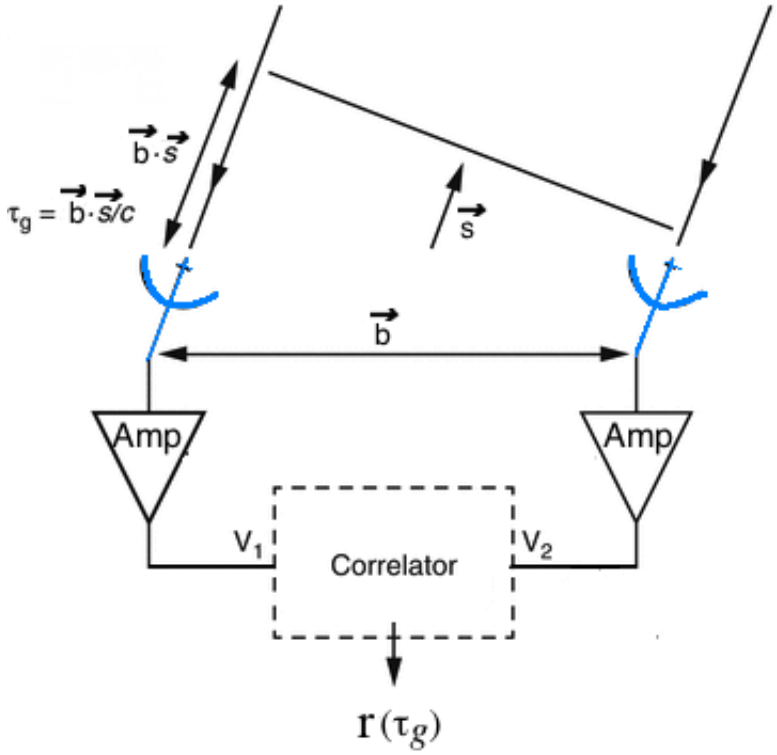

Figure A.1. *Schematic diagram of a stationary quasi monochromatic two-element interferometer.*

Note that $r_C(\tau_g)$ is not a a function of the time of the observation, the physical location of the baseline [3], the actual phase of the incoming signal and the distance of the source. On the other hand, the product is dependent on the antenna collecting areas and electronic gains but these factors can be calibrated for.

If the relative orientation of interferometer baseline $\vec{b}$ and wave propagation direction $\vec{s}$ remain invariable, τ_g remains constant, so does $r_C(\tau_g)$. But since $\vec{s}$ is slowly changing due to the rotation of the Earth, τ_g will vary, and we will measure interference fringes as a function of time. The signal varies slowly as the Earth rotates, changing the angle ωt and giving a large number of baselines at a range of angles, even with only a few dishes.
This simple interferometer can distinguish sources separated only by an angle $\lambda/(bsin(\omega t))$, having the resolution of a large single dish of diameter $bsin(\omega t)$. Note that the two-element interferometer cannot measure the source's position, therefore more telescopes with different baselines are added.
The response from an extended source, treated as the sum of independent point sources, is obtained by summing the responses at each antenna to all the emission over the sky, multiplying the two, and averaging:

$$r_C(\tau_g) = \langle \int V_1 d\Omega_1 \times \int V_2 d\Omega_2 \rangle \tag{A.4}$$

Average and integral operations can be interchanged and, providing spatially incoherent emission, the response becomes:

[3] The physical location of the baseline is unimportant because the source is in the far field.

$$r_C(\tau_g) = \int I(s)\, cos(2\pi \frac{\vec{b}\cdot\vec{s}}{\lambda}) \mathrm{d}\Omega \tag{A.5}$$

This expression links what the observer needs, that is source brightness on the sky I(s), to something that can be measured, that is the interferometer response $r_C(\tau_g)$.

The problem is that one correlator is not enough since the integration of the cosine response over the source brightness is sensitive to only the even part of the brightness. Therefore, to recover the odd part of the brightness, it is possible to replace the cosinus with the sinus in the integral:

$$r_S(\tau_g) = v_1 v_2 sin(\omega \tau_g) \tag{A.6}$$

obtaining the odd fringe pattern. This is implemented by a second correlator with a 90 degree phase shift in one of the signal paths that generates the sine pattern. The combination of cosine and sine correlators is called a complex correlator. In fact, it is now time to define a complex function, called visibility V, from the two independent, real correlator outputs $r_C(\tau_g)$ and $r_S(\tau_g)$:

$$V = r_C(\tau_g) - i\, r_S(\tau_g) = Ae^{-i\phi} \tag{A.7}$$

and recalling that $e^{ix} = cosx + isenx$, by separating the real and imaginary parts of V,

$$Acos\phi = \int I(s) cos(2\pi \frac{\vec{b}\cdot\vec{s}}{\lambda}) \mathrm{d}\Omega \qquad\qquad Asen\phi = -\int I(s) sen(2\pi \frac{\vec{b}\cdot\vec{s}}{\lambda}) \mathrm{d}\Omega \tag{A.8}$$

a useful relationship between the source brightness and the response of an interferometer can be obtained:

$$V(\vec{b}) = r_C(\tau_g) - i\, r_S(\tau_g) = \int I(s) e^{-i\, 2\pi \frac{\vec{b}\cdot\vec{s}}{\lambda}} \mathrm{d}\Omega \tag{A.9}$$

This is a 2D Fourier transform that gives a well established way to recover $I(s)$ from $V(\vec{b})$. The point is to derive the intensity distribution of a part of the radio sky from the measurement of the visibility function using the Fourier transform tool.
In other words, the visibility is the spatial coherence function, that is a measure of the coherence of the electric fields and the term was first used in interferometry by Michelson (1890) to express the relative amplitude of the optical fringes that he observed. As used in radioastronomy, it is a complex quantity: its amplitude [4] gives info about the flux and its phase about the position of the source.
In conclusion, the visibility is a unique function of the source brightness, also referred to as intensity and measured in $Wm^{-2}Hz^{-1}sr^{-1}$ and these two functions are related through a Fourier transform.
Note that the intensity is a real function whereas the visibility is complex and Hermitian.

A two-element interferometer is sensitive only to one Fourier component of the sky brightness distribution, thus more components are required in order to improve the response. This imply

[4] the visibility's amplitude has the dimensions of spectral power flux ($Wm^{-2}Hz^{-1}$)

the need of more baselines, knowing that even the most elaborate interferometer with N antennas can be treated as N (N - 1)/2 independent interferometer pairs. Moreover, it is possible to use the Earth's rotation to vary the projected baseline coverage: this is the Earth-rotation aperture synthesis.

A.3 Interferometers

Now, a convenient coordinate system must be introduced for the two vectorial quantities $\vec{b}$ and $\vec{s}$ to describe the antenna positions and baselines.
Let (u,v,w) be the coordinate axes, measured in units of the wavelength.
The unit direction vector $\vec{s}$ is defined by its projections (l,m,n) on the (u,v,w) axes. The $\vec{s}$ components are called the direction cosines.

$$l = cos\alpha \qquad m = cos\beta \qquad n = cos\theta = \sqrt{1 - l^2 - m^2} \quad \longrightarrow \quad d\Omega = \frac{dl\, dm}{\sqrt{1 - l^2 - m^2}}$$

where α, β and θ are the angles are between the direction vector and the three axes.
It is useful to begin with a special case: an interferometer whose antennas all lie on a single plane. In a two-dimensional measurement plane, the measurements of V(b) are entirely on the plane containing the antennas and normal to the direction of the source, therefore the axis w (for convention) is taken normal to that plane.
Then the components of the baseline vector and of the unit direction vector are respectively:

$$\vec{b} = (\lambda u, \lambda v, \lambda w) = (\lambda u, \lambda v, 0) \qquad \vec{s} = (l, m, n) = (l, m, \sqrt{1 - l^2 - m^2})$$

An interferometer, at any one time, makes one measure of the visibility at baseline coordinate (u,v).
Knowing that

$$\frac{\vec{b} \cdot \vec{s}}{\lambda} = u\, l + v\, m + w\, n = u\, l + v\, m$$

the visibility becomes:

$$V(u, v) = \int\int \frac{I(l, m)}{\sqrt{1 - l^2 - m^2}} e^{-i\, 2\pi (ul + vm)} \mathrm{d}l \mathrm{d}m \tag{A.10}$$

which is a 2-dimensional Fourier transform (often indicated with $\overset{F}{\rightarrow}$, $\mathcal{F}$ or FT) between the projected brightness and the visibility and so, inverting it,

$$I(l, m) = cos(\theta) \int\int V(u, v) e^{i\, 2\pi (ul + vm)} \mathrm{d}u \mathrm{d}v \tag{A.11}$$

In physical optics, this is known as the Van Cittert-Zernicke theorem, which is based on the fundamental relation

$$V(u, v) \overset{F}{\rightarrow} I(l, m)$$

.
The Earth's rotation causes a two-dimensional array, whose baselines are not confined to an east-west line, to fill a three-dimensional volume. Therefore, a nearly coplanar arrays, such as the VLA, cannot use the 2D geometry previously described.

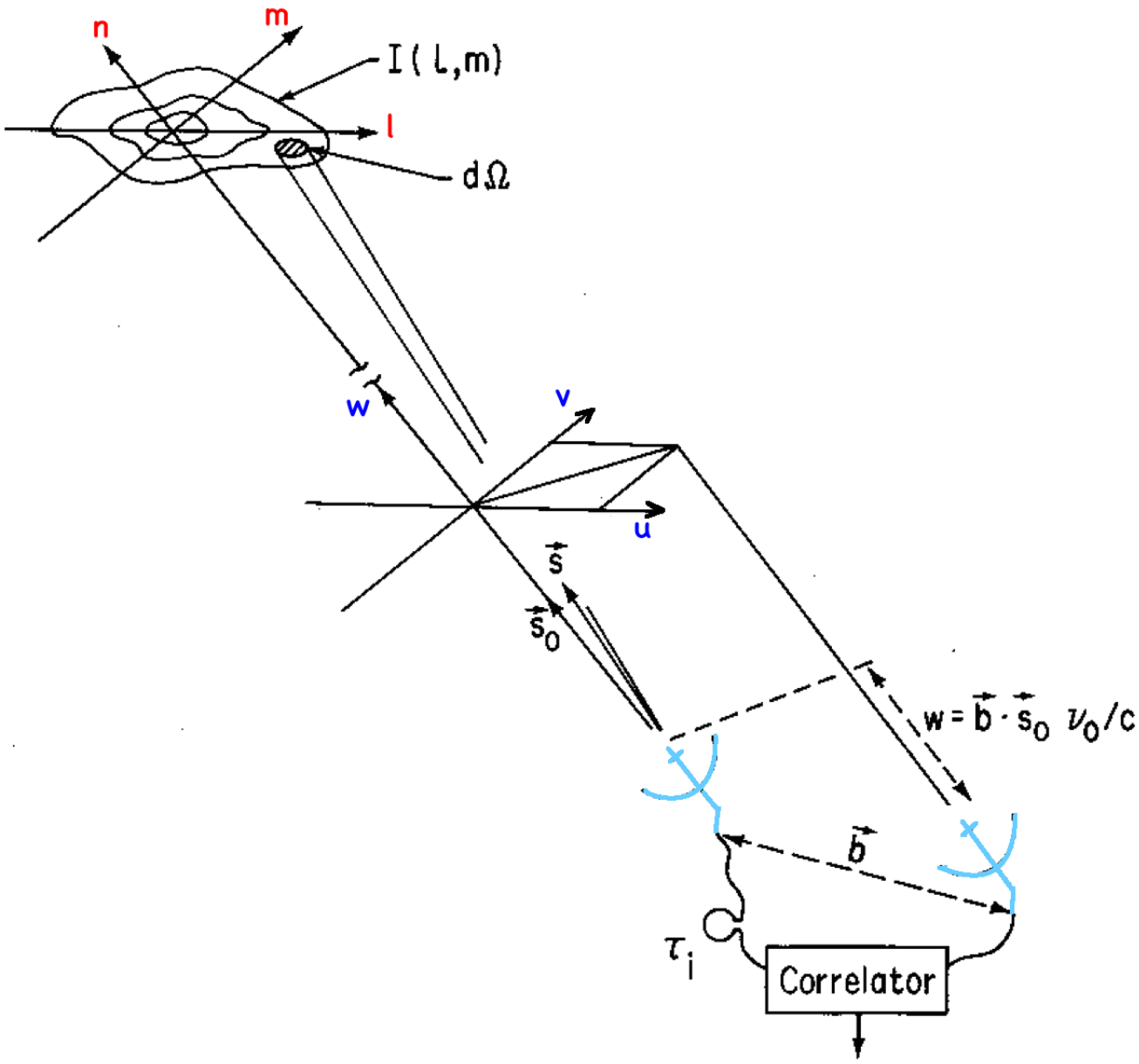

Figure A.2. *The (u,v,w) coordinate system and the direction cosines (l,m,n). (Taylor, Carilli & Perley, 1999)*

In this case, since the plane of the array is rotating with respect to the source, a more general geometry, where all three baseline components are present, must be adopted. This is the coordinate system in most general use for synthesis imaging with 3D interferometers: w points to the region of interest following the source, u towards the east, and v towards the north celestial pole. The direction cosines l and m then increase to the east and north, respectively. Note that the u-v plane always perpendicular to direction to the source.

The visibility in the 3D generalized system becomes:

$$V(u,v,w) = \int\int \frac{I(l,m)}{\sqrt{1-l^2-m^2}} e^{-i\,2\pi(ul+vm+wn)} \mathrm{d}l\mathrm{d}m = \int\int \frac{I(l,m)}{\sqrt{1-l^2-m^2}} e^{-i\,2\pi[ul+vm+w(\sqrt{1-l^2-m^2}-1)]} \mathrm{d}l\mathrm{d}m \tag{A.12}$$

The expression is still not a proper Fourier transform, but if the third term in the phase factor is sufficient small, it can be again a 2D Fourier transform [5].
That condition is met when only a small region of the sky is mapped, hence:

$$w[1-\sqrt{1-l^2-m^2}] = w(1-cos\theta) \simeq \frac{w\theta^2}{2} \ll 1 \tag{A.13}$$

Therefore if the third term in the phase can be neglected, then the relation between the intensity and the visibility again becomes the following 2D Fourier transform:

$$V(u,v) = \int\int I(l,m) e^{-i\,2\pi(ul+vm)} \mathrm{d}l\mathrm{d}m \tag{A.14}$$

and, inverting it:

$$I(l,m) = \int\int V(u,v) e^{i\,2\pi(ul+vm)} \mathrm{d}u\mathrm{d}v \tag{A.15}$$

In conclusion, V(u,v) is the complex visibility function, which is the 2D Fourier transform of the sky brightness distribution I(l,m) for incoherent sources in a far field and with a small field of view. V(u,v) is expressed as (real, imaginary) or (amplitude, phase). The real part of the visibility function is the amplitude that tells "how much" of a certain spatial frequency, whereas the imaginary part is the phase that tells "where" this spatial frequency component is located.
Remember that the baseline coordinates (u,v) are E-W and N-S spatial frequencies measured in wavelengths and the sky coordinates (l,m) are E-W and N-S angles in the tangent plane measured in radians.
Note that each V(u,v) contains information on I(l,m) everywhere, not just at a given (l,m) coordinate or within a particular subregion.
For a complete analysis, see Taylor, Carilli & Perley (1999); Thompson, Moran & Swenson (2001) and Wilson, Rohlfs & H$'$uttemeister (2009).

A.3.1 Coverage of the uv plane

An array of antennas measures only certain values in the set of continous u-v in the visibility function: this is the sampling function S(u,v).

[5] Beware that eq. A.12 is not a three-dimensional Fourier transform!

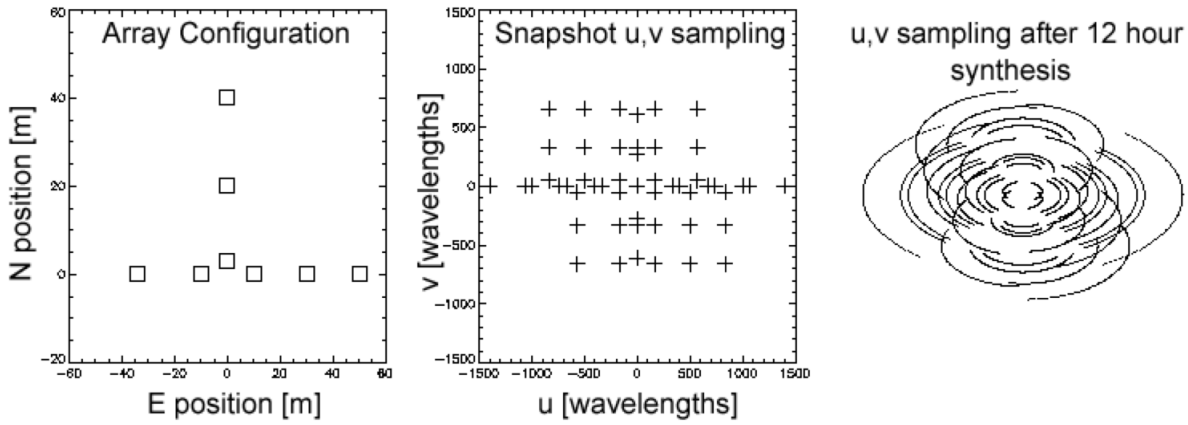

Figure A.3. *a) An example array configuration consisting of 8 antennas, with E and N antenna locations in meters. b) The u,v sampling that results from this array for a single time (snapshot), at zero hour angle. Each cross represents a baseline. There are N(N-1)/2 = 28 unique baselines, but there are twice this many points due to symmetry. c) The u,v sampling that results after a 12 hour integration. The rotating Earth causes the projected baselines to change with time, tracing out portions of elliptical paths.*

Obtaining a good image of a source requires adequate sampling (coverage) of the u-v plane. As seen from the source, the dishes move around each other in elliptical tracks as the Earth rotates. In twelve hours, a map of a source is synthesized as it would be seen by a large elliptical telescope.
If the interferometer has more than two dishes, the u-v coverage becomes a number of concentric ellipses with the same shape.
For every sky brightness distribution there exists a visibility function, that is everywhere a continuos complex function.
The sampled visibility function $S(u,v) \cdot V(u,v)$ is the actual data provided by the array and its inverse Fourier transform gives the dirty image $I_D(l,m)$:

$$I_D(l,m) = \int\int S(u,v) \cdot V(u,v) e^{i\,2\pi(ul+vm)} \mathrm{d}u\mathrm{d}v \tag{A.16}$$

The dirty image does not contain full information about the sky brightness distribution because the sampled visibility presents missing spacings that need to be recovered through an image reconstruction technique.
Using the convolution theorem, the dirty image can be written as the convolution of the the Fourier inversion $\mathcal{F}^{-1}S(u,v)V(u,v)$. The Fourier inversion of the sampling function B(l,m) = $\mathcal{F}^{-1}\{S(u,v)\}$ is known as dirty beam or diffraction pattern of the aperture. In optical systems, where an analog technique is used, this is called PSF (point-spread function) of a telescope. The fundamental relation is clearly explained by images in fig.A.4 and can be expressed as follow:

$$I_D = \mathcal{F}^{-1}\{S(u,v) \cdot V(u,v)\} = \mathcal{F}^{-1}\{S(u,v)\} * \mathcal{F}^{-1}\{V(u,v)\} = B(l,m) * I(l,m) \tag{A.17}$$

Therefore, to obtain the dirty image it is necessary to invert the sampled visibilities. Then, through algorithms of cleaning, the image is restored and the final high quality image is obtained.

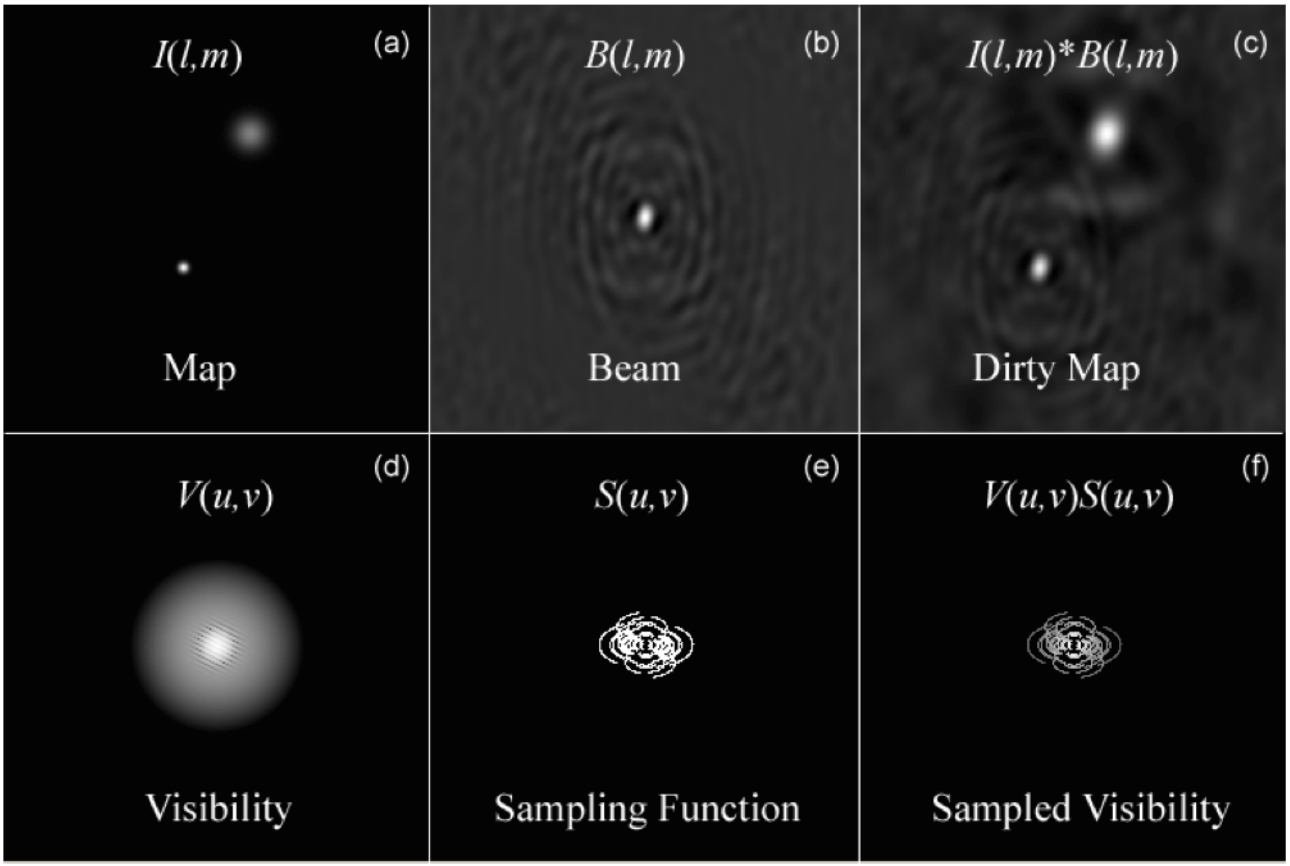

Figure A.4. *The upper row are the sky plane representations of map, beam, and dirty map. The lower row are the corresponding u-v plane representations of visibility, sampling function, and sampled visibility.*
a) An example (model) sky map.
b) The synthesized beam, or point-spread-function, of a model antenna array.
c) The dirty map that results from the FT of the sampled visibilities. This is the same as the convolution of the map in a) and the synthesized beam in b). This is the actual image made by an array.
d) The visibilities corresponding to the map, in other word the FT of a).
e) The sampling function of the array, whose FT gives the beam in b).
f) The sampled visibilities obtained by product of d) and e). These are the actual measurements made by an array.
There are standard image reconstruction techniques that essentially try to predict the missing visibilities in panel d), to arrive at the true map a).

A.3.2 The CLEAN algorithm

Knowing that the sampling is never complete, a deconvolution process is needed to reconstruct the fully sampled map equivalent of the otherwise partially sampled (dirty) (u,v) plane and make a clean image compatible with the sky intensity distribution.
Note that deconvolution is always a non linear process and requires to impose some constrains to better select plausible solutions. The standard deconvolution technique is the CLEAN algorithm, invented by Högbom in 1974 and later developed by Clark (1980) and Cotton and Schwab (1984). It relies on qualitative constrains assuming that the sky brightness is a collection of point sources and the convolution relation $I_D = I * B$ must be valid.

It operates many iterations of a process in which a small amount of the dirty beam is subtracted centered at the highest remaining point in the dirty image. The basic CLEAN algorithm steps can be described as follow (fig. A.5):

1. a residual map is initialized to the dirty map and a clean component list to an empty value;

2. the pixel that assume the maximum value of intensity (I_{max}) is identified in the residual map as a point source (delta function);

3. a fraction of this highest peak, known as "loop gain" g, is added to the clean component list, then convolved with the dirty beam and subtracted from the residual map;

4. this point source amplitude and location are added to the clean component list and then subtracted from the residual map;

5. iteration of the process from point 2 while a stopping criterion is not matched. There are different criterions for stopping the algorithm as reaching the maximum number of clean components or choosing the value of I_{max} less than a fraction of noise or less than a fraction of the dirty map maximum value;

6. the clean component list is convolved by a properly chosen clean beam (restoration step);

7. finally, the result is added to the residual map to obtain the clean map.

The CLEAN algorithm has a number of free parameters:

- the loop gain, which controls the convergence of the method. A good result is when $g \simeq (0.1 - 0.3)$, depending on sidelobe levels, source structure and dynamic range;

- the threshold for convergence and the number of iterations, which define to which accuracy the deconvolution proceeds. It is common practice to clean down to about the noise level or slightly below; however, in case of strong sources, the residuals may be dominated by dynamic range limitations;

- the clean beam in the restoration step, which is usually a 2D Gaussian to allow a simple Fourier transform deconvolution.

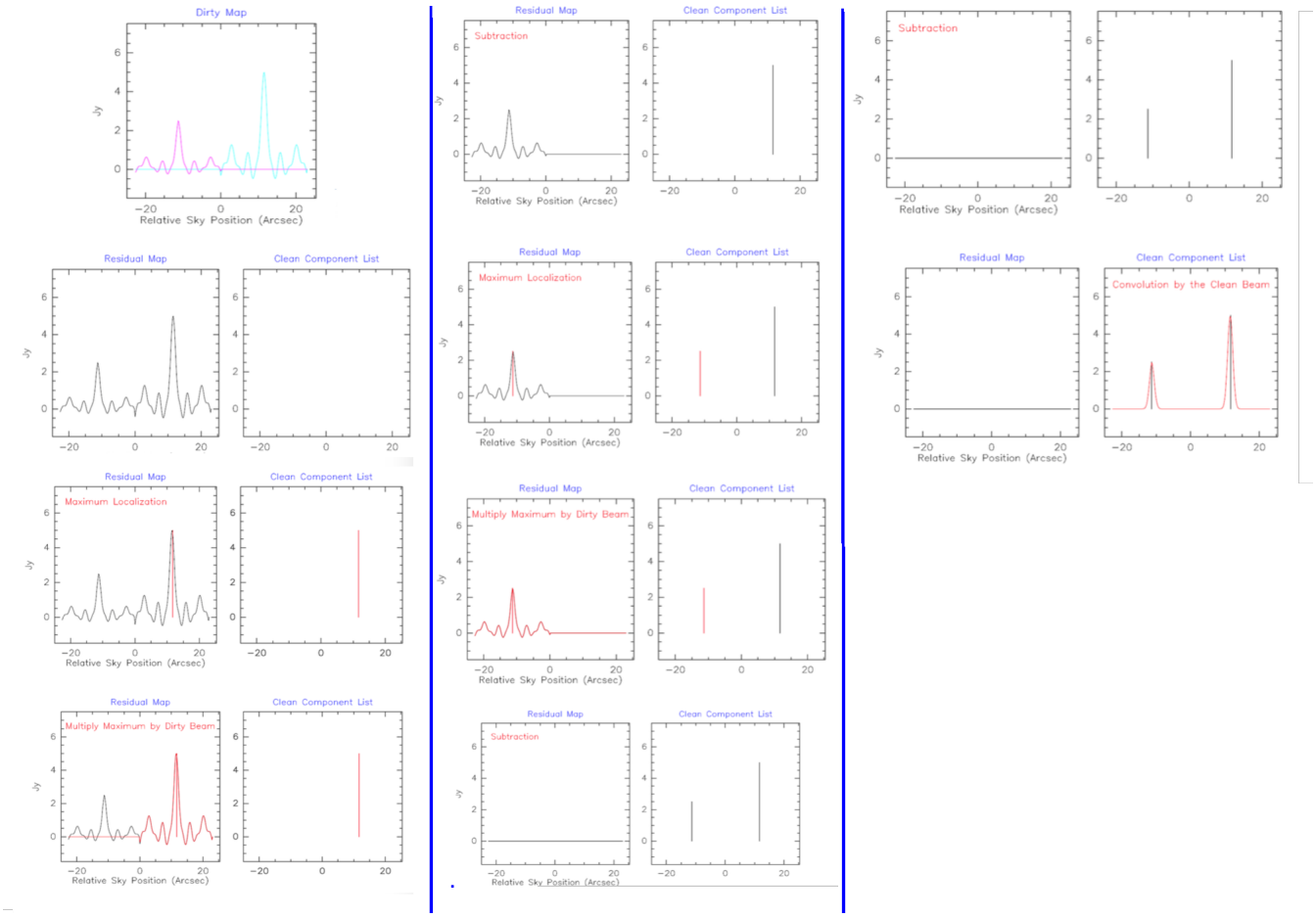

Figure A.5. *Basic CLEAN algorithm. (J. Pety lecture at 8th IRAM Millimeter Interferometry School)*

In conclusion, interferometry samples Fourier components of sky brightness, therefore to make an image it is necessary to Fourier transform the sampled visibilities and then deconvolve to correct for incomplete sampling.
The resulting restored image is an estimate of the true sky brightness I(l,m) and depends on imaging parameters (pixel size, visibility weighting scheme, gridding) and deconvolution (algorithm, iterations, masks, stopping criteria).

A.3.3 Noise

The system temperature T_{sys} is the thermal noise of the data, connected to the emission temperature of the receivers and atmosphere.
What the antenna measures is $T_{sys} = T_A + T_R$ where the receiver temperature T_R is of the order of tens of Kelvin depending on the observed frequency, largely dominating on the antenna temperature T_A.
Therefore, the system temperature represents the average of many measures and determines the noise level of an observation. For a two-element system:

$$\Delta T_{rms} \propto \frac{T_{sys}}{\sqrt{t\Delta\nu}} \qquad k\Delta T_{rms} = \frac{\Delta S A_r}{2} \qquad \longrightarrow \qquad \Delta S = 2k\frac{T_{sys}}{A_r\sqrt{2t\Delta\nu}}$$

where A_r is the receiving area of the antenna, t is the integration time and $\Delta\nu$ is the band width of the channel.

Figure A.6. *Very Large Array with a zoom on an antenna receiver. Here, the VLA presents a low band (dish + dipole) configuration transitioned to wide-bandwidth.*

For an array of N identical telescopes, there are $N(N-1)/2$ simultaneous pair-wise correlations. Then the rms variation in flux density is:

$$\Delta S = 2k\frac{T_{sys}}{A_r\sqrt{2Nt\Delta\nu}}$$

As an example, the performance of the VLA at 1.3 cm is shown: for the twenty-seven 25 m diameter antennas of the VLA, each with $A_r = 300m^2$, after a four hour integration on source with a 100 K system noise and 7.8 kHz frequency resolution, in a 3 arcsec synthesized beam, the flux density rms sensitivity is 3.2 mJy.

A.3.4 VLA

The Karl G. Jansky Very Large Array (VLA) is made by 27 radio antennas located 80 km west of Socorro (New Mexico) on the high Plains of San Augustin at 2124 m above sea level. It is a component of the National Radio Astronomy Observatory (NRAO).
The dishes, each of which has a diameter of 25 m, are placed on rails along three arms in a shape of a large Y. The Y-configuration produces a nearly circular synthesized beam on the sky for a variety of integration times and for most positions on the sky. Also, a Y-configuration is the most efficient arrangement of antennas which need to be connected to a central power and

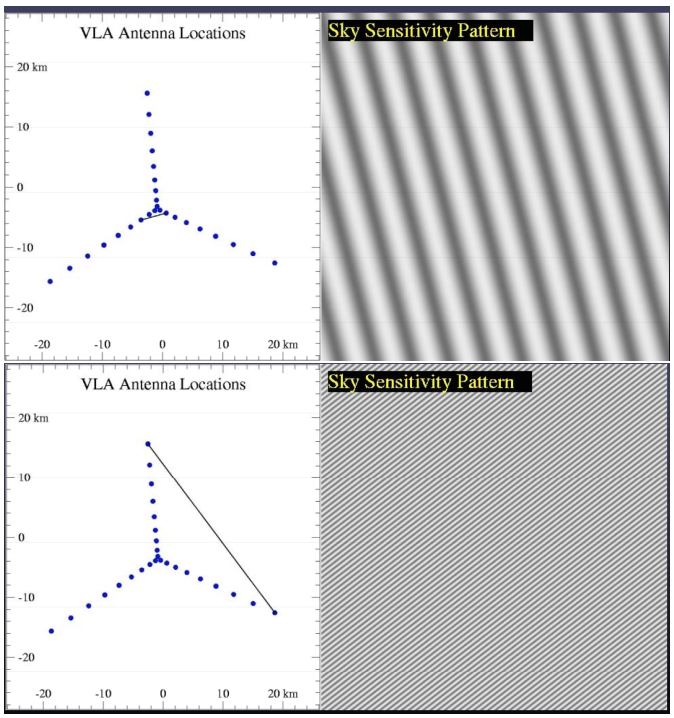

Figure A.7. At the top, a short baseline fringe pattern.
At the bottom, a long baseline fringe pattern.

Configuration	b_{max} (km)	b_{min} (m)
A	36.4	680
B	11.1	240
C	3.4	45
D	1.0	35

Table A.1. VLA configurations and the related maximum and minimum antenna separations.

communication center. Finally, the Y-configuration makes it possible to expand and contract the array to allow for a variety of synthesized beam sizes on the sky.
A four-hour observation then includes baselines at a full range of angles, containing enough information to construct a basic map.
The principal configurations [6] are called A, B, C and D and their maximum and minimum baselines are shown in tab. A.1.
The frequency coverage is wide: from 74 MHz to 50 GHz, or from 4 m to 0.7 cm in wavelengths.

The VLA has undergone an upgrade to become the EVLA starting from 2001, where the E stands for "expanded". New receivers and a far more powerful correlator have been implemented. The continuum sensitivity has improved over the VLA by factors of 5 to 20, to give point-source sensitivity better than 1 μJy between 2 and 40 GHz.

[6] In addition to the principal configurations, there are the hybrid configurations DnC, CnB and BnA, recommended for sources located south of declination -15 degrees or north of declination 75 degrees.

A.3.5 Very Long Baseline Interferometry

As previously seen, for a given wavelength the angular resolution of an interferometer depends only on the baseline, that is limited by the need of phase-stable links such as optical fibers between individual antennas and the correlator sets. Therefore, the baselines can reach a maximum of a few hundred kilometers (MERLIN, UK).
To obtain an excellent resolution, the antennas must be spaced of about thousands of kilometers, therefore the Very Long Baseline Interferometer (VLBI) was born when the development of atomic clocks and extremely phase-stable oscillators led radio astronomers to the idea of independent measurements at every individual antennas of the interferometer.
Today, data can be recorded on storage devices [7] together with precise time marks and correlated later avoiding the transmission of a local oscillator signal.
The antenna outputs contain accurate records of the time variation of the electrical field strength so that the appropriately time-averaged product obtained by multiplying the digitized signal gives the mutual correlation function directly.
Observationally, VLBI can be used to carry out surveys of a large number of sources. Such surveys make use of procedures that are similar to those used in the snapshot observing mode of instruments such as the VLA. Each measurement has a total integration time of up to tens of minutes. For such surveys, the observing runs may extend over few days so that hundreds of sources are measured.
Examples of arrays characterized by baseline of the order of 10^3 km are the Very Long Baseline Array (VLBA) and the European VLBI Network (EVN) [8], which is the most sensitive VLBI array in the world. The combination of EVN and VLBA can be made and is known as Global VLBI.
In the quest for even larger angular resolution, satellites have been placed in Earth orbit to provide extended baselines.

A.3.6 LOFAR

The Low-Frequency Array built by the Netherlands Institute for Radio Astronomy (ASTRON) is known as LOFAR (Van Haarlem et al., 2013).
This interferometric array is characterized by multiple stations combined to create synthesized beams. Thousands omni-directional antennas without moving parts are in at least 48 larger stations, with effective aperture sizes that range from 30 m to 80 m depending on the frequency. The majority of stations is across the Netherlands. Five stations are in Germany, and one each in Great Britain, France and Sweden. Further stations may also be built in other European countries. International stations provide LOFAR with an angular resolution of $\simeq 0.15$ arcsec at 240 MHz and $\simeq 1$ arcsec at 30 MHz.
LOFAR is optimized for the frequency range from 30 to 240 MHz, but also with the ability to observe down to 10 MHz. The telescope receivers are two different kind of dipoles:

- the low-band antennas (LBA), which cover the frequency range 10 - 90 MHz with reso-

[7] Storage devices are hard disks that are shipped to a central correlator location; in the near future these will be sent in real time or near real time over the internet.

[8] whose data are processed at the Joint Institute for VLBI in Europe (JIVE).

Figure A.8. *Low-Frequency Array(Van Haarlem et al., 2013).*
On the left, aerial photograph of the heart of the LOFAR core: a large circular island with six stations. Three additional LOFAR core stations are visible in the upper right and lower left of the image. Each of these includes a field of 96 low-band antennas and two sub-stations of 24 high-band antenna tiles each.
On the right, a single LOFAR LBA dipole including the ground plane.

lution from 40 to 8 arcsec, a field of view from 1089 to 220 arcmin and a sensitivity from 110 to 12 mJy;

- the high-band antennas (HBA), which cover the frequency range 110 - 240 MHz with resolution from 5 to 3 arcsec, a field of view from 272 to 136 arcmin and a sensitivity from 0.41 to 0.46 mJy.

A delay is applied to the relative phases of the signals feeding the dipoles in each station, creating a phased aperture array. This allows to improve the radiation pattern of the array in a target direction and suppress in undesired ones. By applying different delays, LOFAR can therefore point in more than one direction simultaneously and the number of beams is limited only by the bandwidth necessary to transfer the signal to the correlator (De Gasperin et al., 2012).

Appendix B

CASA

CASA (Common Astronomy Software Applications) is a set of C++ application libraries for the data reduction and analysis of radio astronomical data. Its tasks for analysis procedures and tools for data access, display and editing can be run through the IPython interface to Python.
CASA was developed in the 1990s to store both interferometry and single-dish data as the next generation of AIPS. Currently, it is being developed for ALMA and EVLA projects, but it can also be useful for data analysis in the millimeter and sub-millimeter range. Therefore, it can support in principle any setup of radio telescopes.

The data, such as visibilities, images and calibration information, are stored in tables. In particular, the table containing the visibilities is called Measurement Set (extension .ms) as shown in table B.1 (Kemball & Wieringa, 2000). In the main table every row represents a temporal stamp with information about the source and the instrument (antenna configuration, pointing, source fluxes) per spectral window and per baseline. Additional columns can be allocated with the data modified during the calibration or Fourier inversion processes.

The data are processed via the measurement equation (Hamaker, Bregman, Sault, 1996), which connects the observed visibility $\vec{V}_{ij}^{obs}$, decomposed into individual calibration components, to the ideal visibility $\vec{V}_{ij}^{ideal}$:

$$\vec{V}_{ij}^{obs} = G^i \, G^j \, \vec{V}_{ij}^{ideal} \tag{B.1}$$

where i and j indicate the antennas which form the baseline and G^i, G^j are the complex gains. They are defined for each antenna by many components along the signal path :

$$G^i = K^i \, B^i \, J^i \, D^i \, E^i \, P^i \, T^i \, F^i \qquad G^j = K^j \, B^j \, J^j \, D^j \, E^j \, P^j \, T^j \, F^j \tag{B.2}$$

where each term has matrix form:

- K is the geometric compensation;
- B is the bandpass response;
- J is the electronic gain;
- D is the polarization leakage;

Main	original visibility data
Model	Fourier transform of:
	- image made from MS
	- supplied model image
	- calibrator flux density
Corrected	copy of visibilities with calibration tables applied
Flags	classification of visibilities (acceptable or not)

Table B.1. Data in CASA: the Measurement Set in a simple view.

- E is the antenna voltage pattern (primary beam effects);
- P is the parallactic angle (altaz-mounts);
- T are the tropospheric effects;
- F is the ionospheric Faraday rotation.

They are either additive (phases) or multiplicative (amplitudes). In most cases, when performing calibration (information in "calibrator model" step in fig. B.1) we can forget the origin of the contribution to be removed. Some of them are specific to each type of observation (VLBI, spectral line analysis, wide field) and of the observing frequency.

Two quantities that must be calibrated for continuum measurements are amplitude and phase. In addition, for spectral line measurements the instrument passband must also be calibrated. Note that the amplitude, phase and passband calibrations are carried out before the source measurements.
The amplitude scale is calibrated using methods that are similar to those used for single dish measurements. This consists of using the response of each antenna to determine the system noise of the receiver. In the centimeter range, the atmosphere plays a small role while in the millimeter and sub-millimeter wavelength ranges, the atmospheric effects must be accounted for.
For phase measurements, a suitable point-like source with an accurately known position is required to determine the instrumental phase. For interferometers, the calibration sources are usually unresolved or point-like sources, often extragalactic sources.
The passband calibration is carried out by an integration of an intense source to determine the channel-to-channel gains and offsets. This latter calibration is usually made once per observing session, whereas the amplitude and phase calibrations are made more often, depending on the stability of the electronics and weather.

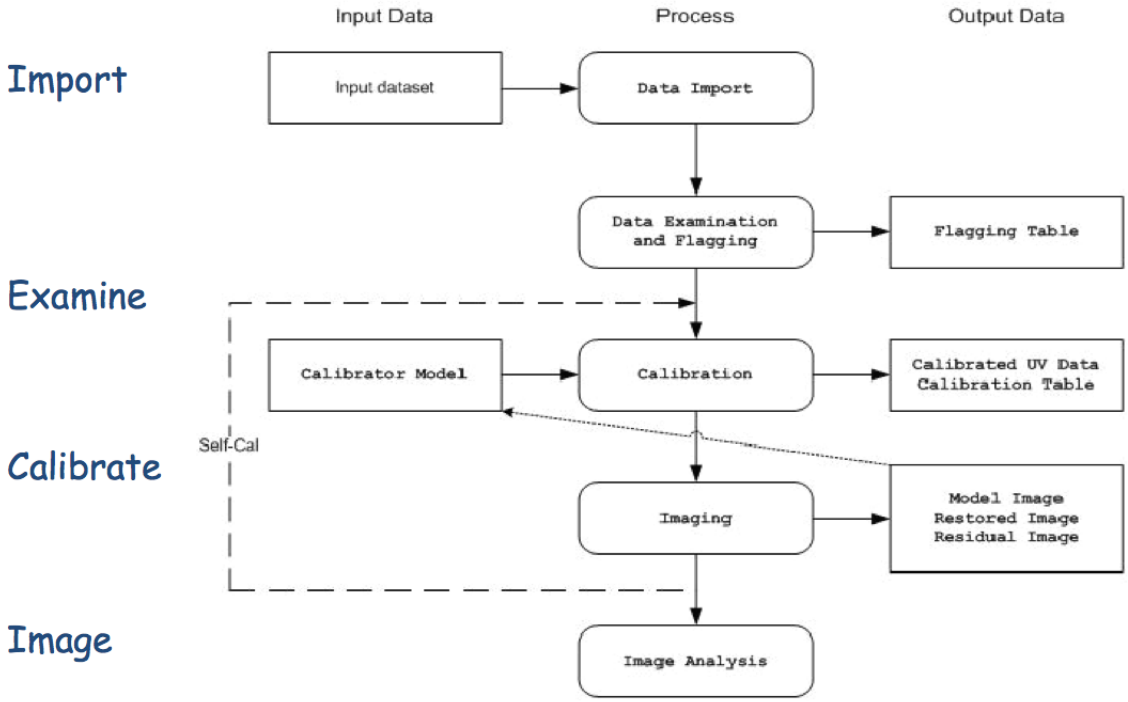

Figure B.1. *Processing philosophy.*

Bibliography

A. A. et al. Abdo. Fermi Large Area Telescope Gamma-Ray Detection of the Radio Galaxy M87. *Astrophys. J.*, 707:55–60, December 2009.

A. Abramowski, F. Acero, F. Aharonian, A. G. Akhperjanian, G. Anton, A. Balzer, A. Barnacka, U. Barres de Almeida, Y. Becherini, J. Becker, and et al. The 2010 Very High Energy γ-Ray Flare and 10 Years of Multi-wavelength Observations of M 87. *Astrophys. J.*, 746:151, February 2012.

V. A. et al. Acciari. Veritas 2008-2009 Monitoring of the Variable Gamma-ray Source M 87. *Astrophys. J.*, 716:819–824, June 2010.

F. A. Aharonian. *Very high energy cosmic gamma radiation : a crucial window on the extreme Universe, River Edge, NJ: World Scientific Publishing*. 2004.

F. et al. Aharonian. Is the giant radio galaxy M 87 a TeV gamma-ray emitter? *Astron. Astrophys.*, 403:L1–L5, May 2003.

F. et al. Aharonian. Discovery of Very High Energy γ-Ray Emission from Centaurus a with H.E.S.S. *Astrophys. J. Lett.*, 695:L40–L44, April 2009.

J. et al. Aleksić. MAGIC observations of the giant radio galaxy M 87 in a low-emission state between 2005 and 2007. *Astron. Astrophys.*, 544:A96, August 2012.

H. Alfvén and N. Herlofson. Cosmic Radiation and Radio Stars. *Physical Review*, 78:616–616, June 1950.

R. Antonucci. Unified models for active galactic nuclei and quasars. *Ann. Rev. Astron. Astroph.*, 31:473–521, 1993.

R. Beck and M. Krause. Revised equipartition and minimum energy formula for magnetic field strength estimates from radio synchrotron observations. *Astronomische Nachrichten*, 326:414–427, July 2005.

V. Beckmann and C. R. Shrader. *Active Galactic Nuclei, Wiley-VCH Verlag GmbH*. August 2012.

A. R. Bell. The acceleration of cosmic rays in shock fronts. II. *Mon. Not. Roy. Astron. Soc.*, 182: 443–455, February 1978.

M. C. Bentz, K. D. Denney, E. M. Cackett, M. Dietrich, J. K. J. Fogel, H. Ghosh, K. Horne, C. Kuehn, T. Minezaki, C. A. Onken, B. M. Peterson, R. W. Pogge, V. I. Pronik, D. O. Richstone, S. G. Sergeev, M. Vestergaard, M. G. Walker, and Y. Yoshii. A Reverberation-based Mass for the Central Black Hole in NGC 4151. *Astrophys. J.*, 651:775–781, November 2006.

B. Binggeli, C. C. Popescu, and G. A. Tammann. The kinematics of the Virgo cluster revisited. *Astron. Astrophys.*, 98:275–296, April 1993.

J. A. Biretta and W. Junor. Results of lambda18 cm vlbi monitoring of the radio jet of virgo a, american astronomical society meeting abstracts. volume 26 of *Bulletin of the American Astronomical Society*, page 109.12, December 1994.

J. A. Biretta, F. N. Owen, and T. J. Cornwell. A search for motion and flux variations in the M87 jet. *Astrophys. J.*, 342:128–134, July 1989.

J. A. Biretta, C. P. Stern, and D. E. Harris. The radio to X-ray spectrum of the M87 jet and nucleus. *Astron. J.*, 101:1632–1646, May 1991.

J. A. Biretta, F. Zhou, and F. N. Owen. Detection of Proper Motions in the M87 Jet. *Astrophys. J.*, 447:582, July 1995.

J. A. Biretta, E. Perlman, W. B. Sparks, and F. Macchetto. Hst observations of the m 87 jet, the radio galaxy messier 87. volume 530 of *Lecture Notes in Physics, Berlin Springer Verlag*, page 210, 1999a.

J. A. Biretta, W. B. Sparks, and F. Macchetto. Hubble Space Telescope Observations of Superluminal Motion in the M87 Jet. *Astrophys. J.*, 520:621–626, August 1999b.

R. D. Blandford. Physical processes in active galactic nuclei. pages 161–275, 1990.

R. D. Blandford and C. F. McKee. Reverberation mapping of the emission line regions of Seyfert galaxies and quasars. *Astrophys. J.*, 255:419–439, April 1982.

R. D. Blandford and D. G. Payne. Hydromagnetic flows from accretion discs and the production of radio jets. *Mon. Not. Roy. Astron. Soc.*, 199:883–903, June 1982.

R. D. Blandford and R. L. Znajek. Electromagnetic extraction of energy from Kerr black holes. *Mon. Not. Roy. Astron. Soc.*, 179:433–456, May 1977.

H. Bohringer, P. E. J. Nulsen, R. Braun, and A. C. Fabian. The interaction of the radio halo of M87 with the cooling intracluster medium of the Virgo cluster. *Mon. Not. Roy. Astron. Soc.*, 274:L67–L71, June 1995.

H. et al. Böhringer. The structure of the Virgo cluster of galaxies from Rosat X-ray images. *Nature*, 368:828–831, April 1994.

A. Boksenberg, F. Macchetto, R. Albrecht, C. Barbieri, J. C. Blades, P. Crane, J. M. Deharveng, M. J. Disney, P. Jakobsen, T. M. Kamperman, I. R. King, C. D. Mackay, F. Paresce, G. Weigelt, D. Baxter, P. Greenfield, R. Jedrzjewski, A. Nota, and W. B. Sparks. Faint Object Camera observations of M87 - The jet and nucleus. *Astron. Astrophys.*, 261:393–404, August 1992.

A. H. Bridle and R. A. Perley. Extragalactic Radio Jets. *Ann. Rev. Astron. Astroph.*, 22:319–358, 1984.

G. R. Burbidge. On Synchrotron Radiation from Messier 87. *Astrophys. J.*, 124:416, September 1956.

V. Cayatte, J. H. van Gorkom, C. Balkowski, and C. Kotanyi. VLA observations of neutral hydrogen in Virgo Cluster galaxies. I - The Atlas. *Astron. J.*, 100:604–634, September 1990.

M. Chiaberge, A. Celotti, A. Capetti, and G. Ghisellini. Does the unification of BL Lac and FR I radio galaxies require jet velocity structures? *Astron. Astrophys.*, 358:104–112, June 2000.

A. et al. Chung. Vla imaging of virgo spirals in atomic gas (viva). i. the atlas and the h i properties. *The Astronomical Journal*, 138(6):1741, 2009. URL `http://stacks.iop.org/1538-3881/138/i=6/a=1741`.

E. Churazov, M. Brüggen, C. R. Kaiser, H. Böhringer, and W. Forman. Evolution of Buoyant Bubbles in M87. *Astrophys. J.*, 554:261–273, June 2001.

B. G. Clark. An efficient implementation of the algorithm 'CLEAN'. *Astron. Astrophys.*, 89:377, September 1980.

R. Dodson, P. G. Edwards, and H. Hirabayashi. Milliarcsecond-Scale Spectral Properties and Jet Motions in M 87. , 58:243–251, April 2006.

A. Dressler. Galaxy morphology in rich clusters - Implications for the formation and evolution of galaxies. *Astrophys. J.*, 236:351–365, March 1980.

R. J. H. Dunn, A. C. Fabian, and G. B. Taylor. Radio bubbles in clusters of galaxies. 364(4): 1343–1353, 2005.

J. Eilek, P. Hardee, T. Markovic, M. Ledlow, and F. Owen. On dynamical models for radio galaxies. *New Astron. Rev.*, 46:327–334, May 2002.

J. A. Eilek and S. N. Shore. The energetics and evolution of jet-fed radio sources. *Astrophys. J.*, 342:187–207, July 1989.

J. A. Eilek, D. B. Melrose, and M. A. Walker. Synchrotron Aging in Filamented Magnetic Fields. *Astrophys. J.*, 483:282–295, July 1997.

M. Elvis, B. J. Wilkes, J. C. McDowell, R. F. Green, J. Bechtold, S. P. Willner, M. S. Oey, E. Polomski, and R. Cutri. Atlas of quasar energy distributions. *Astrophys. J. Supp. Ser.*, 95: 1–68, November 1994.

de Gasperin F. et al. M 87 at metre wavelengths: the LOFAR picture. *Astron. Astrophys.*, 547: A56, November 2012.

van Haarlem et al. LOFAR: The LOw-Frequency ARray. *Astron. Astrophys.*, 556:A2, August 2013.

A. C. Fabian and G. Miniutti. The X-ray spectra of accreting Kerr black holes. *ArXiv Astrophysics e-prints*, July 2005.

A. C. Fabian, E. M. Hu, L. L. Cowie, and J. Grindlay. The distribution and morphology of X-ray-emitting gas in the core of the Perseus cluster. *Astrophys. J.*, 248:47–54, August 1981.

D. Fabricant, M. Lecar, and P. Gorenstein. X-ray measurements of the mass of M87. *Astrophys. J.*, 241:552–560, October 1980.

R. Falomo, E. Pian, and A. Treves. An optical view of BL Lacertae objects. , 22:73, September 2014.

B. L. Fanaroff and J. M. Riley. The morphology of extragalactic radio sources of high and low luminosity. *Mon. Not. Roy. Astron. Soc.*, 167:31P–36P, May 1974.

E. D. Feigelson, J. M. Jackson, R. D. Mathieu, P. C. Myers, and F. M. Walter. An X-ray survey for pre-main-sequence stars in the Taurus-Auriga and Perseus molecular cloud complexes. *Astron. J.*, 94:1251–1259, November 1987.

L. Ferrarese and H. Ford. Supermassive Black Holes in Galactic Nuclei: Past, Present and Future Research. , 116:523, February 2005.

W. Forman, E. Kellogg, H. Gursky, H. Tananbaum, and R. Giacconi. Observations of the Extended X-Ray Sources in the Perseus and Coma Clusters from UHURU. *Astrophys. J.*, 178:309–316, December 1972.

W. Forman, P. Nulsen, S. Heinz, F. Owen, J. Eilek, A. Vikhlinin, M. Markevitch, R. Kraft, E. Churazov, and C. Jones. Reflections of Active Galactic Nucleus Outbursts in the Gaseous Atmosphere of M87. *Astrophys. J.*, 635:894–906, December 2005.

W. Forman, C. Jones, E. Churazov, M. Markevitch, P. Nulsen, A. Vikhlinin, M. Begelman, H. Böhringer, J. Eilek, S. Heinz, R. Kraft, F. Owen, and M. Pahre. Filaments, Bubbles, and Weak Shocks in the Gaseous Atmosphere of M87. *Astrophys. J.*, 665:1057–1066, August 2007.

C. F. Gammie, S. L. Shapiro, and J. C. McKinney. Black Hole Spin Evolution. *Astrophys. J.*, 602: 312–319, February 2004.

D. Garofalo. The Spin Dependence of the Blandford-Znajek Effect. *Astrophys. J.*, 699:400–408, July 2009.

S. T. Garrington, J. P. Leahy, R. G. Conway, and R. A. Laing. A systematic asymmetry in the polarization properties of double radio sources with one jet. *Nature*, 331:147–149, January 1988.

G. Giovannini, C. Casadio, M. Giroletti, M. Beilicke, A. Cesarini, and H. Krawczynski. The jet in M87 from e-EVN observations. volume 275 of *IAU Symposium*, pages 150–154, February 2011.

F. Govoni and L. Feretti. Magnetic Fields in Clusters of Galaxies. *International Journal of Modern Physics D*, 13:1549–1594, 2004.

M. R. Greason, R. W. O'Connell, S. G. Neff, E. P. Smith, P. M. N. Hintzen, A. M. Smith, T. P. Stecher, M. S. Roberts, R. H. Cornett, J. K. Hill, and W. B. Landsman. Ultraviolet imaging telescope observations of m87, bulletin of the american astronomical society. volume 23, page 922, March 1991.

M. Haas, S. A. H. Müller, F. Bertoldi, R. Chini, S. Egner, W. Freudling, U. Klaas, O. Krause, D. Lemke, K. Meisenheimer, R. Siebenmorgen, and I. van Bemmel. The ISOPHOT - MAMBO survey of 3CR radio sources: Further evidence for the unified schemes. *Astron. Astrophys.*, 424:531–543, September 2004.

R. J. Harms, H. C. Ford, Z. I. Tsvetanov, G. F. Hartig, L. L. Dressel, G. A. Kriss, R. Bohlin, A. F. Davidsen, B. Margon, and A. K. Kochhar. HST FOS spectroscopy of M87: Evidence for a disk of ionized gas around a massive black hole. *Astrophys. J. Lett.*, 435:L35–L38, November 1994.

T. Herbig and A. C. S. Readhead. A compendium of radio spectra and luminosities for three complete samples of radio sources. *Astrophys. J. Supp. Ser.*, 81:83–124, July 1992.

A. M. Hillas. The Origin of Ultra-High-Energy Cosmic Rays. *Ann. Rev. Astron. Astroph.*, 22: 425–444, 1984.

J. A. Högbom. Aperture Synthesis with a Non-Regular Distribution of Interferometer Baselines. *Astron. Astrophys.*, 15:417, June 1974.

C. A. Jackson and J. V. Wall. Radio galaxy spectra, particles and fields in radio galaxies conference. volume 250 of *Astronomical Society of the Pacific Conference Series*, page 400, 2001.

W. J. Jaffe and G. C. Perola. Dynamical Models of Tailed Radio Sources in Clusters of Galaxies. *Astron. Astrophys.*, 26:423, August 1973.

A. Jordán, P. Côté, J. P. Blakeslee, L. Ferrarese, D. E. McLaughlin, S. Mei, E. W. Peng, J. L. Tonry, D. Merritt, M. Milosavljević, C. L. Sarazin, G. R. Sivakoff, and M. J. West. The ACS Virgo Cluster Survey. X. Half-Light Radii of Globular Clusters in Early-Type Galaxies: Environmental Dependencies and a Standard Ruler for Distance Estimation. *Astrophys. J.*, 634:1002–1019, December 2005.

W. Junor, J. A. Biretta, and M. Livio. Formation of the radio jet in M87 at 100 Schwarzschild radii from the central black hole. *Nature*, 401:891–892, October 1999.

N. E. Kassim, R. A. Perley, W. C. Erickson, and K. S. Dwarakanath. Subarcminute resolution imaging of radio sources at 74 MHz with the Very Large Array. *Astron. J.*, 106:2218–2228, December 1993.

Y. Kato, S. Mineshige, and K. Shibata. Magnetohydrodynamic Accretion Flows: Formation of Magnetic Tower Jet and Subsequent Quasi-Steady State. *Astrophys. J.*, 605:307–320, April 2004.

P. Kharb. *A Pc-scale study of radio-loud AGN: The Fanaroff-Riley Divide and Unification*. PhD thesis, Indian Institute of Astrophysics, 2004.

P. Kharb, C. P. O'Dea, S. A. Baum, R. A. Daly, M. P. Mory, M. Donahue, and E. J. Guerra. A Study of 13 Powerful Classical Double Radio Galaxies. *Astrophys. J. Supp. Ser.*, 174:74–110, January 2008.

R. A. Koopmann and J. D. P. Kenney. Massive Star Formation Rates and Radial Distributions from Hα Imaging of 84 Virgo Cluster and Isolated Spiral Galaxies. *Astrophys. J.*, 613:851–865, October 2004.

J. Kormendy and L. C. Ho. Coevolution (Or Not) of Supermassive Black Holes and Host Galaxies: Supplemental Material. *Ann. Rev. Astron. Astroph.*, August 2013.

K. Kotera and A. V. Olinto. The Astrophysics of Ultrahigh-Energy Cosmic Rays. *Ann. Rev. Astron. Astroph.*, 49:119–153, September 2011.

T. P. Krichbaum, D. A. Graham, M. Bremer, W. Alef, A. Witzel, J. A. Zensus, and A. Eckart. Sub-Milliarcsecond Imaging of Sgr A* and M 87. *Journal of Physics Conference Series*, 54: 328–334, December 2006.

J. H. Krolik. *Active galactic nuclei : from the central black hole to the galactic environment, Princeton University Press*. 1999.

R. A. Laing. The sidedness of jets and depolarization in powerful extragalactic radio sources. *Nature*, 331:149–151, January 1988.

C. Leipski, R. Antonucci, P. Ogle, and D. Whysong. The Spitzer View of FR I Radio Galaxies: On the Origin of the Nuclear Mid-Infrared Continuum. *Astrophys. J.*, 701:891–914, August 2009.

E. J. Lindfors, M. Türler, E. Valtaoja, H. Aller, M. Aller, D. Mazin, C. M. Raiteri, J. A. Stevens, M. Tornikoski, G. Tosti, and M. Villata. Synchrotron flaring in the jet of 3C 279. *Astron. Astrophys.*, 456:895–903, September 2006.

C. Ly, R. C. Walker, and J. M. Wrobel. An Attempt to Probe the Radio Jet Collimation Regions in NGC 4278, NGC 4374 (M84), and NGC 6166. *Astron. J.*, 127:119–124, January 2004.

C. Ly, R. C. Walker, and W. Junor. High-Frequency VLBI Imaging of the Jet Base of M87. *Astrophys. J.*, 660:200–205, May 2007.

D. Lynden-Bell. Galactic Nuclei as Collapsed Old Quasars. *Nature*, 223:690–694, August 1969.

F. Macchetto, A. Marconi, D. J. Axon, A. Capetti, W. Sparks, and P. Crane. The Supermassive Black Hole of M87 and the Kinematics of Its Associated Gaseous Disk. *Astrophys. J.*, 489: 579–600, November 1997.

E. Maoz. Dynamical Constraints on Alternatives to Supermassive Black Holes in Galactic Nuclei. *Astrophys. J. Lett.*, 494:L181–L184, February 1998.

M. Mariotti. MAGIC observes increased VHE gamma ray flux from M87. *The Astronomer's Telegram*, 2431:1, February 2010.

H. L. Marshall, B. P. Miller, D. S. Davis, E. S. Perlman, M. Wise, C. R. Canizares, and D. E. Harris. A High-Resolution X-Ray Image of the Jet in M87. *Astrophys. J.*, 564:683–687, January 2002.

J. C. McKinney. General relativistic magnetohydrodynamic simulations of the jet formation and large-scale propagation from black hole accretion systems. *Mon. Not. Roy. Astron. Soc.*, 368:1561–1582, June 2006.

S. Mei, J. P. Blakeslee, P. Côté, J. L. Tonry, M. J. West, L. Ferrarese, A. Jordán, E. W. Peng, A. Anthony, and D. Merritt. The ACS Virgo Cluster Survey. XIII. SBF Distance Catalog and the Three-dimensional Structure of the Virgo Cluster. *Astrophys. J.*, 655:144–162, January 2007.

E. T. Meyer, W. B. Sparks, J. A. Biretta, J. Anderson, S. T. Sohn, R. P. van der Marel, C. Norman, and M. Nakamura. Optical Proper Motion Measurements of the M87 Jet: New Results from the Hubble Space Telescope. *Astrophys. J. Lett.*, 774:L21, September 2013.

M. Miyoshi, J. Moran, J. Herrnstein, L. Greenhill, N. Nakai, P. Diamond, and M. Inoue. Evidence for a black hole from high rotation velocities in a sub-parsec region of NGC4258. *Nature*, 373:127–129, January 1995.

M. Murgia, C. Fanti, R. Fanti, L. Gregorini, U. Klein, K.-H. Mack, and M. Vigotti. Synchrotron spectra and ages of compact steep spectrum radio sources. *Astron. Astrophys.*, 345:769–777, May 1999.

F. Owen and J. Biretta. Vla 7mm images of the m 87 jet, the radio galaxy messier 87. volume 530 of *Lecture Notes in Physics, Berlin Springer Verlag*, page 186, 1999.

F. N. Owen and R. A. Laing. CCD surface photometry of radio galaxies. I - FR class I and II sources. *Mon. Not. Roy. Astron. Soc.*, 238:357–378, May 1989.

F. N. Owen and M. J. Ledlow. The FRI/II Break and the Bivariate Luminosity Function in Abell Clusters of Galaxies. volume 54 of *Astronomical Society of the Pacific Conference Series*, page 319, 1994.

F. N. Owen, J. A. Eilek, and W. C. Keel. Detection of large Faraday rotation in the inner 2 kiloparsecs of M87. *Astrophys. J.*, 362:449–454, October 1990.

F. N. Owen, J. A. Eilek, and N. E. Kassim. M87 at 90 Centimeters: A Different Picture. *Astrophys. J.*, 543:611–619, November 2000.

A. G. Pacholczyk. *Radio astrophysics. Nonthermal processes in galactic and extragalactic sources, Series of Books in Astronomy and Astrophysics, San Francisco: Freeman, 1970*. 1970.

E. S. Perlman, J. A. Biretta, W. B. Sparks, F. D. Macchetto, and J. P. Leahy. The Optical-Near-Infrared Spectrum of the M87 Jet fromHubble Space Telescope Observations. *Astrophys. J.*, 551:206–222, April 2001.

J. Pinkney, J. O. Burns, M. J. Ledlow, P. L. Gómez, and J. M. Hill. Substructure in Clusters Containing Wide-Angle-Tailed Radio Galaxies. I. New Redshifts. *Astron. J.*, 120:2269–2277, November 2000.

R. M. Prestage and J. A. Peacock. The cluster environments of powerful radio galaxies. *Mon. Not. Roy. Astron. Soc.*, 230:131–160, January 1988.

M. J. Rees. Black Hole Models for Active Galactic Nuclei. *Ann. Rev. Astron. Astroph.*, 22: 471–506, 1984.

M. J. Reid, J. A. Biretta, W. Junor, T. W. B. Muxlow, and R. E. Spencer. Subluminal motion and limb brightening in the nuclear jet of M87. *Astrophys. J.*, 336:112–120, January 1989.

C. S. Reynolds, A. C. Fabian, A. Celotti, and M. J. Rees. The matter content of the jet in M87: evidence for an electron-positron jet. *Mon. Not. Roy. Astron. Soc.*, 283:873–880, December 1996.

H. Rottmann, K.-H. Mack, U. Klein, and R. Wielebinski. The radio lobes of Virgo A at 2.8cm wavelength. *Astron. Astrophys.*, 309:L19–L22, May 1996.

G. B. Rybicki and A. P. Lightman. *Radiative processes in astrophysics, New York, Wiley-Interscience, 1979. 393 p.* 1979.

M. Ryle and A. Hewish. The synthesis of large radio telescopes. *Mon. Not. Roy. Astron. Soc.*, 120:220, 1960.

N. I. Shakura and R. A. Sunyaev. Black holes in binary systems. Observational appearance. *Astron. Astrophys.*, 24:337–355, 1973.

O. B. Slee, A. L. Roy, M. Murgia, H. Andernach, and M. Ehle. Four Extreme Relic Radio Sources in Clusters of Galaxies. *Astron. J.*, 122:1172–1193, September 2001.

V. Smolčić, G. Zamorani, E. Schinnerer, S. Bardelli, M. Bondi, L. Bîrzan, C. L. Carilli, P. Ciliegi, M. Elvis, C. D. Impey, A. M. Koekemoer, A. Merloni, T. Paglione, M. Salvato, M. Scodeggio, N. Scoville, and J. R. Trump. Cosmic Evolution of Radio Selected Active Galactic Nuclei in the Cosmos Field. *Astrophys. J.*, 696:24–39, May 2009.

L. S. Sparke and J. S. Gallagher, III. *Galaxies in the Universe: an introduction*.

D. Spergel. The new standard cosmology, american physical society.

R. Subrahmanyan, R. W. Hunstead, N. L. J. Cox, and V. McIntyre. SGRS J0515-8100: A Fat-Double Giant Radio Galaxy. *Astrophys. J.*, 636:172–180, January 2006.

G. B. Taylor, C. L. Carilli, and R. A. Perley, editors. *Synthesis Imaging in Radio Astronomy II*, volume 180 of *Astronomical Society of the Pacific Conference Series*, 1999.

A. R. Thompson, J. M. Moran, and G. W. Swenson, Jr. *"Interferometry and synthesis in radio astronomy by A. Richard Thompson, James M. Moran, and George W. Swenson, Jr. 2nd ed. New York : Wiley, c2001.xxiii, 692 p. : ill. ; 25 cm. "A Wiley-Interscience publication." Includes bibliographical references and indexes. ISBN : 0471254924"*. 2001.

C. M. Urry and P. Padovani. Unified Schemes for Radio-Loud Active Galactic Nuclei. , 107: 803, September 1995.

R. V. Urvashi. *Parameterized deconvolution for wide-band radio synthesis imaging*. PhD thesis, Socorro, May 2010.

V. Vacca. *Intracluster magnetic fields*. PhD thesis, Universitgli Studi di Cagliari, March 2012.

G. L. Verschuur and K. I. Kellermann. *Galactic and extra-galactic radio astronomy, Berlin: Springer, 1988, 2nd ed., edited by Verschuur, Gerrit L.; Kellermann, Kenneth I.* 1988.

M. Volonteri. The formation and evolution of massive black holes. 337(6094):544–547, 2012.

J. L. Walsh, A. J. Barth, L. C. Ho, and M. Sarzi. The M87 Black Hole Mass from Gas-dynamical Models of Space Telescope Imaging Spectrograph Observations. *Astrophys. J.*, 770:86, June 2013.

C.-C. Wang and H.-Y. Zhou. Determination of the intrinsic velocity field in the M87 jet. *Mon. Not. Roy. Astron. Soc.*, 395:301–310, May 2009.

C. Z. Waters and S. E. Zepf. Ultraviolet Hubble Space Telescope Observations of the Jet in M87. *Astrophys. J.*, 624:656–660, May 2005.

J. Wilms, C. S. Reynolds, M. C. Begelman, J. Reeves, S. Molendi, R. Staubert, and E. Kendziorra. XMM-EPIC observation of MCG-6-30-15: direct evidence for the extraction of energy from a spinning black hole? *Mon. Not. Roy. Astron. Soc.*, 328:L27–L31, December 2001.

T. L. Wilson, K. Rohlfs, and S. Hüttemeister. *Tools of Radio Astronomy, by Thomas L. Wilson; Kristen Rohlfs and Susanne Hüttemeister. ISBN 978-3-540-85121-9. Published by Springer-Verlag, Berlin, Germany, 2009.* Springer-Verlag, 2009.

F. Zwicky. On the Masses of Nebulae and of Clusters of Nebulae. *Astrophys. J.*, 86:217, October 1937.

Acknowledgements

I am grateful to Dr. Namir Kassim and Dr. Tracy Clarke for getting this work started and to Dr. Paladino and Dr. Mignano for teaching me the way home (CASA).

I am very grateful to Francesco De Gasperin, who I think is the most cited in this thesis. He has been patiently answering to my n mail, with n very large.

I am very very grateful to Steve, but wait, one of the first thing he taught me is that when you say something important or emotional you should use your mother tongue. Unfortunately, my mother tongue is the same that he uses to talk about politics or bullshits in general. Anyway, time to switch:

Ringrazio sentitamente Steve che mi ha insegnato come fare scienza e come costruire un rapporto da pari a pari tra studente e relatore, credo che in pochi possano dire di aver mangiato un kebab guardando una puntata di Game of thrones a fianco del proprio relatore. Grazie anche per avermi incluso nel giro del giovedí sera da Gianni, i cui panini hanno temprato il mio stomaco!

Ringrazio il prof. Dario Grasso e la prof. Elena Pian che si sono sempre interessati a me e agli sviluppi della tesi.

Ringrazio Alessandro che ha contribuito sostanzialmente a questo lavoro e alla mia stabilitá emotiva nello studio 60. Nonostante il suo primo pensiero sia stato "questa é una cagacazzi", ha saputo apprezzarmi ed essermi amico e collega fidato. Grazie per Got e Twd accompagnati da una sana insalatina o un paninazzo della carta gialla, per gli amari al Sud e per le serate e weekend INFN, per lo meno in buona compagnia.

Ringrazio Ilaria che é stata una fantastica compagna di laboratorio, per tutti i nostri pranzi e perchè se hai voglia di fare due chiacchiere lei c'é sempre.

Ringrazio la Bea e la Fra che pensano che io sia un suuuuper brain nonostante le mie innumerevoli idee di merda, i miei conflitti interiori, interinali ed intestinali. Senza di voi sarei persa.
Fra, grazie perchè da sole potremmo reggere una compagnia telefonica, mi hai chiamato o cercato ogni giorno da quando ci conosciamo. Non so cosa ci siamo dette in tutte quelle telefonate ma abbiamo sicuramente avuto conversazioni brillanti. So che pensi che io sia una delle persone piú intelligenti che tu conosca, ma visto che io lo penso di te forse sei tu la piú

intelligente, scacco matto doc!
Grazie Bea perchè sei la mia certezza e perchè in quella compagnia telefonica tu saresti quella che risolve le grane burocratiche. Grazie per esserti preoccupata per me ogni giorno e per avermi dato consigli saggi che purtroppo non sempre ho seguito.

Ringrazio il Clarino megamind, che é la mia roccia. Non ho mai conosciuto nessuno di tanto forte, soprattutto in un minuscolo spazio vitale come quello di un piccolo canarino.

Ringrazio la Anna che é stata compagna di scuola, di pallavolo e di viaggi per una vita.
(Non ho voglia di capire come mettere apostrofi in latex di merda quindi metto articoli completi davanti a nomi come Anna, perchè in Romagna é obbligatorio.)

Ringrazio la Ale Nanus, la Chicca e la Cate per la splendida amicizia di sempre.

Ringrazio la Betta che é come una sorella.

Ringrazio Renzo e Lorica, perchè sono la loro chicca e per quel poco di romagnolo che so. Oi ció un spo miga savé gnaquel.

Ringrazio Ornella, perchè é stata la migliore insegnante che io abbia avuto.

Ringrazio Anto e Diego, due amici fondamentali e parcheggiatori fidati, compagni di infiniti pomeriggi di studio e di serate alternative a Bologna.
Anto anche se ho rischiato di ucciderti con una banana in laboratorio, non potrei vivere senza un amico con cui blaterare come te!

Ringrazio Arianna, una delle poche persone ad aver letto questa tesi e ad averla trovata pure interessante. Grazie per le ottime torte del lunedí sera e per avermi sopportato al laboratorio di elettronica.

Ringrazio Alessio perchè mi ha dato asilo quando piú ne avevo bisogno, cucinando e risolvendo pazientemente problemi ai miei computer.

Ringrazio Marghe perchè come si fa a non affezionarsi a chi conosce il monotremo.

Ringrazio Vezio, che dopo tutti questi anni continua a chiamarmi Federica.

Ringrazio Marco C. per le nostre praxi vacanze a tratti disgusting e Marco T. per i preziosi consigli e il tempo trascorso in the fucking middle of nowhere.

Ringrazio Robi, perchè anche se insieme a beach siamo scandalose, sei la miglior compagna che si possa avere. Grazie per avermi accolto come extra coinquilina per molto tempo, anche in momenti difficili, come Fede puó testimoniare.

Ringrazio tutti i miei compagni di pallavolo di questi anni di universitá, dai Tarallucci&vino

tra cui ricordo con affetto Andrea, Bob e Luca, alle Palle sgonfie, alle Mine vaganti, ai Gatti fradici e di beach per il Beach volley con Amore, la coppia Mimí e Cocó e per i Puffe e terroncini.

Ringrazio i miei compagni della British per interessanti lezioni e post lezioni.

Ringrazio la Fra coinquilina di sempre, che mi ha visto in ogni condizione esistenziale e fisica. Con te tutto é iniziato e finirá. So che mi hai voluto bene da sempre, forse esattamente da quando mi hai trovato in cucina nuda a bere limmi davanti al frigorifero.

Ringrazio Elena che mi capisce.

Ringrazio gli abitanti di casa Animali, dove sono stata accolta quando avevo bisogno di un posto tranquillo dove non mancassero compagnia, cibo e fantastiche centrifughe.

Ringrazio la Tizzi, con me da una vita, da quando colorava i miei disegni sotto attenta supervisione.

Ringrazio Bruto, Carlotta e Pandora per avermi insegnato piaceri e doveri del prendersi cura di un altro essere.

Ringrazio A. Baricco e J.K. Rowling per avermi regalato letture coinvolgenti anche quando i miei occhi erano stanchi e pieni di parole.

Ringrazio Pepi, perchè ci adoriamo. Sei la mia marmotta super brain che ha pure allineato ció che era inallineabile in questa tesi. Grazie a te che mi porti il sogno, il caffa poesia. Vorrei poter dire che questa ultima frase sia mia, ma devo invece ringraziare Frida Kahlo che ha espresso bene quello che penso del tema amore (pur non conoscendo la ceretta, ci sapeva fare con le parole e il pennello).

Infine, ringrazio Aida e Beppe che desideravano una figlia curiosetta. Questa tesi é dedicata a voi che siete per me un modello e mi avete insegnato ad essere uno spirito libero.

e se ho dimenticato qualcuno #fregacazzi, vi ho sicuramente pensato!